Modelling rainfall erosivity using the Weather Research and Forecasting model

Hannah Nissan

December 2013

Space and Atmospheric Physics Group
Department of Physics
Imperial College London

Thesis submitted for the degree of

Doctor of Philosophy of Imperial College London

Supervisor

Prof. Ralf Toumi

Examiners

Dr. Adrian Hill

Prof. Joanna Haigh

For my grandfather

Statement of originality

I declare that this thesis is my own work, except where work by others has been properly referenced.

Publications

The research presented in this thesis has been published in the following articles:

- Nissan, H., and R. Toumi, 2013. Dynamic simulation of rainfall kinetic energy flux in a cloud resolving model. Geophysical Research Letters 40 (22), 5997-5998.
- Nissan, H., and R. Toumi, 2013. On the impact of aerosols on soil erosion. Geophysical Research Letters 40 (12), 3331-3336.

Copyright

Acknowledgments

I am grateful to Ralf Toumi for his supervision and for many interesting discussions relating to this work. I would also like to thank Adrian Hill and Joanna Haigh for examining this thesis, and Rachel White for training me at the beginning of my studies. Thank you Lionel, and my parents, brother and grandparents for your faith in me and for all your support.

This work was funded by the Natural Environment Research Council.

Abstract

Soil erosion is a serious threat to agricultural productivity and the sustainable provision of food to a growing world population. Current erosion models employ simplistic treatments of rainfall. This thesis presents a new approach to erosion modelling, using the Weather Research and Forecasting model to simulate rainfall erosivity, an indicator of the erosive capacity of rain.

Rainfall erosivity is modelled in the Caucasus region, an area vulnerable to erosion and climate change pressures. Low intensity rainfall (below $2\,\mathrm{mmhr}^{-1}$) is found to contribute significantly to erosivity (23%), contrary to common assumptions. An exponential dependence of the fraction of erosivity from light rain on the proportion of light rain is found. Erosion models focus on storms, but results suggest that storm-based calculations may exclude up to 30% of erosivity. In the Universal Soil Loss Equation, this does not lead to errors in long term soil loss but could cause an underestimation of event erosion.

Rainfall kinetic energy flux is an important variable in erosion prediction and is routinely parameterised from intensity. Here this is dynamically simulated from basic physics in a cloud resolving model, using four microphysics schemes. Results are within the range of observations and capture the observed variability in kinetic energy for a given intensity, where current methods fail. Large raindrops are shown to contribute disproportionately to total kinetic energy, and also to surface precipitation, compared with their number.

No connection has hitherto been drawn between aerosols and soil erosion. The effect of aerosols on rainfall erosivity is investigated in a cloud resolving model. Aerosols can either enhance or suppress precipitation. In both these cases the response of erosivity to a rise in aerosols is in the same direction as, but amplified beyond, the change in total rain. It is also shown that aerosols can influence erosivity by changing raindrop sizes. These results suggest that anthropogenic aerosol emissions affect erosivity and thus may have important consequences for agricultural productivity.

Contents

List of Figures

List of Tables

1 Introduction

1.1 Precipitation and the hydrological cycle

1.1.1 Constraints on the hydrological cycle

Global mean precipitation and evaporation rates are controlled by the surface energy budget [*Allen and Ingram*, 2002]. Short wave solar radiation warms the earth's surface, which emits long wave radiation to the troposphere. The troposphere cools by radiating to space and back to Earth. Long wave radiation emitted from the surface is accompanied by an upwards latent heat flux, as potential evapotranspiration increases with surface temperature [*Trenberth et al.*, 2003; *Allen and Ingram*, 2002; *Pall et al.*, 2007]. Evaporation cools the surface and condensation warms the troposphere, opposing the radiative effects. These different processes must balance, and the strength of the hydrological cycle is limited by the ability of the troposphere to radiate energy away. This ultimately determines the global average rain rate, which must balance the evaporation rate [*Allen and Ingram*, 2002]. In a warming climate, this leads to an intensification of the global hydrological cycle [*Trenberth*, 1999].

Local precipitation intensity, however, often greatly exceeds the locally available water vapour supplied by evaporation. Heavy rain events are instead fuelled by large scale transport of moisture from other regions, as local evaporation could sustain only light rainfall [*Trenberth et al.*, 2003]. Transport and moisture availability are therefore the main limiting factors in local rainfall intensity.

The atmospheric moisture content is controlled by thermodynamics. Saturation vapour pressure is the partial vapour pressure exerted by a gas when in equilibrium with its liquid phase. In equilibrium, the ambient vapour pressure and the saturation vapour pressure are equal. If the ambient vapour pressure is less than the saturation pressure evaporation occurs, and in the reverse case water vapour condenses. The saturation vapour pressure of water is therefore used as a measure of the water

holding capacity of the atmosphere. This concept is encapsulated in the expression for the saturation ratio, S (also called the relative humidity), which gives the ratio of the partial vapour pressure of water in the air, e, to the saturation vapour pressure over water, $e_s(T)$ [*Rogers and Yau*, 1989]:

$$S = \frac{e}{e_s(T)} \tag{1.1}$$

Saturation ratios in excess of one are common in clouds; this is discussed further in sec. 1.2. When this occurs the supersaturation is defined as

$$s = S - 1 \tag{1.2}$$

The Clausius-Clapeyron relation describes the evolution of saturation vapour pressure, and thus the water holding capacity of the air, with temperature. In the case where air behaves as an ideal gas, and for the particular case of the phase transition from water vapour to liquid water in the atmosphere, it can be written as

$$\frac{de_s}{dT} = \frac{Le_s}{R_v T^2} \tag{1.3}$$

where T is temperature, L is the latent heat of vaporisation (the energy needed to transform a given quantity of liquid into a gas at constant pressure) and R_v is the gas constant for water vapour [*Andrews*, 2010]. Saturation vapour pressure is an increasing function of temperature (equation 1.3). This explains how clouds form in the atmosphere: rising moist air, cooling at the lapse rate of temperature, experiences a decrease in saturation vapour pressure and an increase in the saturation ratio (equation 1.1) until water condenses [*Andrews*, 2010].

The implication of equation 1.3 is that a warmer atmosphere can hold more water vapour [*Lenderink and van Meijgaard*, 2010], as the maximum vapour pressure before condensation occurs is greater at higher temperatures. For typical atmospheric conditions, the scaling of e_s with temperature is approximately 6.5 - 7.5%K^{-1} [*Lenderink and van Meijgaard*, 2008; *Boer*, 1993; *Wentz et al.*, 2007; *Held and Soden*, 2006]. Observations of atmospheric moisture content provide confirmation of this, showing an increase with temperature in broad agreement with thermodynamic theory [*Trenberth et al.*, 2003; *Wentz et al.*, 2007; *Liepert and Previdi*, 2009].

There are different physical processes occurring during heavy precipitation, drought, and in the overall mean. These are summarised in Fig. 1.1. It is widely argued that the heaviest rainfall is constrained by thermodynamics, as opposed to large scale dynamics or the surface energy budget [*Allen and Ingram*, 2002; *Berg et al.*, 2009; *Lenderink and van Meijgaard*, 2009]. The moisture holding capacity of the atmosphere increases with temperature according to the Clausius-Clapeyron relation, and assuming that relative humidity is largely unchanged (a generally accepted, though not undisputed result [*Allen and Ingram*, 2002; *Held and Soden*, 2006]), the actual water vapour content of the atmosphere increases at the same rate. In the most extreme precipitation events, when all available moisture is precipitated, it therefore follows that precipitation intensity may also scale with temperature at the Clausius-Clapeyron rate of approximately $7\%\mathrm{K}^{-1}$ [*Allen and Ingram*, 2002; *Pall et al.*, 2007; *Lenderink and van Meijgaard*, 2008, 2010; *Haerter et al.*, 2010].

This contrasts with mean local precipitation which, as a combination of all types of precipitation, from low frequency drought conditions to heavy convective rain showers, is a superposition of different physical processes, and as such is not constrained by any one physical condition. Large scale circulation patterns which have an impact on the frequency of precipitation and the transport of moisture are of relevance here, as are the thermodynamic constraints on the upper quantiles of rainfall discussed previously.

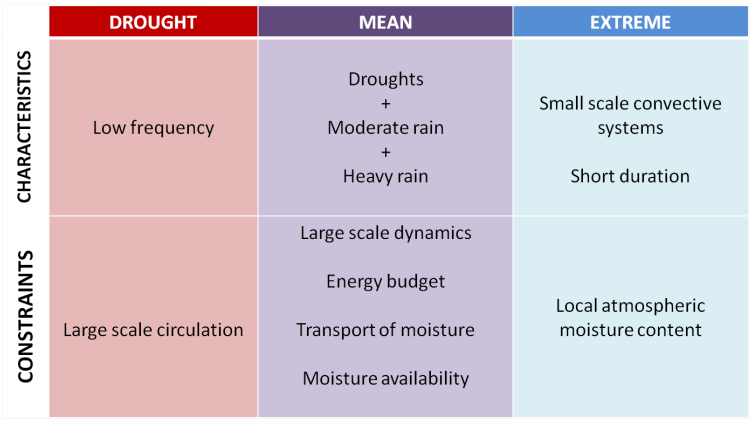

Figure 1.1: The physical constraints on precipitation.

1.1.2 Climate change

The climate has warmed since the mid 20th century, and evidence for this is now unequivocal. With 95% certainty, anthropogenic emissions of greenhouse gases are the dominant cause of this observed warming [*IPCC*, 2013]. Greenhouse gases in the atmosphere absorb infrared radiation emitted by the earth's surface and reemit this, both to space and back to Earth. Rising concentrations of these gases in the atmosphere enhance this effect, increasing the overall downwelling infrared radiation and warming the surface [*Boer*, 1993]. There are many feedback effects which either amplify or reduce the equilibrium response, but the net effect is a positive radiative forcing and a warming of the climate system. Furthermore, emissions continue to rise and are extremely long lived in the atmosphere, so projecting future impacts of this on the earth systems is extremely important [*Solomon et al.*, 2007; *IPCC*, 2013].

1.2 Microphysics

Microphysics is the physics of clouds and precipitation at very small scales. The processes which occur on these scales are of direct relevance to the wider climate and meteorology. Clouds have a direct effect on the radiation budget of the Earth and have been identified as one of the key uncertainties in projecting future climate change [*IPCC*, 2007]. Microphysical processes also influence atmospheric dynamics through latent heating and evaporative cooling. As computational capabilities improve, climate and numerical weather prediction models will continue to increase in spatial and temporal resolution, rendering some parameterisation schemes useless as more processes are explicitly resolved. However, microphysics schemes will never be obsolete because the physics involved goes down to the molecular scale.

The focus of this thesis is rainfall driven soil erosion, and this section will therefore concentrate mainly on liquid precipitation, incorporating a briefer discussion of ice phase cloud processes.

1.2.1 Key microphysical processes

Nucleation

Updrafts causing air parcels to rise and cool in the atmosphere can easily achieve a saturation ratio of one (equation 1.1). Despite this, pure water droplets do not form easily in the atmosphere, requiring substantial supersaturation levels. Instead, cloud droplets are observed to form on aerosol particles which act as condensation nuclei (CN). This can be understood with two key results: the Kelvin effect and Raoult's law [*Andrews*, 2010; *Rogers and Yau*, 1989; *Young*, 1993].

Recall that the saturation vapour pressure is the vapour pressure above which condensation occurs. The Kelvin effect states that the saturation vapour pressure over a spherical drop is greater than over bulk water:

$$e_s(T, r) = e_s(T, \infty) \exp\left[2\sigma / r R_v T \rho_w\right] \tag{1.4}$$

where $e_s(T, r)$ is the saturation vapour pressure over a spherical drop of radius r with surface tension σ and density ρ_w, at temperature T. R_v is the gas constant for water vapour and $e_s(T, \infty)$ is the saturation vapour pressure over bulk water; this is equivalent to $e_s(T)$ in equations 1.1 and 1.3.

Raoult's law finds that the presence of a solute (a dissolved CN) reduces the saturation vapour pressure:

$$\frac{e'_s(T, \infty)}{e_s(T, \infty)} = \frac{n_0}{n + n_0} \tag{1.5}$$

In equation 1.5 $e'_s(T, \infty)$ is the saturation vapour pressure over a bulk solution consisting of n molecules of water and n_0 of solute.

These two results combine to produce the Köhler curve for the equilibrium saturation ratio, S_{eq}, over a solution droplet, which can be approximated as:

$$S_{eq} = \frac{e'_s(T, r)}{e_s(T, \infty)} = 1 + a/r - b/r^3 \tag{1.6}$$

for $a = 2\sigma / R_v T \rho_w$ and $b = 3 i m_v M / 4\pi \rho_w m_s$, with i a measure of the degree of ionic dissociation, m_v and m_s the molecular weights of water and the solute, and M the

mass of the drop [*Young*, 1993]. Saturation is reached when the ambient vapour pressure $e(T) = e'_s(T, r)$, corresponding to a saturation ratio $S > 1$ (equations 1.1 and 1.6).

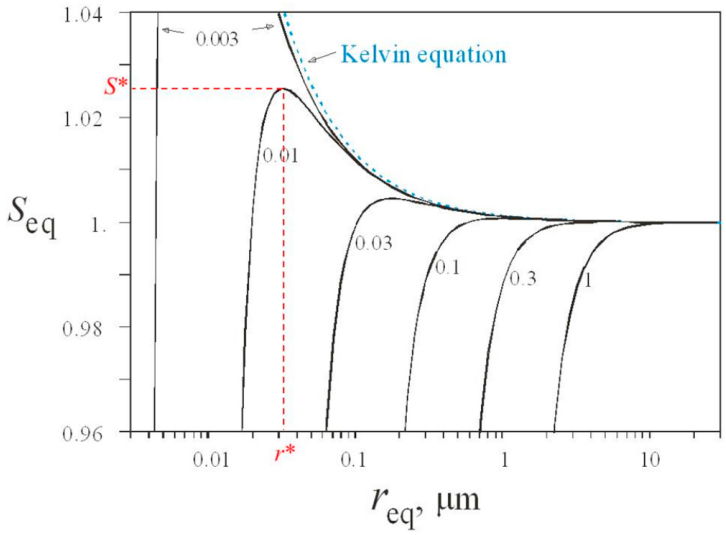

Figure 1.2: Equilibrium saturation ratio, S_{eq} (equation 1.6), for solute drops formed from CN of different sizes (lower curves, with the radii indicated in μm) and over a pure water drop (upper curve indicated as the Kelvin equation), as a function of equilibrium radius, r_{eq}. r^* is the activation radius for a 0.01 μm CN particle, which is reached when the saturation ratio is S^*. Adapted from *Tao et al.* [2012]

Fig. 1.2 illustrates this result. If the ambient $S > S_{eq}$ for a drop, it will grow by diffusion, and in the reverse case it will evaporate. Small solute drops (at radii smaller than the curve maxima in Fig. 1.2) are in stable equilibrium; a perturbation which slightly increases the radius of the drop causes S_{eq} to increase above S, and evaporation shrinks the drop back to its original size. For the droplet to grow in this situation, S must increase. When the droplet reaches the critical radius r^* where the slope becomes negative (which requires a degree of supersaturation since $S^* > 1$), it is in unstable equilibrium with the environment. A small increase in the drop size lowers S_{eq} below the ambient value S, which causes further condensation and the droplet continues to grow. Conversely, above the critical radius the drop will evaporate until it reaches the critical radius if perturbed in that direction. When a CN reaches the critical radius by diffusion of water vapour, it has been 'activated' and can grow into a cloud droplet; CN large enough to be activated at ambient supersaturation levels are called cloud condensation nuclei (CCN). The degree of

supersaturation needed to activate a CN decreases with CN radius (Fig. 1.2) [*Pruppacher and Klett*, 1997]. If the ambient supersaturation is changing rapidly in a cloud, then the kinetic processes may lag behind the thermodynamics, and nuclei may not be able to reach equilibrium on their Köhler curves [*Young*, 1993].

A pure water drop (upper curve in Fig. 1.2) is always in unstable equilibrium, and once formed can grow freely. However, the supersaturation required for a pure water droplet to form is so high that in practice this never occurs because of the presence of ample soluble aerosols, which act as CCN by allowing droplets to form at much lower supersaturations [*Pruppacher and Klett*, 1997].

The number of activated CCN, N_{CCN}, is often approximated by a power law distribution [*Twomey*, 1959; *Pruppacher and Klett*, 1997]:

$$N_{CCN} = cs^k \tag{1.7}$$

where s is the supersaturation (%) and c and k are local constants. *Twomey* [1959] related the number of activated CCN to the maximum supersaturation reached during ascent in the cloud, which in turn depends on the vertical velocity, w:

$$N_{CCN} = 0.88c^{\frac{2}{k+2}} \left[0.07 + w^{\frac{3}{2}}\right]^{\frac{k}{k+2}} \tag{1.8}$$

The maximum cloud droplet concentration is then determined by the number of activated CCN following a one-to-one relationship [*Twomey and Warner*, 1967].

The process of ice nucleation is less well understood. Homogeneous deposition, in which gaseous water molecules spontaneously form an ice embryo, is thought to require extreme supersaturations which never occur in the natural atmosphere. Ice crystals can also form when liquid cloud droplets freeze. This requires the presence of ice nuclei, because spontaneous freezing of cloud drops would require temperatures as cold as -40°C for very small droplets, and slightly warmer for larger ones. Ice nuclei can assist in initiating the nucleation of crystals in three main ways: by serving first as condensation nuclei and then as freezing nuclei, by initiating freezing as soon as they come in contact with a supercooled liquid droplet, or by being absorbed into a supercooled droplet and then causing it to freeze [*Rogers and Yau*, 1989]. Despite the existence of these mechanisms which enable ice crystals to form, supercooled water is common in clouds above the 0°C level in the atmosphere, and has been

observed at temperatures as low as -37.5°C [*Rosenfeld and Woodley*, 2000]. This is because there is a dearth of suitable ice nuclei in the atmosphere, in contrast with condensation nuclei which exist in abundance.

Growth

Condensation nuclei reach their critical radius and then grow beyond this size into cloud droplets by diffusion at a rate which satisfies the diffusion equation, in which D is the molecular diffusion coefficient and ρ_V is the vapour density [*Young*, 1993]:

$$\frac{\partial \rho_V}{\partial t} = -D\nabla^2 \rho_V \tag{1.9}$$

From this, the mass flux of water vapour through the spherical surface of a drop, F_V, is

$$\mathbf{F}_V = 4\pi r^2 D \frac{d\rho_V}{dr} \tag{1.10}$$

Associated with this phase change is a release of latent heat, $L\mathbf{F}_V$ where L is the latent heat of condensation, which warms the droplet relative to its surroundings [*Rogers and Yau*, 1989]. This acts to lower the mass flux, which depends on the density gradient. Heat diffuses away from the droplet according to an analagous equation, where K is the heat diffusivity and T is the temperature:

$$\frac{\partial T}{\partial t} = -K\nabla^2 T \tag{1.11}$$

The heat flux away from the drop, $\mathbf{F}_H$, can be expressed similarly to equation 1.10:

$$\mathbf{F}_H = 4\pi r^2 K \frac{dT}{dr} \tag{1.12}$$

In equilibrium, the latent heat released at the droplet surface balances the sensible heat flow away from the droplet,

$$\mathbf{F}_H = -L\mathbf{F}_V \tag{1.13}$$

An approximate analytical solution to this system [*Young*, 1993] for the rate of growth of a droplet of radius r is:

$$r\frac{dr}{dt} = \frac{S - 1 - \frac{a}{r} + \frac{b}{r^3}}{\left[\frac{L^2}{KR_VT_\infty^2} + \frac{R_VT_\infty}{De_{s,\infty}}\right]} \tag{1.14}$$

where now the subscript ∞ refers to ambient conditions away from the droplet and $S = {}^{e_\infty}/_{e_{s,\infty}}$ is the ambient saturation ratio. a and b are the coefficients from equation 1.6. Equation 1.14 demonstrates that smaller drops grow faster by diffusion than larger drops. If $S < 1 + \frac{a}{r} - \frac{b}{r^3}$, the drop evaporates and r decreases. The approximations made in this derivation can lead to errors, particularly for evaporating drops [*Young*, 1993].

However, this does not account for competition among growing droplets in an environment of limited supersaturation. The evolution of supersaturation with time is expressed by the supersaturation equation:

$$\frac{ds}{dt} = Q_1\frac{dz}{dt} - Q_2\frac{d\chi}{dt} \tag{1.15}$$

where Q_1 and Q_2 are terms consisting of thermodynamic variables. The first term in equation 1.15 expresses the production of supersaturation by updrafts (dz/dt is the vertical air velocity), which cool the air and reduce $e_{s,\infty}(T)$. The second term is the removal of supersaturation by condensation onto cloud and raindrops, at a rate given by $d\chi/dt$ where χ is the mass of condensed water vapour [*Rogers and Yau*, 1989; *Twomey*, 1959]. These competing effects result in a peak in supersaturation usually within the first 100 m of a cloud base, above which a roughly constant value is approached. As a consequence of this, most cloud droplets are produced in the lower part of the cloud where supersaturation is greatest, following equation 1.7 [*Rogers and Yau*, 1989].

The saturation vapour pressure over a liquid drop is considerably greater than over an ice crystal [*Young*, 1993]. After nucleation of an ice crystal in a supercooled water cloud, the environment will be highly supersaturated with respect to ice, and only moderately so with respect to water. The environment is favourable for ice crystal growth by diffusion as long as supercooled liquid water is present to replenish the water vapour by evaporation. If all the liquid drops evaporate or sediment out of the cloud, the removal of water vapour by diffusion onto the ice crystals will reduce the supersaturation until equilibrium is reached with the ice phase, in a similar way to the process of diffusion described for liquid water. Diffusional growth of ice particles

can be described similarly to liquid drops, but solving the growth equation (1.9) is more challenging owing to the complex shapes of ice crystals [*Rogers and Yau*, 1989].

A further consequence of the lower saturation vapour pressure over ice than over liquid water arises when the environment is supersaturated with respect to ice but subsaturated with respect to water. In this scenario ice crystals can grow quickly by the Bergeron process, in which supercooled water evaporates rapidly and is deposited by diffusion onto an ice crystal [*Pruppacher and Klett*, 1997].

Coalescence

Growth by diffusion is important for cloud droplets, but alone cannot account for the development of precipitating raindrops within the time generally observed between a cloud developing and rainfall reaching the ground, usually around 20 minutes. Collision and coalescence between droplets takes over above a radius of about 20 μm [*Rogers and Yau*, 1989]. In order for collisions to occur, there must be sufficient breadth in the droplet size distribution for particles to have significantly different fall speeds. Only then can larger water drops catch up with smaller ones and coalesce to form raindrops. Turbulent mixing and entrainment of air at the cloud edges, which mixes air parcels with different histories, is thought to cause the droplet spectrum to broaden so that this process can be initiated [*Rogers and Yau*, 1989; *Young*, 1993]. In particular, it is the presence of a few large drops that triggers the process, as small droplets do not readily collide with others.

The problem is simplified by restricting the analysis to two spherical interacting particles. The stream flow around a falling drop will tend to deflect particles in its close vicinity, particularly smaller drops which have low inertia. As a result, the effective volume swept out by a large collector drop (termed the collection kernel, Γ) is not simply a function of its size [*Young*, 1993]:

$$\Gamma = \pi R^2 (\nu_L - \nu_S) \tag{1.16}$$

Here R is the radial distance, from the fall axis of the collector drop, within which all small drops are collected. The collector drop falls at speed ν_L, while the population of small drops fall at ν_S. The collection rate is the product of the collection kernel and the concentration of the small drops, N_S:

$$\frac{dN_S}{dt} = \pi R^2 N_S(\nu_L - \nu_S) \tag{1.17}$$

In fact, colliding drops do not always coalesce to form a larger drop. They may bounce apart, coalesce permanently or temporarily, or break into many smaller fragments [*Rogers and Yau*, 1989]. The collision efficiency, ξ_{col}, is a measure of the likelihood of a particle to collide with others during its fall, and increases with size [*Young*, 1993]:

$$\xi_{col} = \frac{R^2}{(r_L + r_S)^2} \approx \frac{R^2}{r_L^2} \tag{1.18}$$

In equation 1.18, r_L and r_S are the radii of the collector and collected drops.

The coalescence efficiency is the ratio of the number of permanent coalescences to collisions. The overall collection efficiency, ξ, is then the product of the collision and coalescence efficiencies, encapsulating the overall effectiveness of the collision-coalescence process [*Rogers and Yau*, 1989]. This leads to the collection equation, in which the number of collected small drops increases with the collector drop size:

$$\frac{dN_S}{dt} = \pi r_L^2 \xi N_S(\nu_L - \nu_S) \tag{1.19}$$

Other factors which influence the collection efficiency are the angle of impact, surface tension of the colliding particles, electric charges, relative humidity and ambient pressure and temperature [*Testik and Barros*, 2007; *Pruppacher and Klett*, 1997].

The diffusional growth process is more efficient for ice than for liquid water, because its lower equilibrium saturation ratio means the atmosphere can more easily be supersaturated with respect to ice. Ice crystals can sometimes grow sufficiently to fall to the ground as precipitation without combining with other particles on the way. Nonetheless, most precipitation particles are larger than this, and these may only develop within reasonable time frames by aggregation or accretion. Aggregation is the combination of several ice crystals to form snowflakes. Accretion describes the collision of a large fast falling particle with a small slow moving one; coalescence of liquid drops normally happens by accretion. In a mixed phase cloud, graupel is produced when a large snowflake or frozen drop catches up with a smaller supercooled water drop, freezing immediately upon contact and creating an outside layer of rime (hard white ice). Hail are denser ice particles which form similarly by accretion of

supercooled drops by ice particles, but in this case the freezing process is more gradual [*Pruppacher and Klett*, 1997; *Rogers and Yau*, 1989]. As for the liquid phase, these processes require a consideration of collection efficiencies, but the problem of estimating these is compounded by the complicated shapes of ice particles.

Breakup

Raindrop breakup can either occur as a result of collision with another particle, or because of hydrodynamic instability. The larger the drop, the greater the difference in pressure between the lower and upper edge as it falls. At some critical equivalent diameter (the diameter of a spherical drop of equivalent volume), usually about 6-8 mm [*Testik and Barros*, 2007], these effects override the surface tension effects that act to retain a spherical shape, the drop becomes hydrodynamically unstable and breaks apart. The internal circulation of the raindrops can also induce spontaneous breakup.

Collision induced breakup can be understood in the context of collection efficiencies, discussed in the previous section. Successful particle collection occurs when a collision results in the permanent coalescence of two drops. Conversely, drop breakup occurs when a collision does not result in permanent coalescence, and the two drops split apart. The probability of drop breakup is therefore 1-ξ_{coal}, where ξ_{coal} is the probability of coalescence given that a collision has occurred. Physically, breakup will occur after a collision if the rotational energy after impact exceeds the surface energy acting to hold the child drop together. This may either produce two resultant drops, or multiple satellite drops [*Young*, 1993].

1.2.2 Particle size distributions

Natural rain consists of drops of varying sizes (e.g. *Laws and Parsons* [1943]; *Marshall and Palmer* [1948]). Given the complexity of interactions within clouds and variations in environmental conditions between clouds and regions it is surprising that observations converge towards quite similar average drop spectra [*Srivastava*, 1971]. This has historically been understood from the perspective of raindrop collisions driving the breakup of drops and ultimately producing observed equilibrium size distributions [*Martinez-Casasnovas et al.*, 2002; *Srivastava*, 1971; *Testik and Barros*, 2007; *Rogers and Yau*, 1989]. However, recent work by *Villermaux and*

Bossa [2009] demonstrates that the forces on a single drop falling through air can cause sufficient fragmentation and breakup to produce observed drop size distributions on timescales much shorter than the typical collision time between raindrops, which these authors say is too long for this to be the primary driver of drop breakup. This is consistent with work by *Srivastava* [1971], who predicted that drop breakup was important during intense rainfall when drops are large and unstable, but authors who promoted the idea stressed the combined roles of collision, coalescence and breakup. There is continuing debate about the relative importance of drop collision and single drop fragmentation [*Niu et al.*, 2010; *Kostinski and Shaw*, 2009; *Barros et al.*, 2010; *Villermaux and Bossa*, 2010; *Testik and Barros*, 2007].

There is much discussion in the literature concerning the appropriate form for the raindrop size distribution (DSD). An exponential formulation was originally proposed by *Marshall and Palmer* [1948], based on data captured by *Laws and Parsons* [1943]:

$$N(D) = N_0 \exp(-\lambda D) \tag{1.20}$$

where $N(D)$ is the number of drops of diameter D mm per unit volume and the intercept, $N_0 = 8 \times 10^3\,\mathrm{m}^{-3}\mathrm{mm}^{-1}$. The data showed a broadening of the distribution with increasing rainfall intensity, i (mmhr^{-1}), reflected by a decrease in the slope parameter, λ, as raindrops become larger:

$$\lambda = 41 i^{-0.21} \mathrm{c}m^{-1} \tag{1.21}$$

The expontial DSD has been found to be a good approximation of the average spectrum in many situations [*Rosenfeld and Ulbrich*, 2003; *Rogers and Yau*, 1989]. However, a number of studies have also shown deviations from exponentiality. In particular, this approximation tends to overestimate the number of small drops [*Rosenfeld and Ulbrich*, 2003; *Ulbrich and Atlas*, 2007]. *Willis* [1984] found that the exponential distribution overestimated the number of small and large raindrops in measurements taken during two hurricanes, and that this could be improved with the use of a three parameter gamma distribution:

$$N(D) = N_0 D^{\mu} \exp(-\lambda D) \tag{1.22}$$

The shape parameter, μ, is a measure of the relative dispersion or width of the distribution. *Smith* [2003] compared the two forms and concluded that where the primary interest is bulk quantities such as rainfall rate, liquid water content and reflectivity, the difference between them is minimal, and the additional mathematical complexity of the gamma distribution is therefore unnecessary. Others have shown that numerical simulations of microphysical processes can be affected by the DSD formulation [*Willis*, 1984; *Abel and Boutle*, 2012]

Alternative formulations have been proposed, including a Weibull [*Best*, 1950] and a log-normal [*Feingold and Levin*, 1986] distribution. However, the gamma and exponential distributions have endured, and it is these two forms which are used in most modern microphysical parameterisation schemes. This is partly because of the relative ease with which functions of the DSD in a generalised gamma or exponential form may be integrated [*Cohard and Pinty*, 2000].

The average size distribution of cloud droplets has a more pronounced positive maximum than raindrops, and therefore is better represented by a gamma or log-normal particle size distribution (PSD). However, the spectrum of droplets varies greatly between clouds and regions, and during the different phases of cloud development. This is largely due to the concentration of CCN, which alters not only the mean droplet size but also the width of the PSD (sec. 1.2.5). Some bimodal cloud spectra have been observed, which can be represented mathematically by superposing two unimodal distributions, but most microphysics models use a gamma or even exponential PSD for simplicity [*Pruppacher and Klett*, 1997; *Rogers and Yau*, 1989].

Observations of PSDs for ice-phase particles are more scarce [*Pruppacher and Klett*, 1997]. *Gunn and Marshall* [1958] found that the distribution of snowflakes could be expressed in terms of the equivalent diameter of a melted snowflake with an exponential formulation as in equation 1.20, but with $N_0 = 3.810 \times 10^3 i^{-0.87}\,\mathrm{m^{-3}mm^{-1}}$ and $\lambda = 25.5 i^{0.48}\,\mathrm{cm^{-1}}$. This was confirmed by other studies, though different behaviours of the intercept and slope were found: *Sekhon and Srivastava* [1970] suggested a different fixed value for N_0 and for the variation of λ with i, while *Woods et al.* [2008] found a temperature dependence for N_0. Fits for actual (frozen) snowflake diameters produced consistent results, though deviations from exponential behaviour have also been found, in particular "sub-exponential" and "super-exponential" PSDs in weak stratiform and convective cloud regions, respectively [*Pruppacher and Klett*, 1997]. For graupel and hail, most research indicates that an exponential PSD is

also suitable, again with some variation in the intercept parameter [*Pruppacher and Klett*, 1997].

1.2.3 Size and shape of particles

The mass of most hydrometeors can conveniently be represented using a simple power law expression:

$$M(D) = cD^d \tag{1.23}$$

where c and d are constants. Most particles can be approximated as spheres, with d=3 and $c = \pi\rho_p/6$ where ρ_p is the particle density. However, deviations of raindrops from sphericity are well documented [*Szakáll et al.*, 2010; *Pruppacher and Klett*, 1997]. In fact, only drops smaller than about 1 mm meet this assumption (Fig. 1.3). Larger drops become progressively more deformed by the drag force acting against their fall, and are considerably more oblate in shape [*Villermaux and Bossa*, 2009; *Testik and Barros*, 2007].

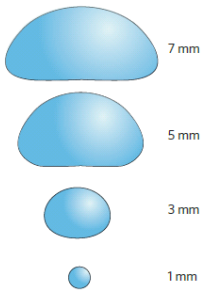

Figure 1.3: The increasing oblateness of raindrops with size. Taken from *Kostinski and Shaw* [2009].

Ice crystals have an array of different shapes, but empirical fits to observations have shown that a power law relation works reasonably well, with d on the order of 2 or 3. The same is true for aggregate snowflakes, though there are limited observations, and d is rather lower, between 1.4 and 2.2. Graupel and hail fit a spherical approximation and power law mass relation fairly well, but the density of graupel varies greatly because it can be formed in different ways (e.g. by snowflakes or ice crystals interacting with cloud droplets in different environments) [*Pruppacher and Klett*, 1997].

1.2.4 Terminal velocity

It is commonly assumed that all sedimenting particles fall at their terminal velocity, defined by a balance between opposing weight and drag forces. Data published by *Laws* [1941], *Gunn and Kinzer* [1949] (Fig. 1.4) and *Beard and Pruppacher* [1969] are among the most commonly cited measurements of the terminal fall speed of water or raindrops, and these observations agree well with each other. *Beard* [1976] developed a set of semi-empirical formulae for the terminal velocity of drops in different flow regimes and found that the results matched well with the measurements from *Gunn and Kinzer* [1949], which are still commonly used as a benchmark for comparison.

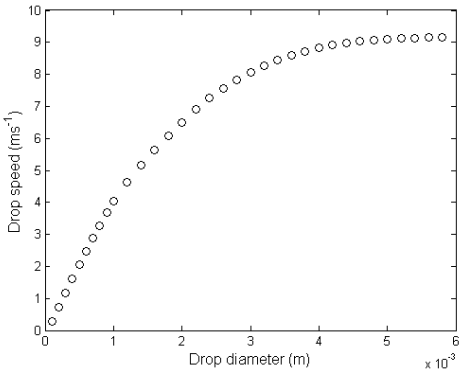

Figure 1.4: Terminal velocity of water drops measured by *Gunn and Kinzer* [1949].

Several fits to these measurements have been proposed [*Atlas et al.*, 1973; *Liu and Orville*, 1969; *Uplinger*, 1981; *Atlas and Ulbrich*, 1977; *Rogers*, 1989; *Rogers and Yau*, 1989]. A common practice in numerical cloud models is to adopt a power law expression, where $V(D)$ is the drop velocity and a and b are empirically determined constants :

$$V(D) = aD^b \tag{1.24}$$

Torres et al. [1994] demonstrated that all empirical fits to observed DSDs could be understood as particular forms of a generalised DSD formulation. This enabled them to relate bulk rainfall variables to one another as power laws so long as terminal velocity was also related to drop diameter by a power law. The appeal of simple power law relations between variables, and the relative ease of integrating power law functions in simulations, has led to the adoption of power law velocity fits in several microphysics parameterisation schemes. Some researchers have pointed out

the failure of a straight power law function to account for the saturation of velocity with drop size. This arises because of the increasing oblateness of raindrops with size; the drag on an oblate drop is greater than on a spherical one of equivalent volume [*Atlas et al.*, 1973; *Van Dijk et al.*, 2002].

The assumption that particles fall at terminal velocity has not gone unchallenged. *Montero-Martinez et al.* [2009] observed both sub- and super-terminal velocities during natural rainfall events near Mexico City. During coalescence between a small (slow) and a large (fast) drop, immediately after impact the resultant particle travels at a speed slightly slower than the large parent drop. When drop breakup produces several satellite fragments, immediately after breakup these all travel at the same speed. This speed is equal to the intial speed of the parent drop, and is therefore larger than the terminal fall speed of the small fragments. *Montero-Martinez et al.* [2009] found that small drops sometimes travel at speeds which are orders of magnitude larger than their terminal velocities, while the sub-terminal speeds of larger drops were modest. *Villermaux and Eloi* [2011] showed that these results are consistent with their finding [*Villermaux and Bossa*, 2009] that single drop fragmentation can account for the *Marshall and Palmer* [1948] exponential DSD.

1.2.5 Aerosol effects on clouds and precipitation

Aerosols are small airborne particles of varying chemical composition which may be of natural or anthropogenic origin. The impacts of aerosols on the climate system are far reaching, and may be divided into their direct and indirect effects [*IPCC*, 2007]. The direct effects are the absorption and scattering of short and long wave radiation by aerosols that alter the energy balance of the system. This can also have an impact on precipitation, as the absorption of radiation by aerosols reduces surface heating and stabilises the lower atmosphere [*Rosenfeld et al.*, 2008]. The indirect effects refer to the influence of aerosols on the microphysical properties of clouds, which in turn alter their radiative properties and have consequences for precipitation. This discussion focusses on the microphysical impacts of aerosols on clouds and the consequences for precipitation, excluding radiative effects. This provides the background for chapter 5, which presents simulations of the influence of aerosols on precipitating clouds in an idealised model with no radiation.

Understanding the effects of aerosols on precipitation processes remains challenging, depending on a complex balance of microphysical and dynamic factors [*Khain*

et al., 2005; *Tao et al.*, 2012; *Lee et al.*, 2008]. The outcome for surface precipitation ultimately depends on competing processes of condensate generation and loss (condensation and evaporation), both of which are higher in polluted clouds and are affected by cloud type and environmental conditions [*Khain et al.*, 2005; *Khain*, 2009; *Igel et al.*, 2013; *Lee et al.*, 2008].

The microphysical effects begin with the tendency of aerosols to increase the concentration of cloud droplets by acting as CCN. For a given liquid water content, this leads to smaller cloud droplets as the same mass of water is distributed among a larger population of droplets [*Squires*, 1958; *Squires and Twomey*, 1960; *Twomey*, 1977]. Competition among a larger number of droplets reduces the maximum supersaturation reached, raising the minimum cutoff size for CN activation (Fig. 1.2) and reducing the breadth of the distribution [*Squires*, 1958; *Tao et al.*, 2012]. The narrower droplet spectrum, combined with the reduced collision efficiency of smaller droplets, inhibits the collision and coalescence processes that lead to raindrop formation and suppresses surface rainfall. This in turn can prolong cloud lifetime and increase liquid water content [*Albrecht*, 1989].

The issues are simplified by considering liquid and mixed-phase clouds separately [*Tao et al.*, 2012]. Fully glaciated clouds occurring high in the atmosphere are not considered here. In warm rain clouds, a suppression of precipitation usually occurs because of the microphysical effects described above. This is supported by observations and modelling studies [*Albrecht*, 1989; *Niu and Li*, 2012; *Li et al.*, 2011; *Tao et al.*, 2012; *Fan et al.*, 2012; *Lebsock et al.*, 2008; *Jiang et al.*, 2006]. In addition, more efficient evaporation from smaller cloud droplets prevents them from reaching the surface, further contributing to this result [*Khain et al.*, 2008]. This opposes the influence of increased evaporation in the downdrafts, which acts to invigorate convective overturning [*Rosenfeld et al.*, 2008].

Conversely, in a mixed phase system, these smaller droplets, which survive longer in the cloud, may be lifted to freezing level and serve to invigorate cold-rain formation processes. The associated latent heat release can invigorate convection and push the cloud top higher, where radiative cooling is stronger and can further intensify convection (though the radiative processes would not be included in the model simulations in chapter 5) [*Rosenfeld et al.*, 2008; *Li et al.*, 2011]. Latent heating in the upper levels and subsequent cooling lower down from the melting of falling frozen hydrometeors corresponds to a greater upward heat transport and consumption

of more instability for a given amount of surface precipitation, leading to more overturning convection [*Rosenfeld et al.*, 2008; *Rosenfeld*, 2006]. The result of these processes, illustrated in Fig. 1.5, is a delayed increase in surface rainfall ('aerosol invigoration effect') [*Rosenfeld et al.*, 2008; *Khain et al.*, 2005, 2008; *Tao et al.*, 2012; *Li et al.*, 2011].

This increase in precipitation occurs mostly under conditions of low wind shear, high humidity and atmospheric instability [*Khain et al.*, 2008; *Khain*, 2009; *Fan et al.*, 2009; *Lee et al.*, 2008; *Khain and Lynn*, 2009]. Some studies have found that a decrease in precipitation efficiency can offset the tendency of ice invigoration to increase precipitation [*Khain et al.*, 2005; *Khain*, 2009; *Khain and Lynn*, 2009; *Igel et al.*, 2013]. For instance, smaller particles have lower velocities and evaporate more, tending to reduce surface precipitation. Observations from a variety of sources have confirmed the tendency of aerosols to increase precipitation in mixed phase clouds, and for suppression in warm rainclouds [*Li et al.*, 2011; *Niu and Li*, 2012; *Lebsock et al.*, 2008] but there are also several conflicting or inconclusive results [*Rosenfeld et al.*, 2008; *Lee and Feingold*, 2013; *Igel et al.*, 2013; *Lee et al.*, 2008]. At the global scale evaporation must balance precipitation, and a balance between a reduction in rain from shallow clouds and an increase from deeper clouds is consistent with this constraint [*Rosenfeld et al.*, 2008].

Khain et al. [2008] attempted to classify results from many previous studies by environmental conditions and type of cloud system. This is shown in Fig. 1.6. The diagonal line separates the two possible outcomes, in which either condensate loss ($\triangle L$) or generation ($\triangle G$) dominate, leading to decreasing or increasing precipitation, respectively. In the upper left portion $\triangle L > \triangle G$ and precipitation decreases, while in the lower right segment the reverse is true. The characteristics of the cloud system are important: in isolated clouds mixing with the surrounding environment entrains dry air and increases $\triangle L$, while in cloud clusters, supercell storms and squall lines the convective region is humid and $\triangle L$ is lower. Relative humidity was found to be particularly important because of its influence on the precipitation efficiency, with the potential to reverse the sign of the precipitation sensitivity to aerosols [*Khain et al.*, 2008].

Fan et al. [2009] concluded that in the case of isolated deep convective clouds, wind shear is a more important factor than relative humidity in determining the outcome for surface rainfall. High wind shear suppresses convection by enhancing evaporative

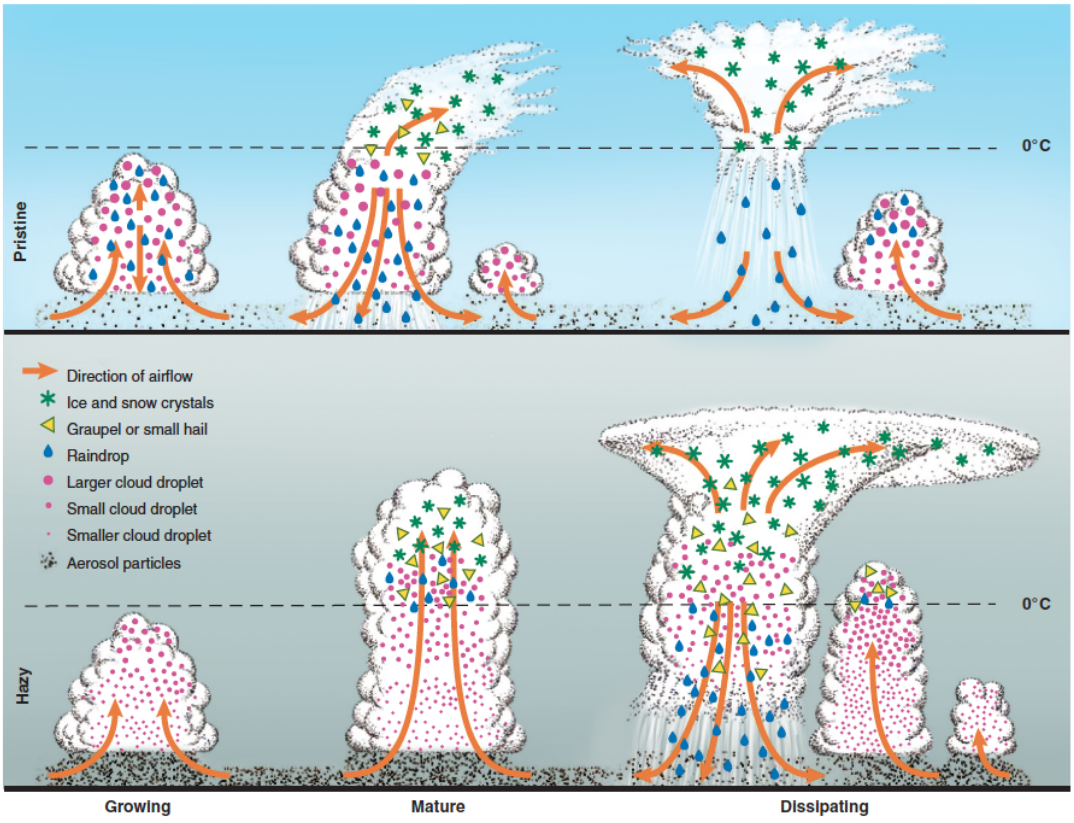

Figure 1.5: Illustration of the aerosol invigoration effect, taken from *Rosenfeld et al.* [2008]. The upper (lower) panel shows the evolution of deep convective clouds under clean (polluted) conditions. In the clean case, cloud droplets coalesce to form raindrops and rain out, while smaller droplets that persist in the cloud freeze onto ice precipitation in the upper cloud levels, which sediments and then melts, reaching the ground as rain. In a polluted environment, smaller cloud droplets cannot form raindrops and are lifted to the supercooled zone, releasing latent heat of freezing and then melting at lower levels, invigorating convection, pushing the cloud top higher and increasing rainfall.

cooling through detrainment of cloud droplets and entrainment of surrounding dry air [*Fan et al.*, 2009; *Lee et al.*, 2008]. This effect will be greater in a more polluted cloud as smaller particles evaporate more quickly (equation 1.14). However, for cloud ensembles, a secondary effect of the increase in evaporative cooling under conditions of high wind shear can be to intensify downdrafts, strengthening the cold pool, increasing convergence in the boundary layer and leading to the formation of secondary clouds and ultimately to an increase in precipitation [*Khain*, 2009; *Khain et al.*, 2005; *Lee et al.*, 2008; *Tao et al.*, 2007]. This is more likely under polluted conditions, when evaporative cooling is stronger.

Atmospheric stability is another important factor, which was investigated by *Lee et al.* [2008] for mesoscale convective systems using a double moment bulk microphysics model. They found that high convective available potential energy (CAPE, corresponding to high instability) and strong wind shear favoured a positive sensitivity of precipitation to aerosols through dynamic effects (enhanced convection and stronger downdrafts), which fostered secondary cloud formation. They found that in this case these dynamic effects were more important than the contribution of ice processes, and *Rosenfeld et al.* [2008] notes that some model simulations show an increase in precipitation without ice processes.

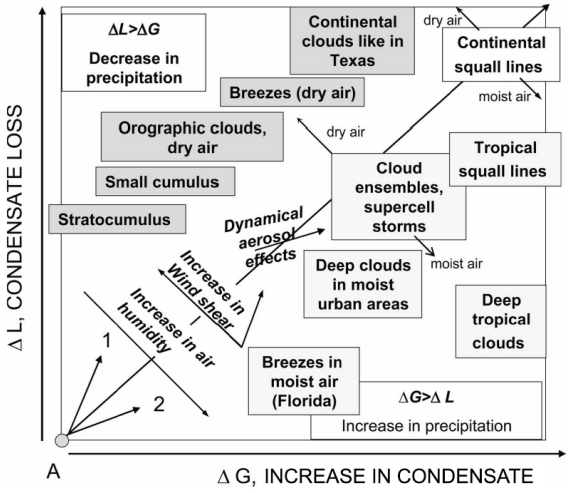

Figure 1.6: Classification of the effects of aerosols on precipitation according to cloud type and environmental conditions. The area above (below) the diagonal line corresponds to an decrease (increase) in precipitation because of a dominance of condensate loss (generation) [*Khain et al.*, 2008].

1.3 Soil erosion

"Without healthy soil, life on Earth is unsustainable."[1] Nearly 2 billion hectares of land, approximately 15% of the earth's surface, suffer from soil degradation as a result of human activities, with over half of all soil erosion caused by water [*Crosson*, 1995; *UNEP*, 2002]. Erosion directly affects food and water security, compromising agricultural productivity and contaminating waterways [*UNEP*, 2007; *Pimentel et al.*, 1995]. Exacerbating this, population growth is exerting increasing pressure on agricultural systems to provide enough food for all [*Pimentel et al.*, 1995; *Yang et al.*, 2003]. In addition, erosion reduces the capacity of land to act as a sink for the greenhouse gas carbon dioxide; up to 20% of carbon stored in eroded soils is released to the atmosphere as CO_2 [*Yang et al.*, 2003]. Uncertainties regarding the effect of a changing climate on food production add to the severity of these concerns.

1.3.1 The mechanical process of soil erosion

There are three phases in the erosion process: detachment, transport and deposition [*Morgan*, 1986]. As in most erosion models, only the first two are considered here. Detachment refers to the separation of individual soil particles from the ground by a detaching agent. The agent must deliver sufficient energy to overcome the friction which binds the soil particles in the earth. The most significant detachment agent is rainsplash, whereby falling raindrops deliver kinetic energy to the soil and may displace soil particles by several centimetres [*Allen*, 1997; *Morgan*, 1986]. Other detachment agents include surface runoff and wind, alternate drying and wetting, freeze-thaw and footfall by people and livestock. These processes loosen the soil and make it more likely that substantial erosion will take place in the presence of a transport agent to remove the detached particles.

The most effective transport agent is surface runoff/overland flow [*Allen*, 1997]. Rills are narrow channels of water flow formed by surface runoff, small enough to be removed by tilling and other farming practices. Transport processes which act uniformly over large areas cause interrill erosion. These include surface runoff when it occurs as a wide, shallow flow (sheet erosion), rainsplash, which can displace soil particles small distances as well as detaching them, and wind [*Morgan*, 1986].

[1] Ban Ki-moon, UN Secretary General, speaking in 2012 at the World Day to Combat Desertification.

From an energy conservation perspective, erosion is a mechanical process for which the energy is provided by the eroding agents. Of all the agents, falling raindrops have the most energy available for erosion, but most of this is spent on detachment, leaving little energy for significant displacement. Acting alone, the most efficient erosive agent is surface runoff concentrated in rills, followed by overland flow/sheet runoff and finally rainsplash. It is when the action of raindrop impact and surface runoff are combined that they cause substantial erosion [*Morgan*, 1986].

Further erosion can be caused by rivers and streams, and by mass soil movements such as landslides or creep, where water inflitrates the soil and loosens it from within [*Morgan*, 1986]. These processes are not considered here.

1.3.1.1 Factors affecting erosion

Erosivity of the eroding agent For both wind and rain, erosivity is related to the energy available to the soil from the eroding agent. The erosivity of rainfall expresses its ability to detach soil particles and to generate surface runoff. The detachment of particles and the formation of surface runoff are also influenced by the erodibility of the soil, terrain slope and vegetation. Rainfall erosivity is the focus of this thesis and is discussed in further detail in the following section.

Slope Erosion is greater on steeper slopes, but a different consideration of terrain slope is required depending on which erosion processes are occurring. Raindrop impact only affects the ground within a few drop widths of the point of impact, so only the slope local to this point is relevant. This term is negligible and is routinely ignored. However, the displacement of soil particles by rainsplash is affected by the average slope, as on a steeper gradient more of these particles are displaced downslope, resulting in net downhill transport. Detachment and transport by surface runoff are strongly dependent on terrain slope, because this exerts a strong control on the generation of surface runoff and its flow velocity [*Morgan*, 1986]. Slope length is also important, and is often combined with slope in erosion models [*Allen*, 1997].

Generation of surface runoff The production of surface runoff depends on several factors including rainfall intensity, slope, vegetation, soil moisture and soil type. Maximum infiltration rates and limiting soil moisture contents control the hydraulic

conductivity of the soil[2] and vary among soil types. In a simplified model, rain falling at intensities up to the maximum infiltration rate are absorbed into the ground, while higher intensity rain produces surface runoff [*Allen*, 1997]. However, the infiltration rate can sometimes increase with rain intensity as heavy rain disrupts soil seals and crusting, and it also varies during a storm [*Morgan*, 1986; *Allen*, 1997]. The limiting soil moisture value also exerts a control on the absorption of rain. When soil moisture is below this value, rain is readily stored in pores within the soil, but above this value ponding and eventually runoff occur. When this is the controlling process, even low intensity rain can generate runoff. Whichever limit is reached first (maximum infiltration rate or limiting moisture content) determines when runoff is produced [*Morgan*, 1986].

Vegetation Vegetation tends to reduce erosion in two ways: by absorbing some of the energy of erosive agents and by strengthening the soil [*Allen*, 1997; *Morgan*, 1986]. A plant canopy reduces the height from which raindrops fall, but for high canopies drops still reach close to terminal velocity. The size distribution of drops is altered by the canopy, with average drop size around twice the average raindrop size. These effects vary with vegetation density and height; between rows of crops for instance, erosion can be increased by a higher concentration of drops falling from leaves, but be reduced under the crops themselves. Plants also intercept running water and wind, tending to reduce the velocity and capacity for erosion in both cases, but again this varies with the type of cover as sparse crops can create channels of higher velocity flow. Vegetation reduces the erodibility of soil, as roots increase cohesion between particles and improve slope stability [*Morgan*, 1986]. Plant roots can also raise the infiltration capacity of soil, allowing more water to be absorbed before runoff occurs [*Allen*, 1997].

Soil erodibility Soil erodibility is the resistance of the soil to the processes of detachment and transport. Many factors contribute to this, including farming practices. Soil texture is related to the size of particles; larger particles are more resistant to transport as their weight requires larger forces to dislodge them, while smaller particles are more resistant to detachment as they tend to be more cohesive. Clay content is often used as an indicator of soil erodibility, as a higher fraction of clay

[2]Hydraulic conductivity is the ease with which water moves through a material.

tends to increase stability. Shear strength and chemical composition are also important. The erodibility affects other erosion processes including the rainfall infiltration capacity and the production of runoff. For example, rain falling on soil with a low soil moisture limit is more likely to result in ponding which, depending on the depth of ponding, can affect the ability of raindrop impact to detach particles [*Morgan*, 1986].

1.3.2 The Universal Soil Loss Equation

In the 1950s, demand for a simple way to estimate annual average soil loss from rainfall by sheet and rill erosion in the United States led to the development of the Universal Soil Loss Equation (USLE, *Wischmeier and Smith* [1978]). Since then this tool has been used extensively all round the world, and continues to be used today. Despite being developed to estimate annual average soil loss from rainfall, the USLE is often used to measure erosion from individual storms [*Kinnell*, 2010]. The equation takes a very simple form:

$$A = RKLSCP \tag{1.25}$$

where A is long term average annual soil loss in units of mass per area per year. The terms L, S (slope length and gradient factors), C (crop management factor), P (support practice factor) and K (soil erodibility) in equation 1.25 are static factors relating to the physical conditions of the soil and are obtained from look-up tables. A unit plot is defined as having a slope of 9%, a length of 72.6 feet, with fallow plot, tillage up and down the slope, and no crop management practices in use. L, S, C and P are dimensionless quantities, and under these conditions $L = S = C = P = 1$. Soil erodibility, K, is the rate of soil loss per unit of R for a given soil on a unit plot:

$$K = A/R \tag{1.26}$$

These factors were experimentally determined when the USLE was first developed in the United States [*Wischmeier and Smith*, 1978], but are nonetheless used in other areas of the world. K values were determined experimentally for different soils. The focus of this research is the rainfall erosivity factor, R, which expresses the erosive potential of rainfall.

A Revised Universal Soil Loss Equation (RUSLE) was proposed by *Renard et al.* [1997]. The model still follows equation 1.25, but the methods of calculation and the data used for some of the parameters were updated. Of note to this investigation are the changes made to the erosivity parameter in the new version of the model, and these are explained in detail below.

Rainfall erosivity

In the (R)USLE, erosivity is defined for a storm as the product of storm total kinetic energy, E (Jm^{-2}), and the maximum 30-minute precipitation intensity that occurs during the storm, I_{30} (mmhr^{-1}), and is then summed over all storms, s, within the period of interest (a year or several years):

$$R_{R,U} = \sum_{s} EI_{30} \tag{1.27}$$

This original definition of erosivity in the (R)USLE is referred to as $R_{R,U}$ to distinguish it from the more recent version below, and is referred to in the text as the EI30 erosivity term. *Wischmeier and Smith* [1958], who proposed this formulation, found that it explained between 72 and 85% of yearly variations in soil loss from six different soils under continuous fallow.

Many modifications to the erosivity parameter have been suggested since the development of the USLE and RUSLE models [*Usón and Ramos*, 2001]. In particular, there is currently no direct account made of surface runoff in the (R)USLE. This has been widely criticised, and several alternative versions of the erosivity term which incorporate runoff have been proposed (e.g. the USLE-M and MUSLE variants, and others discussed in *Kinnell* [2010]). The kinetic energy of precipitation impacting the soil provides the energy needed to detach sediment from the earth, but rainsplash is not in itself an efficient erosive agent. For erosion to occur, runoff is needed to transport the detached soil particles, and this also causes further detachment. With this in mind, *Kinnell et al.* [1994] proposed an alternative formulation for erosivity,

$$R = \sum_{s} \left[\sum_{t} q_t e_t (\triangle t)^2 \right] \tag{1.28}$$

where q_t and e_t are the runoff rate and the rainfall kinetic energy flux at time t, occurring over duration $\triangle t$, during each storm. This is referred to in subsequent

chapters as the QE erosivity term. Note that the units of $R_{R,U}$ are Jmm.m^{-2}hr^{-1} while R is in Jmm.m^{-2}. This does not pose a problem because erosivity is non-dimensionalised by the K factor, which takes units of soil loss per unit of erosivity. Because equation 1.28 was empirically determined, it accounts for detachment by both impact and runoff. Lack of surface runoff data makes the QE erosivity index difficult to implement in the field. This problem is negotiated in chapter 3 by using a climate model with a land surface runoff scheme.

Because the model is empirical, any determinants of soil loss that are not explicitly included as a separate term in the equation are implicitly accounted for via empirical relationships with the other variables in the model. Therefore, if a term for surface runoff were added, the tabulated values of L, S, C, P and K would need to be re-calculated. *Kinnell* [2010] acknowledges this, advocating nonetheless for changes in the model to improve erosion estimations.

Kinetic energy parameterisations

Since the earliest work attempting to quantify the relationship between precipitation and soil erosion, it has been accepted that raindrop impact is a crucial determinant of soil loss [*Rosewell*, 1986]. The mechanical energy required to erode soil is delivered by raindrops in the form of kinetic energy as they fall. Direct measurements of kinetic energy have not been made, and values are instead based upon observations of drop size distribution and drop terminal velocity. For simplicity therefore, energy is parameterised from rainfall intensity.

In the (R)USLE total storm kinetic energy, E, is found using a parameterisation of energy per unit depth of rainfall, E_d, from periods of constant rain intensity within the storm, i. Multiplying E_d by accumulated surface precipitation, P, gives the total energy for each sub-storm period. These sub-storm periods are then summed to calculate the total energy for the storm.

Energy-intensity relationships differ between the USLE and RUSLE; both are empirical fits to historical observations of raindrop velocities and size distributions with intensity. The USLE uses a logarithmic equation proposed by *Wischmeier and Smith* [1958] based on measurements of size distributions and fall speeds of drops by *Laws and Parsons* [1943] and *Laws* [1941]:

$$\begin{aligned} E_d &= 11.87 + 8.73 log_{10}(i) \quad i \leq 76 \text{mmhr}^{-1} \\ E_d &= 28.3 \qquad\qquad\qquad i > 76 \text{mmhr}^{-1} \end{aligned} \tag{1.29}$$

while the RUSLE takes an exponential form [*Brown and Foster*, 1987]:

$$E_d = 29[1 - 0.72e^{-0.05i}] \tag{1.30}$$

E_d is in $\text{Jm}^{-2}\text{mm}^{-1}$ and intensity, i, is in mmhr^{-1}. Fig. 1.7 shows a comparison between these energy-intensity parameterisations. The RUSLE predicts lower energy per unit depth of rain than the USLE for rains less than $35\,\text{mmhr}^{-1}$ and greater energy for higher intensity rainfall. The two forms differ considerably at low intensities. Equation 1.29 has an implicit minimum intensity threshold of $0.04\,\text{mmhr}^{-1}$, below which it would predict negative energies; the USLE therefore discounts all energy from rainfall below this level. By contrast, the RUSLE version unphysically predicts a minimum energy of $8.12\text{Jm}^{-2}\,\text{mm}^{-1}$ at zero rain intensity [*Van Dijk et al.*, 2002]. Despite this, equation 1.30 is favoured in RUSLE guidelines because it is based upon a larger dataset and continuously approaches an asymptote at high intensities, as reflected in observations, while equation 1.29 must be coerced to a maximum at $76\,\text{mmhr}^{-1}$.

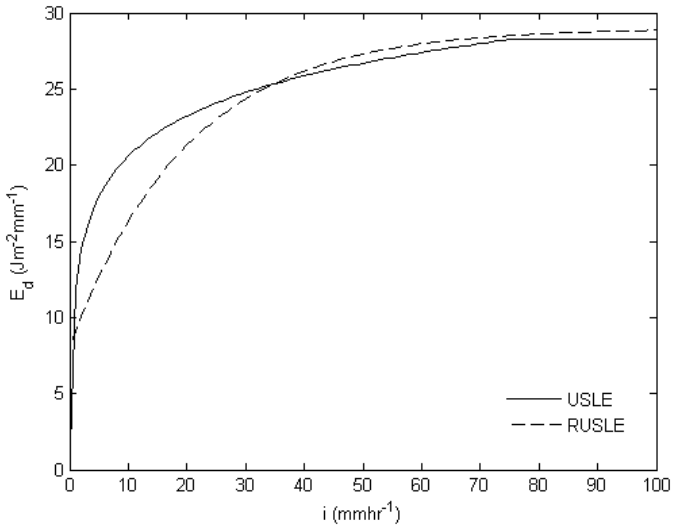

Figure 1.7: Comparison between kinetic energy-intensity parameterisations used in the USLE (solid line, equation 1.29) and RUSLE (dashed line, equation 1.30).

Rainfall kinetic energy flux, e ($\text{Jm}^{-2}\text{hr}^{-1}$), can be calculated from E_d by multiplying

by rain intensity:

$$e = iE_d \tag{1.31}$$

The result is an approximately linear relation between rainfall intensity and kinetic energy flux at higher intensities (*Salles et al.* [2002], chapter 4).

Several alternative energy-intensity parameterisations have been put forward (*Salles et al.* [2002], *Van Dijk et al.* [2002] and *Usón and Ramos* [2001] provide reviews). Many of these are developed for use in regions outside the United States, though the original USLE and RUSLE equations remain widely used in many regions [*Van Dijk et al.*, 2002].

In earlier work (e.g. *Wischmeier and Smith* [1958]), observations of drop size distributions underpinning the kinetic energy calculations were made using simple techniques such as flour trays. More recently, raindrop sizes have been measured using disdrometers, which may be optical or electromechanical. The Joss-Waldvogel disdrometer is an electromechanical impact disdrometer commonly used in the derivation of kinetic energy-intensity parameterisations for erosion studies [*Joss and Waldvogel*, 1967; *Illingworth and Stevens*, 1987]. The device processes the impact of raindrops electronically, producing an output signal which varies as D^n where D is the drop diameter and n is in the range 3.1 to 4.3 [*Illingworth and Stevens*, 1987]. The fall speed of the drops as a function of diameter is then needed to compute concentrations, and this is assumed to follow the measurements taken by *Gunn and Kinzer* [1949]. *Kinnell* [1976] raised concerns about large errors due to deviations of drops from terminal fall speed in windy conditions, but subsequent work indicated that these errors were only about 4% [*Joss and Waldvogel*, 1977]. For erosion studies, errors relating to soil properties and conditions (factors L, S, C, P in the (R)USLE) and measuring actual soil loss for calculation of the K factor, are likely to be far greater than this.

Storm classification

The form of the EI30 erosivity parameter requires an event-based treatment of erosion, as the peak 30-minute intensity for each event must be determined in order to calculate the erosivity (equation 1.27). Storms are defined in the guidelines for both the USLE and RUSLE as follows: rains of 0.5 inches or less over a period of 6 hours

are excluded and these periods are treated as breaks between storms [*Wischmeier and Smith*, 1978; *Renard et al.*, 1997]. This assumes that these low intensity rains are of negligible importance to the total erosion [*Wischmeier and Smith*, 1978]. This assumption is tested in chapter 3.

Alternative erosion models

There are also many process based erosion models (e.g. WEPP [*Flanagan et al.*, 2001]), which have not been used in this study for several reasons. These are often preferred because they include more detail on the physical processes occurring in the soil than the (R)USLE. However, they also require more data to constrain them, which are not available in many regions [*Kinnell*, 2010; *Bagarello et al.*, 2010]. The simplicity of the (R)USLE equation is its strength, as it can be used in a wider range of situations than more sophisticated process models. In regions with limited data, this enables (albeit very simple) studies of the influence of rainfall on erosion, without considering the intricate soil processes involved. In addition, the application of process based models is usually limited to the field or catchment scale because of computational expense, and they are often not suitable for climatological time frames. For these reasons, the (R)USLE model continues to be widely used (in over 100 countries [*USDA*, 2013]).

1.3.3 Climate models and soil erosion

Soil erosion is likely to be affected by climate change via two broad pathways: factors which influence the land surface, and those which change the climate drivers of erosion, namely wind and rain. The first of these encompasses a number of possible influences, including plant biomass production, decomposition rates, soil microbial activity, evapotranspiration and changes in human land use. These effects are difficult to quantify, but *Nearing* [2001] suggests that changes in rainfall erosivity are likely to dominate.

Erosion models require climate data at high temporal and spatial resolutions. The potential of data from global climate models (general circulation models, GCMs) to be used as input for ecological models has been recognized by many authors. There are two main obstacles to this approach: spatial and temporal downscaling from the

coarse GCM projections. Previous studies have used statistical methods to combat these issues.

For temporal disaggregation, *Renard and Freimund* [1994] developed empirical relations between erosivity and annual rainfall data in the United States. Their work built upon several other studies which had done the same elsewhere in the world. *Nearing* [2001] calculated erosivity values from GCM projections over the United States using this method, but made no attempt to obtain information at higher spatial resolutions. An alternative approach has been to use stochastic weather generators to produce rainfall data at the frequencies needed for hydrological impact models. CLIGEN [*Nicks and Gander*, 1994] was developed specifically to generate input data for WEPP, and was later used to calculate RUSLE erosivity indices [*Yu*, 2002]. An alternative method to using GCM projections has been to run CLIGEN on historical climate observations and perturb these data to reflect plausible future outcomes [*Pruski and Nearing*, 2002b].

To obtain local information from model data at low spatial resolutions, *Zhang* [2005], *Zhang* [2007] and *Zhang et al.* [2010] fitted transfer functions between GCM output for the 20$^{\text{th}}$ century and local observations and then applied the same function to future model projections. High frequency data was then obtained from the monthly model output using CLIGEN and used to generate erosivity indices and force erosion models. Studies often employ the 'change factor' method, applying relative shifts in climate parameters obtained from climate model output directly to local baseline time series to infer likely local changes without attempting to account for differences in climate variability across spatial scales [*Pruski and Nearing*, 2002a; *Hansen and Ines*, 2005; *Favis-Mortlock and Guerra*, 1999].

Wood et al. [2004] discussed methods for downscaling both GCM and low resolution regional climate model (RCM) data for input to a range of hydrological models, but this has not been done for erosion models. Further spatial downscaling of RCM data would be required to provide site-specific data, but RCMs run at high resolutions could be used to conduct erosion studies on regional or catchment scales. Given sufficient computing resources, RCMs can be tailored to specific needs, delivering output at sub-daily frequencies over limited areas and time periods.

Current erosion models include considerable detail on soil processes but employ simplified treatments of rainfall. This research explores an alternative approach, using a RCM to simulate rainfall erosivity. This approach permits simplistic soil

erosion studies from an atmospheric science perspective. Using a climate model in this way enables dynamic investigations into the role of weather and climate in soil erosion, and how this may alter in a changing climate and on spatial scales where it is not practical to obtain data to parameterise erosion models.

1.4 Thesis outline

This thesis explores the potential of a RCM to be used for erosion studies by simulating rainfall erosivity. Chapter 2 provides an overview of dynamic models of the atmosphere, including the Weather Research and Forecasting (WRF) model used for this research. In particular, the treatment of cloud microphysics in the WRF model is described, as this is the basis for the work presented in chapters 4 and 5. Chapter 3 tests the common assumption that erosion is caused entirely by heavy storm rain, using a one year WRF model simulation of rainfall erosivity in the Caucasus region as a case study. Chapter 4 presents the first dynamic simulation of rainfall kinetic energy flux, an important quantity in erosion modelling, using a cloud-resolving version of WRF. The influence of aerosols on rainfall erosivity is explored in chapter 5. A stationary supercell storm with heavy precipitation and a gentle orographic rain event provide the two idealised case studies used to illustrate that aerosols may have an effect on rainfall erosivity and therefore on soil erosion.

2 Dynamic models of the atmosphere

2.1 Concepts

Parameterisation

The climate on a global scale is represented by general circulation models. The spatial resolution of these models is typically on the order of 100 to 300 km but continues to increase with computational power [*Salathe Jr et al.*, 2010]. Processes occuring at sub-grid scales contribute sources and sinks of momentum and energy, but cannot be explicitly resolved [*Hartmann*, 1994]. These features must be parameterised: the effect of these processes on those that are resolved is specified based on the resolved fields. These parameterisations are a major cause of divergence between models and a chief concern when considering model deficiencies [*Von Storch*, 2006].

Regional climate models

Information is often required at higher resolution than provided by GCMs, for example when climate or meteorological data is needed for a specific site, or when the topography of a region (which may not be well resolved) is likely to significantly affect the local climate and weather patterns. This is either achieved by statistical downscaling, which does not account for the influence of local terrain on weather systems [*Salathe Jr et al.*, 2010] and assumes that the relationship between large and small scale behaviour is invariant [*Huntingford et al.*, 2003], or with the use of a regional climate model [*Von Storch*, 2006]. RCMs operate on a limited area, and are forced at the boundaries of their domain by data that describes the large scale dynamics, provided by a GCM or reanalysis data. Reanalyses are best estimates of

the state of the atmosphere at a given time, produced by a global model of the atmosphere and/or ocean constrained by observations [*Von Storch*, 2006]. Depending on their resolution, which may range from metres to tens of kilometres [*Leung et al.*, 2006; *Zhang et al.*, 2009], regional models are able to resolve features of the local terrain in more detail, and therefore better represent those mesoscale processes that are affected by these features (e.g. orographic precipitation). Usually, local features represented by regional models are not fed back onto the larger scale, so their effect on the wider meteorological conditions is not captured [*Salathe Jr et al.*, 2010]. It is important to note that regional model simulations, when forced by data from a GCM at the boundaries, will inherently reflect biases from both models. Forcing using reanalysis data, or performing several simulations using a range of GCMs, can help to isolate deficiencies in the regional model [*Salathe Jr et al.*, 2010; *Von Storch*, 2006]. The drawback of regional models lies in this inability to explicitly resolve biases, and in the computational power they necessitate.

2.2 Theory

The same primitive equations underpin all models of atmospheric physics. These are the Euler equations, which correspond to the full Navier-Stokes equation for fluid flow with zero viscosity and heat conduction terms, plus conservation of mass and energy. The Navier-Stokes equation describes the flow of a moving viscous fluid. It is derived by application of Newton's Second Law to a moving parcel of fluid, whereby the acceleration of a body is equal to the sum of all the forces acting upon it. This is the law of conservation of momentum.

$$\frac{D\mathbf{u}}{Dt} = -\frac{1}{\rho}\nabla p - [2\mathbf{\Omega} \times \mathbf{u} - \Omega \times (\mathbf{\Omega} \times \mathbf{r})] - g\mathbf{k} - \frac{\mu}{\rho}\nabla^2\mathbf{u} \tag{2.1}$$

In equation 2.1, the operator $\frac{D}{Dt} = \frac{\partial}{\partial t} + \mathbf{u}.\nabla$ is the material derivative, which describes the rate of change with time following the motion of the parcel. ρ is the air density, p is the pressure, μ is the dynamic viscosity, Ω is the angular velocity of the Earth, $\mathbf{u}$ is the velocity vector (measured in the rotating frame), $\mathbf{r}$ is the radial distance from the Earth's centre, g is the gravitational acceleration, and $\mathbf{k}$ is the unit vertical vector. $\frac{D\mathbf{u}}{Dt}$ is the acceleration and the terms on the right hand side of equation 2.1 represent the forces acting on a parcel of fluid. These are, from left to right, forces

arising from pressure differences, the Earth's rotation, gravity and viscosity. This can be expanded to give three equations, one for each of the three components of the acceleration vector. Solving equation 2.1 requires additional assumptions because the five unknown quantities (three components of $\mathbf{u}$, ρ and p) require five prognostic equations. The Navier-Stokes equations can be simplified for a non-viscous fluid as follows:

$$\frac{Du}{Dt} = -\frac{1}{\rho}\frac{\partial p}{\partial x} + F_x \tag{2.2}$$

$$\frac{Dv}{Dt} = -\frac{1}{\rho}\frac{\partial p}{\partial y} + F_y \tag{2.3}$$

$$\frac{Dw}{Dt} = -\frac{1}{\rho}\frac{\partial p}{\partial z} - g + F_z \tag{2.4}$$

where $\mathbf{u}$=(u,v,w) and F_x, F_y, F_z are the non-pressure forces including rotational and turbulent mixing, as well as forces arising from model physics such as sub-grid parameterisations. Conservation of mass (the continuity equation 2.5) and energy (the First Law of Thermodynamics, equation 2.6) are also required:

$$\frac{D\rho}{Dt} + \rho\nabla.\mathbf{u} = 0 \tag{2.5}$$

$$\frac{D\theta}{Dt} = \frac{Q}{c_p}\left(\frac{p}{p_0}\right)^{-R/c_p} \tag{2.6}$$

where p_0 is the surface pressure, R is the universal gas constant, c_p is the specific heat capacity at constant pressure, θ is the potential temperature and Q are heat sources and sinks.

These equations can be written in a variety of forms to account for the intended application, such as for solutions on different map projections or to make approximations for incompressibility or hydrostatic balance. In particular, they are usually adjusted to include water vapour, an essential component of the climate system. Where water vapour is included, an equation for conservation of each of these water species is needed:

$$\frac{Dq_m}{Dt} = S_{q_m} \tag{2.7}$$

where q_m is the mass of each water species m =vapour, cloud, rain etc. and S_{q_m} represents the sinks and sources of each species.

Finally, an equation of state is adopted to relate density changes to variations in pressure and temperature. It is assumed that the atmosphere behaves as an ideal gas, such that

$$p = \rho R^* T \tag{2.8}$$

where R^* is the specific gas constant (R per unit mass). This provides six equations and six unknown quantities u, v, w, ρ, p and T, plus a prognostic equation for each water species [*Andrews*, 2010; *Cushman-Roisin*, 1994; *Hartmann*, 1994; *Laprise*, 1992]. These may be solved given boundary conditions, which are discussed further below.

2.3 The Weather Research and Forecasting Model

The Weather Research and Forecasting model (WRF, *Skamarock et al.* [2008]) is a mesoscale numerical weather prediction (NWP) model designed for flexible use across a range of physical scales. It was developed and is supported for both research and operational applications, and is intended to assist connections between these two areas. WRF is an open source community model and can be run on a range of computing platforms. Applications inlude real time forecasting, regional climate modelling, physics research, ocean-atmosphere coupling, data assimilation and idealised simulations [*Skamarock et al.*, 2008]. It contains a range of physics options and paramaterisation schemes and its flexibility to be run both as a regional climate model and as a simple idealised cloud resolving model lends itself well to the research conducted for this thesis.

The model uses a terrain-following sigma vertical coordinate system, commonly employed in other models, which permits simulations over complex orography as demonstrated in chapter 3. The model top is maintained at constant pressure, with options to user-define the vertical levels and minimum pressure. It is run on a Arakawa-C grid staggering, in which the horizontal wind velocity components are

positioned in the centre of the cell edges, while all other variables (mass, thermodynamic, scalars etc.) are in the centre of the cell [*Skamarock et al.*, 2008].

WRF solves the fully compressible, non-hydrostatic Euler equations in flux form, including moisture. These equations (equations 2.2 to 2.7) are recast in terms of a base state atmosphere in dry hydrostatic balance plus a perturbation term to avoid truncation and numerical errors in horizontal and vertical pressure gradients. They are also reformulated for solutions on a range of map projections and for the sigma vertical coordinate system. The core prognostic variables are the u, v and w components of the wind velocity, perturbation geopotential, perturbation potential temperature and perturbation surface pressure of dry air. In addition, scalars such as mixing ratios and number concentrations of water vapour, rain/cloud water and ice species and chemical tracers are also prognosed depending on the physics options employed.

The model is advanced in time using a Runge-Kutta time integration procedure (RK3), in which the lower frequency modes, which are also the most meteorologically relevant, are integrated every model time step, while higher frequency 'acoustic' modes are advanced at sub-time step intervals. This maintains model stability at minimum computational cost. The acoustic time stepping contributes the major portion of the computational cost, but much of the most expensive model physics is performed in the longer time step or external to the RK3 procedure using additive time splitting. Savings are made by using a time step that is large compared with the acoustic time step [*Skamarock et al.*, 2008].

WRF is a limited area model, run over a prescribed domain. Boundary conditions provide a constraint on the regional model, ensuring that the simulation within the domain is consistent with the wider meteorology. The lateral boundary conditions are specified for real data cases using a relaxation boundary condition, whereby the outermost grid box corresponds exactly to the input data while in the relaxation zone (typically the four grid boxes next to the specified layer) the model fields are relaxed towards the specified boundary conditions. WRF can also optionally be forced with sea surface temperatures throughout the simulation. These may be data from reanalyses, GCMs or observations processed using the WRF Preprocessing System (WPS). In addition to the lateral boundary forcings, WRF must be intialised over the domain at the start of a simulation. The fields required for this are three-dimensional (3D) temperature, pressure, u and v components of horizontal wind,

relative humidity and geopotential height fields. Two-dimensional (2D) surface pressure, temperature, relative humidity and u and v fields, and sea level pressure are also needed. The model uses 2D soil temperature and moisture, and static 2D data for terrain elevation, land use, soil texture categories and a land-sea mask, as well as information about the map projection, Coriolis and latitude/longitude points in the domain [*Skamarock et al.*, 2008].

Nesting of domains can be used to obtain higher horizontal resolution over a portion of the outer domain. Boundary conditions for the fine resolution domain(s) are calculated by interpolating the coarse grid simulation fields. To retain model stability, the resolution must be gradually increased from the coarsest data used to force the outer domain to the innermost domain with high resolution. When very high resolution is required this is achieved using multiple nests.

Several idealised test cases are provided with the standard WRF model release. These can be 1D, 2D or 3D and the default physics simulated is drastically simplified. In most cases radiation physics is excluded and there are no surface fluxes (no heat or moisture fluxes) or frictional effects. Unlike in real data simulations, boundary conditions are not specified and may be open, periodic or symmetric. The model is initialised using a reference atmospheric state which is computed from a 1D sounding of potential temperature, water vapour mixing ratio and the two components of the horizontal wind velocity at specified heights above the ground, as well as surface values for pressure, potential temperature and water vapour mixing ratio. The reference state (dry hydrostatic balance) and perturbation terms needed to initialise the model are computed assuming that these data represent an atmosphere in moist hydrostatic balance. The input sounding is contained in a simple text file which is easily modified by the user. This simplified version of the model provides a valuable testing ground for atmospheric dynamics and cloud physics.

2.3.1 Physics options within WRF

WRF contains several physics options, which fall into the following categories: microphysics, cumulus parameterisation, planetary boundary layer (PBL), land surface, radiation and diffusion. The physics packages compute changes in the tendencies of wind, potential temperature and moisture fields arising because of unresolved sub-grid scale processes. These represent sources and sinks of energy in the Euler equations which are not captured at the grid resolution.

The physics packages are executed in the following order: radiation, surface, PBL, cumulus and finally microphysics. All except the microphysics are integrated within the first RK3 time loop (ie. over the full model time step rather than the smaller acoustic step). Microphysics is the last operation before the time step is advanced, and is executed after the normal RK3 steps as an adjustment prcoess. This is done to ensure that the saturation balance matches the final temperature and moisture for the next time step. In addition, the microphysics scheme provides a latent heat forcing for the calculation of potential temperature by the dynamics solver. The model diffusion parameterises horizontal and vertical turbulent mixing. Diffusion is separated from the other physics options in the model, and is executed by the dynamics solver.

Surface rainfall is computed by both the microphysics and cumulus parameterisations. The total precipitation produced by the model is the sum of the sub-grid (cumulus) and resolved (microphysics) precipitation fields. Microphysics provides updates for moisture and temperature tendencies from resolved grid scale water vapour, cloud and precipitation processes. More information about microphysics schemes is provided in sec. 2.4. A cumulus parameterisation is used to capture the effects of sub-grid scale updrafts and downdrafts on vertical profiles of heat and moisture and on surface rainfall. Precipitation produced by this scheme is calculated independently from the microphysics precipitation. A cumulus parameterisation is not needed at resolutions below about 5 km as at this scale the model is able to resolve the convective fluxes explicitly. Above about 10 km the unresolved convection may be substantial and without a cumulus parameterisation latent heating and precipitation fields may be severely affected. Scales between 5 and 10 km are more difficult, as in this region some, but not all, convective eddies may be resolved. Neither the microphysics nor the cumulus parameterisations use a cloud fraction scheme.

The purpose of the surface layer physics is to feed data into the land surface scheme for the calculation of surface heat and moisture fluxes, and to provide friction velocities for the calculation of surface stress by the PBL package. Over water, fluxes are computed within the surface layer scheme. The land surface scheme computes heat and moisture fluxes over land and sea-ice grids. This is done using information provided by the surface layer and radiation schemes, and total precipitation from the cumulus and microphysics schemes. The complexities of the schemes vary, for example in their treatment of vegetation and canopy effects, surface runoff and

number of soil layers. Land state variables (e.g. soil moisture and temperature) are also updated. The PBL scheme provides tendencies of temperature, moisture and momentum due to sub-grid vertical flux transport from unresolved eddies. It does this throughout the column, in the well mixed boundary layer but also in the stable layer above, using fluxes from the surface layer and land surface schemes. Finally, the radiation scheme calculates atmospheric heating from short and longwave radiative processes. Cloud fraction is considered within the radiation scheme, but is not included in the calculation of precipitation by the cumulus and microphysics parameterisations.

The model is conservative for scalars (e.g. mass of cloud species, equation 2.7), but the advection procedure does not guarantee 'positive definiteness', meaning that negative values are permitted, and are offset by adding positive values. Several physics packages do not allow negative values and will set them to zero, resulting in a net mass increase. A positive definite correction option is available to avoid this problem [*Skamarock et al.*, 2008].

2.4 Microphysics parameterisation schemes

Microphysics parameterisation schemes predict changes in moisture and precipitation fields in models of the atmosphere. They also compute local temperature tendencies from latent heating occurring during phase transitions in the cloud and feed this information back to the model.

Microphysics paramaterisations can be separated into two categories: bin and bulk schemes. In the more comprehensive bin approach the size distribution of each hydrometeor is explicitly computed in the model, based on several tens of bins for each hydrometeor type (cloud, rain, ice, snow etc.). This entails storing variables for each bin and hydrometeor throughout the model integration and is prohibitively costly for most mesoscale modelling applications [*Cohard and Pinty*, 2000]. In the simpler bulk parameterisation models, a functional form for the size distribution of each hydrometeor is assumed, and only integral parameters of this distribution are computed during the model simulation (e.g. *Thompson et al.* [2004]; *Morrison et al.* [2009]; *Lim and Hong* [2010]; *Milbrandt and Yau* [2005]; *Cohard and Pinty* [2000]; *Ferrier* [1994]). The bulk approach saves significantly on computational costs [*Cohard and Pinty*, 2000; *Khain et al.*, 2000], but carries other disadvantages

relating to the accurate representation of the many complex physical processes it attempts to capture. All the microphysics schemes considered in this thesis are of the bulk variety.

2.4.1 Bulk parameterisation equations

Most schemes use the three parameter PSD in equation 1.22, restated here for reference:

$$N(D) = N_0 D^{\mu} \exp(-\lambda D) \tag{2.9}$$

With a shape parameter, μ, of zero, equation 2.9 reduces to an exponential distribution. The n^{th} integral moment of the PSD is then

$$m(n) = \int_0^{\infty} D^n N(D) dD \tag{2.10}$$

The error incurred by integrating over the limits [0,∞] rather than over the realistic range of drop sizes is small and is routinely neglected [*Srivastava*, 1967; *Willis*, 1984].

Most schemes are either single or double moment in each hydrometeor class, meaning that they prognose either one or two integral moments of the PSD. The two moments most commonly predicted are the zeroth and the third, as these have physically useful interpretations. The zeroth moment is the total number concentration, and the third is proportional to the mass content assuming particles are spherical. The double moment approach predicts both of these, while single moment schemes predict only mass [*Milbrandt and Yau*, 2005]. Computing the third moment allows the rainfall rate to be found from the mass content according to

$$i \propto \int_0^{\infty} D^3 N(D) V(D) dD \tag{2.11}$$

Three equations are required to fit all three parameters of equation 2.9. In the double moment case, there are two equations and the shape parameter, μ is usually held constant or diagnosed from known model variables. N_0 and slope parameter, λ, can be computed from the predicted number concentration, N_T, and mass mixing ratio, Q:

$$N_0 = N_T \frac{\lambda^{\mu+1}}{\Gamma(\mu+1)} \tag{2.12}$$

$$\lambda = \left[\frac{cN_T\Gamma(1+\mu+d)}{\rho Q \Gamma(1+\mu)} \right]^{1/d} \tag{2.13}$$

where Γ is the gamma function[1], ρ is the air density and c and d are the constants in the mass relation (equation 1.23).

With only one prognostic equation, single moment schemes either fix or diagnose N_0. N_T and λ can then be found by rearranging the terms in equations 2.12 and 2.13. It is a challenge of any parameterisation scheme to represent different regimes using the same set of equations. Observations indicate that N_0 can vary dramatically in time and between regions [*Waldvogel*, 1974]. Incorporating a variable intercept into a *Marshall and Palmer* [1948] PSD can better account for a range of scenarios with different particle sizes and is computationally cheaper than adding number concentration as an extra prognostic variable [*Thompson et al.*, 2004, 2008; *Abel and Boutle*, 2012]. Relating N_0 to mass is a common approach [*Abel and Boutle*, 2012; *Reisner et al.*, 1998; *Thompson et al.*, 2008, 2004], but for the snow PSD temperature is sometimes used [*Thompson et al.*, 2004]. Moreover, the microphysical structure of different storm types (e.g. convective and stratiform rain) can be very different, and allowing the PSD parameters to vary independently is the most realistic way to represent these variations.

A terminal velocity-diameter relation, $V(D)$, is also adopted. In many schemes this can be expressed in the general form:

$$V(D) = \sqrt{\frac{\rho_0}{\rho}} a D^b \exp(-fD) \tag{2.14}$$

where a, b and f are empirically determined constants. This is based on measurements at sea level (e.g. *Gunn and Kinzer* [1949]; *Laws* [1941]), so the scaling factor $\sqrt{\frac{\rho_0}{\rho}}$, where ρ_0 is the surface air density, is included to account for the reduction with height in the drag force felt by falling particles as air becomes less dense [*Ferrier*, 1994]. Number and mass do not sediment at the same rate. The moment-weighted terminal velocity is used for each, so that number concentration sediments at the

[1] $\Gamma(n) = \int_0^\infty x^{n-1} e^{-x} dx = (n-1)!$[*Boas*, 1983]

number weighted fall speed, $[V]_{N_T}$, and mass at the mass-weighted speed, $[V]_Q$ [*Milbrandt and Yau*, 2005]:

$$[V]_Q = \frac{\int M(D)N(D)V(D)dD}{\int M(D)N(D)dD} \tag{2.15}$$

$$[V]_{N_T} = \frac{\int N(D)V(D)dD}{\int N(D)dD} \tag{2.16}$$

where $M(D)$ is the particle mass (equation 1.23).

Large particles, falling faster than smaller ones, appear preferentially at lower levels in the atmosphere. The different sedimentation rates of mass and number concentration in double moment schemes allow this natural size sorting effect to be represented to some extent in the model. As $[V]_Q$ is always greater than $[V]_{N_T}$, the ratio Q/N_T is higher in the lower model levels. The mean-mass diameter, $D_m = \left[\frac{\rho Q}{cN_T}\right]^{1/d}$, therefore also increases towards the ground [*Milbrandt and Yau*, 2005]. This effect cannot be represented in a single moment scheme because, in this case, N_T varies monotonically with Q. This is unrealistic, as some microphysical processes clearly show that these quantities can vary independently in nature. For example, diffusional growth increases Q but does not change N_T, while the opposite is true for the breakup of large unstable raindrops. Single moment schemes which incorporate a variable intercept N_0 (e.g. *Thompson et al.* [2004], *Abel and Boutle* [2012]) go some way towards rectifying this problem, but this requires an appropriate diagnostic relation which may not be appropriate for all situations and model setups.

The shape parameter, μ, however, is not permitted to vary independently, as this would require a third prognostic equation. *Milbrandt and Yau* [2005] showed that the shape parameter is important for acheiving the correct degree of vertical size sorting in the column. Excessive size sorting can occur with double moment schemes after longer time periods because the relative sedimentation velocity of mass compared with number concentration, $^{[V]_Q}/_{[V]_{N_T}}$ is allowed to diverge without limit [*Shipway and Hill*, 2012; *Milbrandt and Yau*, 2005]. In a fully prognostic situation, μ increases with the degree of size sorting, effectively constraining this to within physically realistic bounds. While three moment schemes remain unfeasible computationally, *Milbrandt and Yau* [2005] also found that higher values of μ are preferable, with an exponential PSD (μ=0) performing least well.

The treatment of sedimentation in microphysics schemes is important for the research presented in this thesis, which relies on the representation of the size of raindrops arriving at the ground. Errors introduced by this problem can be particularly large for higher order moments [*Milbrandt and McTaggart-Cowan*, 2010], and so are important for the surface level rainfall kinetic energy flux calculations presented in chapter 4.

The shape parameter is also important for precipitation development because of its effect on particle interactions. A narrower spectrum will inhibit collisions. This can reduce raindrop formation and freezing of cloud droplets [*Morrison et al.*, 2005], and inhibit the formation of large raindrops. It could also impact other collision dependent microphysical processes such as riming.

2.4.2 Microphysical continuity equations

Kessler [1969] proposed the earliest parameterisation model of precipitation, and described the basic mass continuity equation that underpins modern microphysics schemes. These equations have since been extended to include prognostic equations for the number concentrations of hydrometeors. They may be generalised in the following way, where N_{Tx} is the number concentration and Q_x is the mass mixing ratio of each hydrometeor, x [*Ferrier*, 1994]:

$$\frac{\partial N_{Tx}}{\partial t} = -\nabla.(\mathbf{V}N_{Tx}) + TURB(N_{Tx}) + \frac{\partial}{\partial z}(N_x[V_x]_{N_T}) + \frac{dN_{Tx}}{dt} \tag{2.17}$$

$$\frac{\partial Q_x}{\partial t} = -\frac{1}{\rho}\nabla.(\rho\mathbf{V}Q_x) + TURB(Q_x) + \frac{1}{\rho}\frac{\partial}{\partial z}(\rho Q_x[V_x]_Q) + \frac{dQ_x}{dt} \tag{2.18}$$

Here ρ is the air density and $\mathbf{V}$ is the 3D velocity vector. The terms on the right hand side of 2.17 and 2.18 represent, from left to right, changes in N_{Tx} and Q_x by advection, turbulent diffusion, vertical flux convergence (sedimentation) and microphysical sources and sinks.

The last term encapsulates the local changes in mass/number by microphysical processes described in sec. 1.2 (nucleation, condensation, evaporation, coalescence, accretion, breakup, riming, aggregation etc.) and by others which have not been described in detail such as the melting of ice particles into raindrops as they pass through the melting layer. *Ferrier* [1994] showed that it was more important to

preserve the spectral characteristics of interacting hydrometeors (i.e. the slope and intercept parameters of the PSDs) than their number concentration, particularly for higher order moments such as radar reflectivity (proportional to D^6). This is because of errors arising from the fixed PSD shape parameter. The precise source/sink terms vary between schemes, depending on which hydrometeor classes are included and the level of complexity of the model (Fig. 2.1). The number of processes that must be described increases as more hydrometeors are added; for a warm rain scheme, there are fewer potential interactions between species than in a scheme which also includes several ice phases.

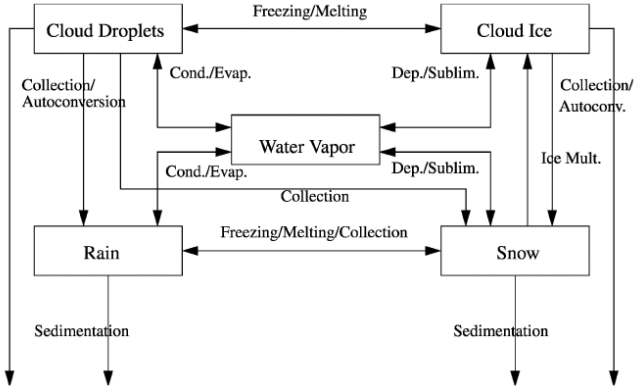

Figure 2.1: Schematic showing the main processes captured by a microphysics parameterisation scheme, taken from *Morrison et al.* [2005]. This example does not include hail or graupel.

2.4.3 Treatment of supersaturation

Very high resolutions are needed to fully resolve the supersaturation field. This is needed in order to model droplet activation using the full Köhler relation (equation 1.6), for which the maximum supersaturation is needed. For lower resolutions, activation is computed based on the maximum vertical velocity (which itself may be resolved or parameterised) according to equation 1.8. In many schemes, droplet activation is not modelled at all, and cloud droplet number concentration is maintained at a fixed value.

Prognostic supersaturation is also needed to model the rate of diffusion (for condensation/evaporation/deposition/sublimation). To circumvent this problem, a saturation adjustment method is usually employed, whereby any excess vapour (relative

humidity greater than one) is instantly condensed. Droplet growth using this method does not depend on drop size according to equation 1.14. The instantaneous saturation approximation is reasonable for liquid water, for which the timescale of kinetic effects is short so that supersaturation is usually relatively low. This is not true for ice, where phase relaxation timescales are longer and large supersaturations are frequently observed. Deposition/sublimation of ice may therefore be modelled using non-equilibrium vapour diffusion.

2.4.4 WRF microphysics schemes

Four microphysics parameterisation schemes are used during the model simulations in this thesis: Thompson [*Thompson et al.*, 2008], Morrison [*Morrison et al.*, 2009], Milbrandt-Yau [*Milbrandt and Yau*, 2005] and WDM6 [*Lim and Hong*, 2010]. An updated version of the Morrison scheme used in chapter 5 is described later in this section. The remaining schemes are the standard versions released with the WRF model.

All four schemes predict mass mixing ratio, Q_x, and (where double moment) number concentration, N_{Tx}, for each hydrometeor, x, according to equation 2.10, and follow the microphysical continuity equations 2.17 and 2.18. Some of the main features of each model are outlined in Tab. 2.1. The Morrison scheme includes a user switch for graupel or hail; graupel is used by default. The default versions of Morrison, Thompson and Milbrandt-Yau all impose a constant cloud droplet number concentation, N_{Tc}. WDM6 and the updated Morrison scheme, however, are double moment in cloud water, predicting the total mass and number of droplets. Unique among the standard WRF microphysics schemes, WDM6 also predicts the number concentration of CCN. Cloud water droplets are the only non-sedimenting particle in all the schemes, except in Morrison where all hydrometeors are given a terminal fall speed.

The size distributions adopted for each class of hydrometeor in the four schemes are summarised in Tab. 2.2. Most can be expressed using the three parameter gamma distribution in equation 2.9. Exceptions to this are snow in the Thompson scheme and cloud ice and water in WDM6. The snow size distribution in Thompson is the sum of an exponential and gamma distribution, which is able to account for the observed "super-exponential" distribution of very small snowflakes, while still accommodating the slope of larger particles [*Thompson et al.*, 2008]. In WDM6, cloud

Microphysics scheme	Mass predicted	Number predicted
Thompson	c, r, i, s, g	r, i,
Morrison	c, r, i, s, g/h	r, i, s, g/h
Milbrandt-Yau	c, r, i, s, g, h	r, i, s, g
WDM6	c, r, i, s, g	c, r, CCN

Table 2.1: Hydrometeor classes included in each microphysics scheme, separated into those for which mass and number are prognosed. c=cloud water, r=rain, i=cloud ice, s=snow, g=graupel, h=hail, CCN=cloud condensation nuclei. Adapted from *Skamarock et al.* [2008].

water follows a generalised gamma distribution, of which equation 2.9 is a particular form with υ=1 (Tab. 2.2). The treatment of cloud ice in WDM6 is different and will be briefly described at the end of this section. In Thompson, the shape parameters for rain, ice and graupel can be easily altered by the user, and in Milbrandt-Yau this can be done for all hydrometeors.

Most particles are assumed to be spherical, with d=3 and $c = \pi\rho_p/6$ in equation 1.23. Snow is an exception: in Thompson $M(D) = 0.069D^2$ and in WDM6 $M(D) = 0.1597D^{2.078}$.

The terminal velocity relation, $V(D)$, adopted for all precipitating hydrometeors in all four microphysics schemes conforms to equation 2.14. Tab. 2.3 gives the values of the constants in this relationship. Morrison, Milbrandt-Yau and WDM6 all adopt a straight power law function (f=0), and only Thompson includes an exponential term. This is an important difference between the schemes, which is explored further in chapter 4. Note that there is no dependence of the sedimentation rate on vertical wind speed. Particles should sediment only when their weight exceeds the upward force arising from updrafts, so drop size should increase with updraft strength. This is achieved indirectly by advection in the double moment schemes. Smaller drops which should be held aloft by a given updraft strength will fall a distance during one time step but be lifted by wind in the subsequent step, while larger drops will fall further in the same time and reach the ground more quickly.

An attempt is made to control excessive size sorting owing to the differential sedimentation velocities of number and mass concentration in Thompson, Morrison and Milbrandt-Yau. WDM6 does not impose any controls on excessive size sorting, with the result that unphysically large raindrops can sometimes appear at ground level. Thompson and Morrison achieve this using similar methods. Thompson imposes a

maximum raindrop median volume diameter (mvd) of 2.5 mm. Morrison does this with a minimum value for the slope parameter λ, applied to all hydrometeors. In the case of rain, this can be understood as forced drop breakup. For other particles this does not hold, but may still be necessary for numerical reasons [*Milbrandt and Yau*, 2005]. In Milbrandt-Yau size sorting is controlled by using a higher value for μ in equation 2.16, so that $[V_x]_{N_T}$ is increased slightly while $[V_x]_Q$ is unchanged, resulting in a decrease in size sorting [*Milbrandt and McTaggart-Cowan*, 2010]. Despite these controls, size sorting can still be too large in these schemes [*Shipway and Hill*, 2012; *Milbrandt and Yau*, 2005].

Updated Morrison scheme with prognostic cloud droplet number

The Morrison scheme has been adapted to include a prognostic treatment of cloud droplet number concentration [*Fan et al.*, 2012; *Morrison et al.*, 2005] (provided by Hugh Morrison via personal communication). In the updated Morrison scheme, droplet activation is based on a power law CCN distribution (equation 1.7). The empirical parameters c (the number of activated CCN with a supersaturation of 1%) and k remain constant during the simulation, so N_{CCN} is not prognostic.

Supersaturation is not resolved by the model, and CCN are activated based on the resolved vertical velocity at the cloud base, w, according to equation 1.8, assuming no initial cloud water is present. Cloud droplets are activated according to the number of activated CCN and existing cloud drops, the sum of which are constrained to equal the background CCN concentrations:

$$[N_{Tc}]_{t+1} = \frac{N_{CCN} - [N_{Tc}]_t}{\triangle t} \tag{2.19}$$

where $[\mathrm{N}_{Tc}]_{t+1}$ and $[\mathrm{N}_{Tc}]_t$ are the number of cloud droplets at times t and $t+1$, respectively and $\triangle t$ is the model time step. All other sources and sinks of CCN are ignored. No distinction is made between aerosols of different size or chemical composition, and no vertical variation in background CCN concentrations is accounted for in the initial conditions. A saturation adjustment method is employed for condensation and evaporation, while deposition and sublimation of ice occur through non-equilibrium vapour diffusion.

WDM6

Treatment of cloud droplet formation and cloud ice in WDM6 differs from the other three schemes. Cloud droplet number prediction in WDM6 is similar to in the updated Morrison scheme, but with some key exceptions. No account is made of the inability of the model to resolve the supersaturation field in WDM6 (as is done using equation 1.8 in the updated Morrison scheme). Instead, CCN activation is computed based on equation 1.7. The coefficient k is fixed, while c is also effectively predefined by choosing the initial CCN concentration, $N_{CCN}|_{t=0}$, and fixing the required maximum supersaturation to activate all CCN, s^k_{max}=0.48%. The total number of activated CCN and cloud droplets are constrained by the background CCN count: $N_{CCN}|_{t=0} = N_{CCN} + N_{Tc}$. Within this constraint, CCN number is altered by evaporation of cloud water and activation of cloud droplets. No other sources or sinks are considered. CCN number is therefore not fully prognostic. At $s = s_{max}$,

$$c = (N_{CCN} + N_{Tc})s^{-k}_{max} \tag{2.20}$$

The number of CCN activated in a given time step, n_a, can then be written according to equation 1.7:

$$n_a = (N_{CCN} + N_{Tc}) \left(\frac{s}{s_{max}} \right)^k \tag{2.21}$$

Cloud ice in WDM6 is handled in a different way from in other schemes. In most schemes, the number concentration of a single moment particle is diagnosed from parameters of the PSD using equation 2.12. In WDM6 however, no PSD is assumed for cloud ice. Instead, the number concentration is diagnosed from the mass mixing ratio:

$$N_{Ti} = 5.38 \times 10^7 (\rho Q_i)^{0.75} \tag{2.22}$$

This equation is based upon an assumption that the fall speed of ice crystals is related to their mass mixing ratio according to the following empirically determined relationship:

$$V_i = 3.29(\rho Q_i)^{0.16} \tag{2.23}$$

Applying this constraint, assuming a mass - diameter relation (equation 1.23) and taking the mean mass of a crystal to be $\rho Q_i/N_i$ results in the terminal velocity - diameter equation given in Tab. 2.3.

	Hydrometeor class	Particle size distribution	Parameters
Thompson	c, r, i, g	$N_D = N_0 D^{\mu} \exp(-\lambda D)$	$\mu_{r,i,g} = 0^*$ $\mu_c = \mu_c(N_{Tc})$ $N_{Tc} = const.*$ $N_{0g} = N_{0g}(Q_g)$
	s	$N(D) = \frac{m(2)^4}{m(3)^2}\left[\kappa_0 \exp\{-\frac{m(2)}{m(3)}\Lambda_0 D\} + \kappa_1 (\frac{m(2)}{m(3)} D)^{\mu_s} \exp\{-\frac{m(2)}{m(3)}\Lambda_1 D\}\right]$	μ_s=0.6357 κ_0=490.6 κ_1=17.46 Λ_0=20.78 Λ_1=3.29
Morrison	c, r, i, s, g	$N_D = N_0 D^{\mu} \exp(-\lambda D)$	$\mu_{r,i,s,g} = 0$ $\mu_c = \mu_c(N_{Tc})$ $N_{Tc} = const.*$
	c		
Milbrandt-Yau	c, r, i, s, g, h	$N_D = N_0 D^{\mu} \exp(-\lambda D)$	$\mu_{r,i,s,g,h} = 0^*$ $\mu_c = 1^*$ $N_{Tc} = const.*$
WDM6	r, s, g	$N_D = N_0 D^{\mu} \exp(-\lambda D)$	$\mu_r = 1$ $\mu_{s,g} = 0$ $N_{0s} = N_{0s}(T)$ $N_{0g} = const.$
	c	$N(D) = N_T \frac{\alpha \lambda^{\alpha\nu}}{\Gamma(\nu)} D^{\alpha\nu - 1} \exp(-(\lambda D)^{\alpha})$	$\alpha = 3$ $\nu = 1$
	i	$N_T = xQ^y$	$x = 5.38 \times 10^7$ $y = 0.75$

Table 2.2: Summary of PSDs for each microphysics scheme. The default values for parameters are given, and * denotes those which can be easily altered by the user. N_{Tc} is the total cloud droplet number and is prescribed in the Thompson and default Morrison and Milbrandt-Yau schemes. For single moment species following a gamma PSD (equation 2.9), N_0 is either fixed (*const.*) or diagnosed as a function of another variable. μ is fixed in most cases, or diagnosed from N_T. $m(n)$ is the n$^{\text{th}}$ moment of the size distribution (equation 2.10).

	Thompson			Morrison			Milbrandt-Yau			WDM6		
	a	b	f	a	b	f	a	b	f	a	b	f
c	-	-	-	3.00 x 10^7	2.00	0	-	-	-	-	-	-
r	4854.00	1.00	195.00	841.90	0.80	0	149.10	0.50	0	841.90	0.80	0
i	1847.50	1.00	0	700.00	1.00	0	71.34	0.66	0	1.49 x 10^4	1.31	0
s	40.00	0.55	100.00	11.72	0.41	0	11.72	0.41	0	11.72	0.41	0
g	442.00	0.89	0	19.30	0.37	0	19.30	0.37	0	330.00	0.80	0
h	-	-	-	-	-	-	206.89	0.64	0	-	-	-

Table 2.3: Constants used in each scheme for the mass - diameter relationship (equation 1.23). Values for cloud ice in WDM6 are derived differently; see the text for an explanation of this. Morrison is the only scheme in which cloud water droplets sediment, so no values are given for other schemes.

3 The contribution of light rain to rainfall erosivity: a case study in the Caucasus region

3.1 Introduction

Low intensity rain is assumed to have a negligible contribution to erosion in the (R)USLE. This is reflected in the minimum intensity threshold of 0.5 in/6 hr ($2\,\mathrm{mmhr}^{-1}$) stipulated in the (R)USLE guidelines [*Wischmeier and Smith*, 1978; *Renard et al.*, 1997]. It is also embedded in the construction of the EI30 erosivity index, which requires an event based treatment, classifying rainfall data into storm periods and excluding rain occurring between storms (sec. 1.3.2). This chapter tests this assumption, using a one year WRF simulation over the Caucasus region to quantify the contribution of light and non-storm rain to rainfall erosivity.

Some studies suggest that low intensity precipitation can cause substantial erosion. In Scotland, a 24-hour rainstorm caused widespread erosion in 1992, though intensities were generally below $4\,\mathrm{mmhr}^{-1}$ [*Kirkbride and Reeves*, 1993]. South of Madrid, lighter rainfall was found to contribute as much as 69% to total erosion from 1994-2005 owing to a high relative occurrence of light compared to extreme events [*Marques et al.*, 2008]. However, lighter rainfall in that study was defined as below $10\,\mathrm{mmhr}^{-1}$, higher than the $2\,\mathrm{mmhr}^{-1}$ (R)USLE threshold. Events of approximately $3.7\,\mathrm{mmhr}^{-1}$ intensity caused 19% of sediment loss during 1997-2006 at another location in Spain [*Baartman et al.*, 2012]. However, these studies only analysed low intensity storms, ignoring precipitation that occurs between events. In general, lack of data is a serious hindrance to a more systematic study. Because of this, a regional climate model can be a useful by enabling a more comprehensive study.

3.1.1 The Caucasus region

3.1.1.1 Geography

The focus region for this chapter is illustrated in Fig. 3.1 and Fig. 3.2. The area consists of eastern Turkey and the area between the Black and Caspian Seas (Georgia, Azerbaijan, Armenia, the southernmost part of the Southern Federal District of Russia, and north-west Iran). This includes the Caucasus Mountains, which run from the north eastern edge of the Black Sea to the west of the Caspian Sea. South of this are the Lesser Caucasus, which are lower in height (highest peak of 4000 m compared with over 5000 m for the Greater Caucasus) and span a larger area. Between these regions a valley runs from north-west to south-east. Turkey is most mountainous in the east and has an average altitude of 1,132 m [*Demirci and Karaburun*, 2011]. These complex and highly varying topographical features necessitate the use of a regional climate model run at sufficient spatial resolution to resolve key features of the landscape. This has been identified as an important requirement for modelling the climate of the region and a problem associated with using coarse resolution GCMs in the area [*Evans*, 2008; *Lelieveld et al.*, 2012; *Evans et al.*, 2004].

Figure 3.1: Map of the broad region of interest for this study [*Google*, 2013]. Country borders and names are shown in yellow. The Caspian Sea is in the east, the Black Sea in the north-west and the eastern part of the Mediterranean Sea can be seen in the south-west of the image.

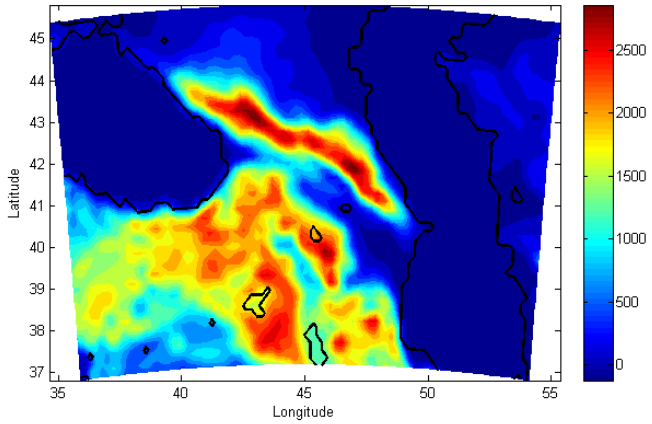

Figure 3.2: Terrain height (m) in eastern Turkey and the Caucasus. The outline of the Caspian sea in the east and the Black Sea in the north-west are also shown. Data is taken from the MODIS data set and interpolated to 20 km resolution.

3.1.1.2 Climate

Climatic conditions in the region are varied, and several types of extreme weather phenomena are observed [*Lelieveld et al.*, 2012]. This is largely attributable to the complex terrain and abrupt changes in altitude [*Mahmudov*, 2003; *Georgian Academy of Sciences*, 2002; *Sensoy*, 2013; *Armenian Travel Bureau*, 2013]. Atlantic storm tracks passing over Eastern Europe are the predominant source of precipitation, with mountainous areas receiving most rain [*Bozkurt et al.*, 2011].

At the higher altitudes of the Greater Caucasus snow cover is year-round. There are about 2000 glaciers in the Caucasus, covering an area of 1600 km^2 [*Shahgedanova et al.*, 2009]. In Georgia, high summer temperatures are experienced in the valley area, while in the mountains conditions tend to be cold and windy in the winter, with storms and heavy precipitation in the summer [*Georgian Academy of Sciences*, 2002]. Neighbouring Armenia and Azerbaijan experience similar extremes, with most precipitation falling as snow in the mountains [*Armenian Travel Bureau*, 2013; *Heydar Aliyev Foundation*, 2013]. Armenia has an average snowfall of 1000 $mmyr^{-1}$ in the mountains [*Armenian Travel Bureau*, 2013]. In Azerbaijan precipitation varies from below 200 $mmyr^{-1}$ in the foothills to 1800 $mmyr^{-1}$ in some of the mountainous areas [*Heydar Aliyev Foundation*, 2013]. In north-west Iran winters are cold with heavy snow in the mountains, while summers are dry and hot. Annual precipitation can be as high as 1,700 mm [*Ministry Of the Islamic Republic of Iran*, 2013]. Turkey has a predominantly Mediterranean climate but its complex terrain leads to

substantial variation around this. The climate in the coastal areas is mild, while the highlands have hot summers and cold winters. Most precipitation falls in the winter [*Sensoy*, 2013].

3.1.1.3 Vulnerabilities

Agriculture is an important sector in the Turkish economy, representing 10% of GDP and providing 25% of employment in 2010 [*European Commission*, 2013]. About 70% of Turkish soils suffer from erosion, with 1 billion tons lost per year from a combination of wind and water erosion [*Demirci and Karaburun*, 2011]. Nearly half the land in Azerbaijan is eroded, with water erosion occurring throughout the country. This poses a serious threat as the agricultural sector sustains 20% of GDP and employs 29% of the working population [*Shelton*, 2003]. In Georgia, the agricultural sector constitutes 28-30% of GDP and between 70 and 100% of soils suffer from erosion [*Kereselidze et al.*, 2013]. It is also an important area for energy, with the BTC pipeline running from Baku, on the coast of the Caspian Sea in Azerbaijan, along the valley via Tbilisi to Ceyhan on the Mediterranean coast of Turkey. The BTC pipeline transports crude oil from oil fields near the Caspian to Europe [*BP*, 2013]. There is concern about the environmental impact caused by the construction of the pipeline, and about the stability of pipelines and above ground installations under high erosion rates.

Climate change projections give further cause for concern. The highlands in eastern Turkey form the headwater region of the Euphrates and Tigris rivers, which provide water to arid Syria, Iran and Iraq further downstream. The rivers are an essential source of water for irrigation and for maintaining public health and political stability in the region [*Cullen and Demenocal*, 2000]. Model simulations suggest a drying of the eastern Mediterranean region under increased greenhouse gases, with a reduction in precipitation predicted by most models by the mid to late 21^{st} century, though the magnitude of the change varies between models [*Giorgi and Lionello*, 2008; *Bozkurt and Sen*, 2013; *Evans*, 2008]. This same trend is expected to extend further east over the Caucasus region and the northern Middle East [*Evans*, 2008]. This is understood to be the result of a poleward shift in the Atlantic storm track owing to greater warming at high latitudes compared with at the equator, leading to a decrease in cyclone density and intensity in the area [*Evans*, 2008; *Giorgi and Lionello*, 2008]. It could lead to a shift in the dominant precipitation process from large scale cyclonic

activity to orographically induced rainfall. This has led to projections indicating that the Euphrates river may have the largest reduction in streamflow of any major river by 2100 [*Nohara et al.*, 2006].

3.2 Methods

3.2.1 Model setup

The domain used for the model simulation is shown in Fig. 3.3. WRF version 3.3 was run from 1st January 2009 for one year over the Caucasus region at a horizontal resolution of 20 km. Data from the Climate Forecast System Reanalysis (CFSR, *Saha and Coauthors* [2006]) at 0.5 degree resolution, produced by the National Centers for Environmental Protection (NCEP), was used for the boundary conditions.

WRF was run at a horizontal resolution of 20 km, with 60 vertical levels between the ground and model top at 5000 Pa. Sub-grid microphysics and convection were parameterised according to *Thompson et al.* [2004] and *Kain* [2004], respectively, and boundary layer physics followed *Janjic* [1994]. Longwave radiation followed *Mlawer et al.* [1997] and shortwave radiation followed *Dudhia* [1989]. Surface runoff was generated by the NOAH land surface scheme [*Chen and Dudhia*, 2001]. In the NOAH scheme, precipitation that is not absorbed by the soil or intercepted by the canopy becomes surface runoff. This occurs when rainfall intensity exceeds the maximum infiltration rate of the soil, or because of soil saturation. There are four soil layers with a fixed water table at a depth of 2 m below the surface and assumptions are made about properties in a given grid point such as hydraulic and diffusive conductivity, canopy resistance and leaf area index [*White and Toumi*, 2012]. Soil, vegetation and land use types are obtained from the MODIS land classifications of the International Geosphere-Biosphere Programme. Model variables were extracted every 30 minutes.

3.2.2 Calculations

The calculation of erosivity, R, follows directly from the QE index proposed by *Kinnell et al.* [1994] (equation 1.28):

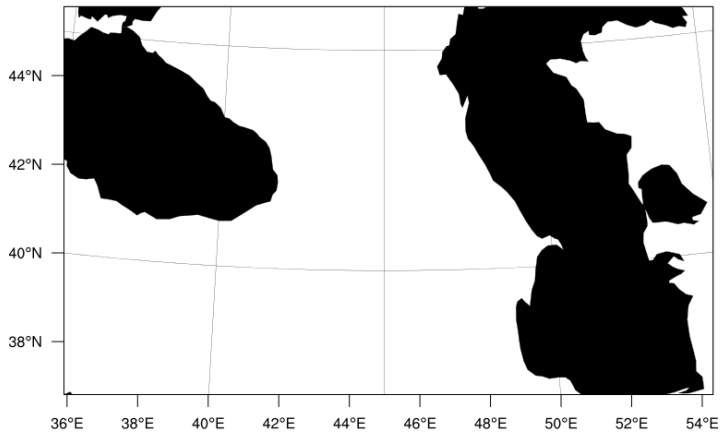

Figure 3.3: Model simulation domain.

$$R = \sum_{t} q_t e_t (\triangle t)^2 \tag{3.1}$$

where q_t is the surface runoff rate (mmhr^{-1}) and e_t is the kinetic energy flux ($\mathrm{Jm}^{-2}\mathrm{hr}^{-1}$) at time t of rain falling over a time period $\triangle t$ of 30 minutes. The only difference between equation 3.1 and equation 1.28 is that here erosivity is evaluated for all time steps and model grids, rather than only during storms. Kinetic energy flux was calculated from rain intensity according to both RUSLE and USLE parameterisations (equations 1.30 and 1.29). To avoid including runoff from snowmelt, data were excluded wherever there was snow on the ground. Only warm (liquid) rain was included in the analysis.

The fraction of total erosivity owing to low intensity rain (defined as rain lighter than the (R)USLE threshold of $2\,\mathrm{mmhr}^{-1}$), F_G, was computed using both RUSLE and USLE erosivities for each model grid:

$$F_G = \frac{R_{low}}{R} \tag{3.2}$$

with R_{low} calculated in the same way as R (equation 3.1) but including only time steps with rain intensity below the $2\,\mathrm{mmhr}^{-1}$ threshold. The normalisation by R permits a comparison of the importance of light rain between different areas, as the magnitude of erosivity will vary spatially. However, in regions with mostly light rainfall, F_G may be extremely high even if the total erosivity is very low. To avoid

this problem, a minimum erosivity threshold of $1\,\mathrm{Jm^{-1}}$ was applied to each grid. This threshold was chosen based upon Figure 4 from *Kinnell et al.* [1994], which regresses soil loss (in tons (T)/acre (A)) against erosivity (defined according to equation 3.1 in foot-tons (ft-T)×foot (ft)/acre(A)) for storms over a five year period on a plot in Mississippi. A storm with R=4 ft-T.ft/A ($1\,\mathrm{Jm^{-1}}$) produced about 10 T/A soil loss. Total erosivity was found to be insensitive to this threshold up to $10\,\mathrm{Jm^{-1}}$.

Similar terms for the grid level contribution of low intensity rain to the total rainfall amount (P_G), kinetic energy (E_G) and surface runoff (Q_G) are also defined:

$$X_G = \frac{X_{low}}{X} \tag{3.3}$$

where X may be substituted for grid total rain amount, kinetic energy or surface runoff.

A domain-wide measure of the contribution of light rain to erosivity was also computed, for which the total erosivity from low intensity rain was summed over the whole domain and normalised by the total erosivity from rain of all intensities:

$$F_D = \frac{\sum R_{low}}{\sum R} \tag{3.4}$$

The analogous expression for the contribution of low intensity rain to the domain total rainfall amount (P_D), kinetic energy (E_D) and surface runoff (Q_D) across the whole domain is

$$X_D = \frac{\sum X_{low}}{\sum X} \tag{3.5}$$

where again X can be substituted for rain amount, kinetic energy or surface runoff.

Some low intensity rain may in fact fall within storms that are included in the (R)USLE erosivity calculations, rather than falling between storms. In particular, this may be relevant in the build up and tail end of heavy rain events. To explore this, the contribution to erosivity of heavy rain days, S_G, used as a proxy for storm days, was calculated:

$$S_G = \frac{R_{heavy}}{R} \tag{3.6}$$

where R_{heavy} is the total erosivity in a model grid from heavy rain days, defined as days with at least one 30-minute period where precipitation intensity exceeds the 99^{th} percentile of rainy 30-minute periods for each grid.

3.3 Results

3.3.1 Model validation

Fig. 3.4 compares annual total precipitation between WRF, CFSR and two observational datasets, E-OBS [*Haylock et al.*, 2008] and GPCC [*Schneider et al.*, 2011]. CFSR does not assimilate precipitation observations, so the precipitation fields are 6-hour forecasts forced by assimilated observations [*Wang et al.*, 2010]. Both E-OBS and GPCC are gridded data products. At 0.25 degrees, E-OBS has a higher spatial resolution than GPCC, which is only available at 0.5 degree resolution. E-OBS is based on rain guage data at observational stations, and therefore contains some regions with incomplete coverage (as shown in Fig. 3.4a), while GPCC uses both satellite observations and rain guage data and is available over all land areas. Rain guages do not measure snowfall, so E-OBS data includes only liquid precipitation, while GPCC incorporates ice phases as well. GPCC data is monthly, while E-OBS is reported daily.

Both sets of observations demonstrate that precipitation in the Caucasus is strongly influenced by orography. Rainfall closely follows the terrain, increasing at higher elevations (Fig. 3.4, Fig. 3.2). This gives justification for using a regional climate model run at sufficient spatial resolution to capture these features. Both E-OBS and GPCC show a precipitation maximum to the east of the Black Sea, which extends to the south-west along the mountain range. This maximum is greater in the GPCC data than in E-OBS, which may be attributable to snowfall in the mountains. There is substantially less precipitation in the east of the domain. Rainfall observations in the south-west of the domain cannot be compared because of a lack of E-OBS data coverage in this area.

The spatial pattern of WRF precipitation agrees well with observations, with most rain occurring around the eastern coast of the Black Sea and in the mountains (Fig. 3.4c). The structure of the precipitation field produced by WRF differs from the CFSR field (Fig. 3.4d), with the influence of the complex terrain evident in the

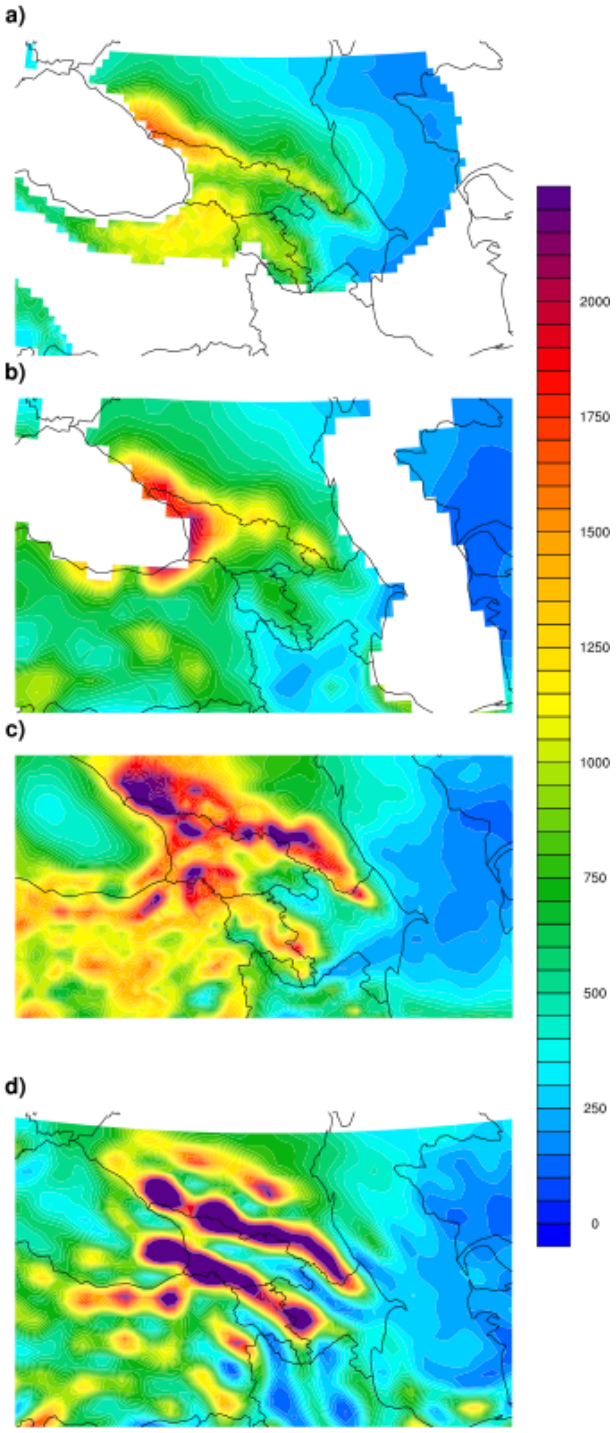

Figure 3.4: Total annual precipitation (mm) in 2009 from gridded observational datasets a) E-OBS and b) GPCC, and from c) WRF and d) CFSR models. White areas in a) and b) are regions with no data coverage.

WRF model, especially in the detail of the pattern around the Greater Caucasus Mountains (see Fig. 3.2).

The bias in WRF precipitation compared with EOBS and GPCC is shown in Fig. 3.5. It is clear that WRF has a wet bias, particularly in the mountains, compared with both datasets. The maximum east of the Black Sea is greater than in both sets of observations. However, there is also disagreement between the observations (Fig. 3.4a, b). WRF agrees reasonably well with E-OBS in the area south-east of the Black Sea, but GPCC suggests less rainfall occurred here. Between the Black and Caspian Seas, the wet bias is greater relative to E-OBS data than to GPCC. The precipitation bias in WRF can largely be attributed to problems in the forcing model, CFSR, which produced significantly more rainfall in the mountains than WRF, and an additional band of heavy precipitation south of this (Fig. 3.4d). This is consistent with *Wang et al.* [2010], who found a positive precipitation bias in CFSR over this region for the period from 1979 to 2008.

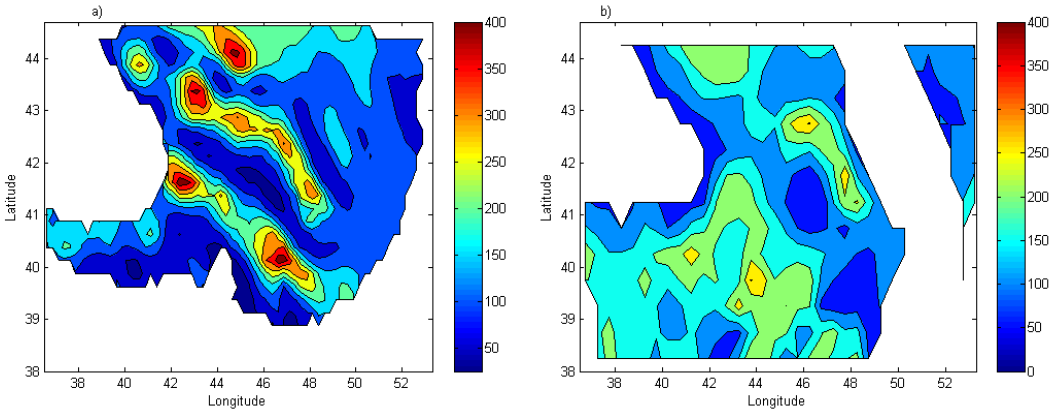

Figure 3.5: Relative bias (%) between WRF and a) E-OBS and b) GPCC total annual precipitation. For both maps, WRF was regridded onto the coarser resolution grid to permit a direct comparison. White areas represent grids with missing observational data.

Domain-mean total rainfall for the year was 616 mm in E-OBS and 686 mm in GPCC. To enable a more direct comparison, WRF and CFSR model output were regridded onto the E-OBS and GPCC grids, and grids/time steps with missing data were excluded from the validation. Given the different geographical coverage of the observations, this resulted in quite different areas being considered for each validation. Over the E-OBS area, mean total precipitation in WRF was 903 mm (bias of +46% compared with E-OBS), and 965 mm in CFSR (+57% compared with E-

OBS). For the GPCC area (all land areas), mean total precipitation was 996 mm in WRF (+45% compared with GPCC) and 959 mm in CFSR (+40% compared with GPCC). The GPCC area includes the south-west corner of the domain, where WRF rains more than the forcing model CFSR.

The seasonal picture is similar (Fig. 3.6). The spatial pattern in WRF follows observations better than CFSR, but the amount of precipitation is higher in both models. Spatially, WRF agrees least well with the observations during spring (MAM) and summer (JJA), when it shows the largest wet bias, reflecting the bias in CFSR during these months. The strong summer bias suggests that the excess rain produced by WRF may be partly attributable to the cumulus scheme, as convection is strongest in summer. WRF domain-averaged precipitation matches very well with observations in the later months, but overestimates rainfall in the first part of the year (Fig. 3.7).

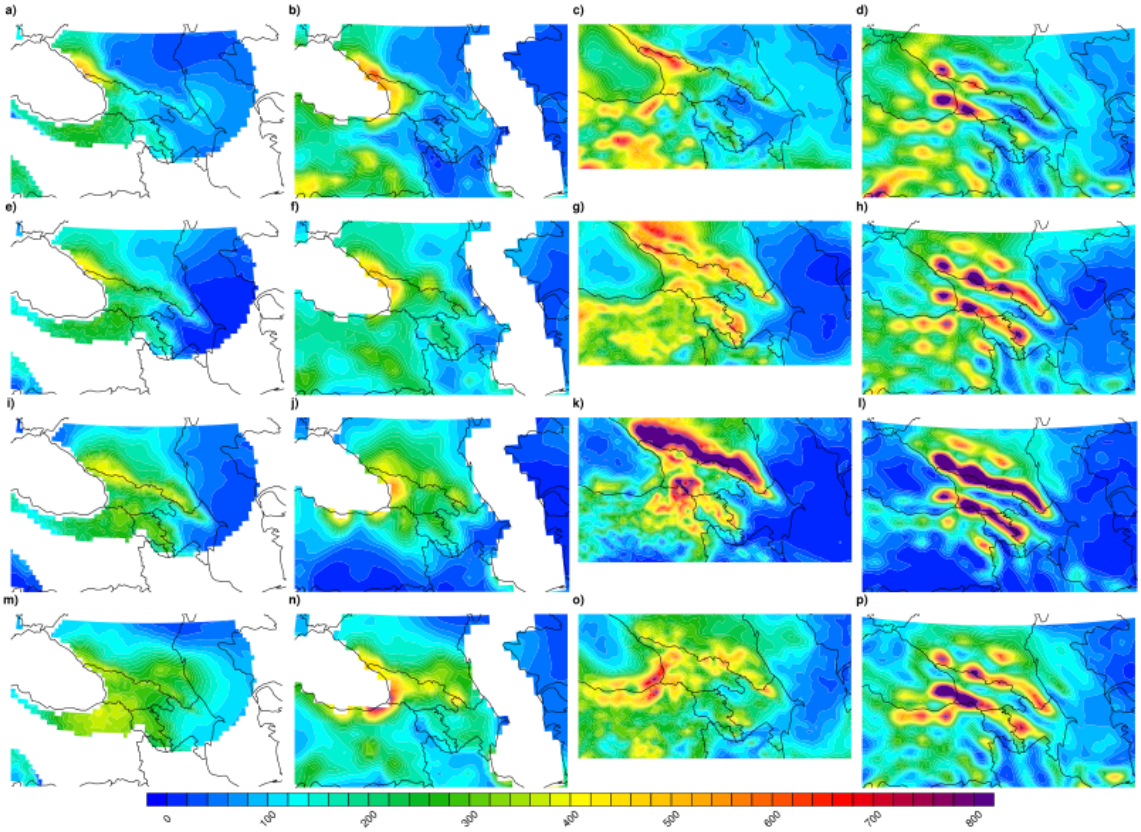

Figure 3.6: Seasonal total precipitation (mm) in 2009 from E-OBS (first column), GPCC (second column), WRF (third column) and CFSR (fourth column) for DJF (top row), MAM (second row), JJA (third row) and SON (fourth row).

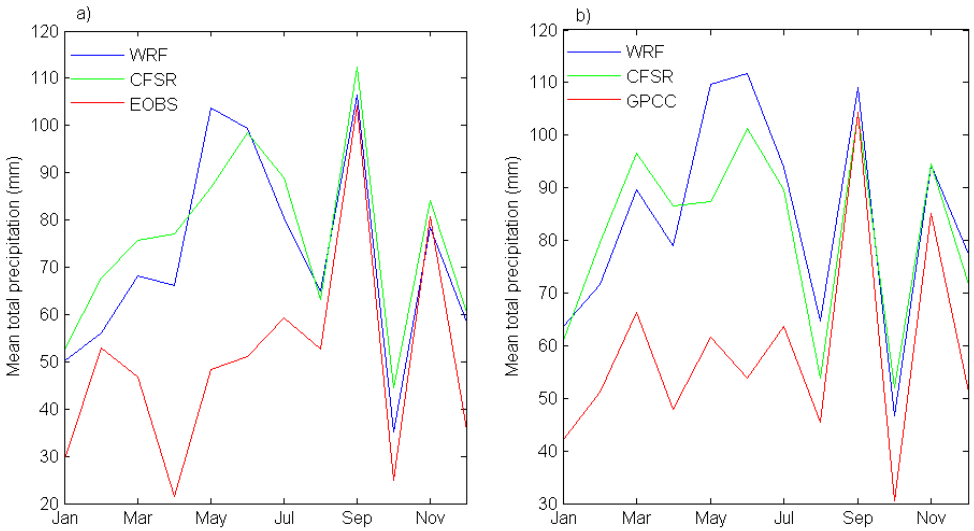

Figure 3.7: Monthly total precipitation in the model domain from WRF (blue), CFSR (green) and a) E-OBS (red) or b) GPCC (red). Data points which were missing from a) the E-OBS dataset and b) GPCC were also excluded from the model data for each comparison.

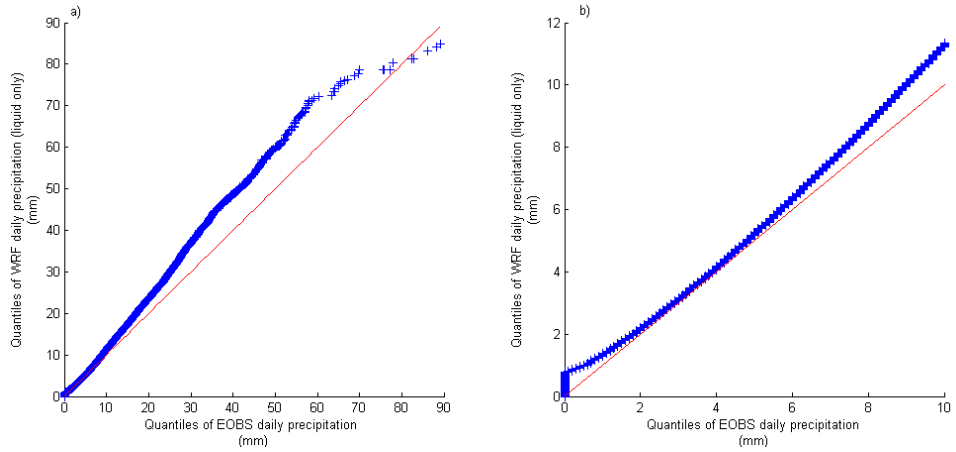

Figure 3.8: Quantile-quantile plots for grid daily precipitation (mm) between WRF and E-OBS. A quantile-quantile plot is a scatter plot between the quantiles of two distributions. For two identical distributions, the points would lie along the $x = y$ line (shown in red). Daily data from all grids were pooled to calculate the quantiles of each distribution. Liquid precipitation was used for WRF to enable a more direct comparison with EOBS rain guage data, but a similar analysis using total precipitation did not change the results.

Sub-storm data is needed to calculate rainfall erosivity. In the absence of higher

frequency observations, a validation of daily rainfall in WRF compared with E-OBS was performed across all grids (Fig. 3.8). The highest quantiles of WRF daily rainfall lie above the $x = y$ line in the quantile-quantile plot, indicating that WRF produces too much heavy rain compared with observations (Fig. 3.8a). WRF also produces too much light rainfall (Fig. 3.8b). There are substantially more rainy days in WRF than were observed (80% compared with 32%); this can also be seen in Fig. 3.8b, where E-OBS has more zero rain quantiles than WRF. A quantile-quantile plot between daily precipitation in WRF and CFSR indicates that these biases can be attributed to the forcing model (Fig. 3.9).

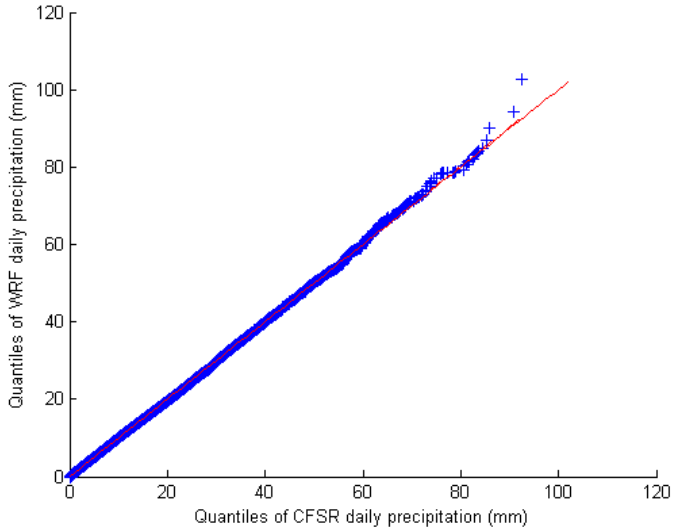

Figure 3.9: Quantile-quantile plot between WRF and CFSR grid daily total precipitation quantiles. Daily data from all grids were pooled to calculate the quantiles of each distribution. Total precipitation was used for WRF for direct comparison with total precipitation data from CFSR.

Tab. 3.1 gives the average fraction of total rainfall from days with rain below a range of minimum daily intensity values. The ratio of these fractions gives the bias in the fraction of total rain from low intensities in WRF compared with E-OBS daily data. The contribution of days with intensity below 5 mmday^{-1} is too high, while it is too low for days below 48 mmday^{-1}. This implies that the contribution from days between 5 and 48 mmday^{-1} is too low in WRF. The daily equivalent of the (R)USLE minimum intensity threshold of 2 mmhr^{-1} is 48 mmday^{-1}, but the bias in the fraction of daily light rainfall cannot be assumed to be representative of the sub-daily bias. The mean fraction of total grid rainfall from 30-minute rain below

$2\,\mathrm{mmhr}^{-1}$ in WRF is 76%, compared with 99% for daily rain below $48\,\mathrm{mmhr}^{-1}$.

Daily intensity threshold (mmday^{-1})	WRF	E-OBS	$\frac{\text{WRF}}{\text{E-OBS}}$
2	0.16	0.09	1.73
5	0.35	0.31	1.14
10	0.58	0.61	0.96
20	0.83	0.88	0.94
40	0.97	0.99	0.99
48	0.99	0.99	0.99

Table 3.1: Grid-averaged fraction of total rainfall from days with rain below the given intensity thresholds in WRF and E-OBS, and the relative bias in this fraction.

3.3.2 The contribution of light rain to erosivity

Contours of QE erosivity, calculated using the RUSLE and USLE energy relations, are shown in Fig. 3.10; results are similar for the two measures. It is clear that there is significant spatial heterogeneity. Erosivity closely follows the rainfall pattern (Fig. 3.4), with higher values east of the Black Sea and lower values south and further east near the Caspian Sea.

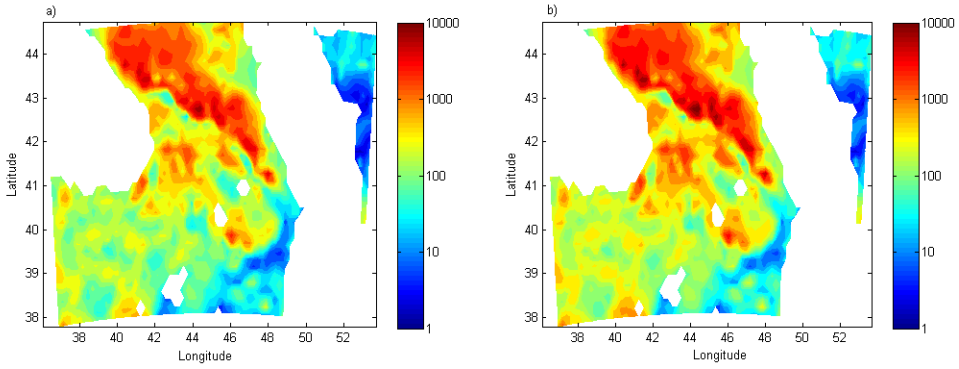

Figure 3.10: Contours of QE erosivity (Jm^{-1}) using a) RUSLE and b) USLE kinetic energy parameterisations. Note the log colour scale.

Fig. 3.11 shows contours of the contribution of rain below $2\,\mathrm{mmhr}^{-1}$ to RUSLE

erosivity (F_G), RUSLE rainfall kinetic energy (E_G), total rainfall (P_G) and surface runoff (Q_G). It appears that light rain is more important for total erosivity in areas of high terrain in most of the domain, but correlation coefficients (r) between F_G and terrain height were only 0.07 for both RUSLE and USLE. Correlations between terrain height and E_G, P_G and Q_G were also negligible. This is because of the low lying area east of the Caspian Sea with low rainfall levels (Fig. 3.4) and a high fraction of erosivity from light rain (Fig. 3.11a). In the rest of the domain light rain contributes more to erosivity at height (r=0.27 between F_G and height for both RUSLE and USLE), owing to a higher proportion of surface runoff from light rain at higher elevations (r=0.19 between Q_G and height).

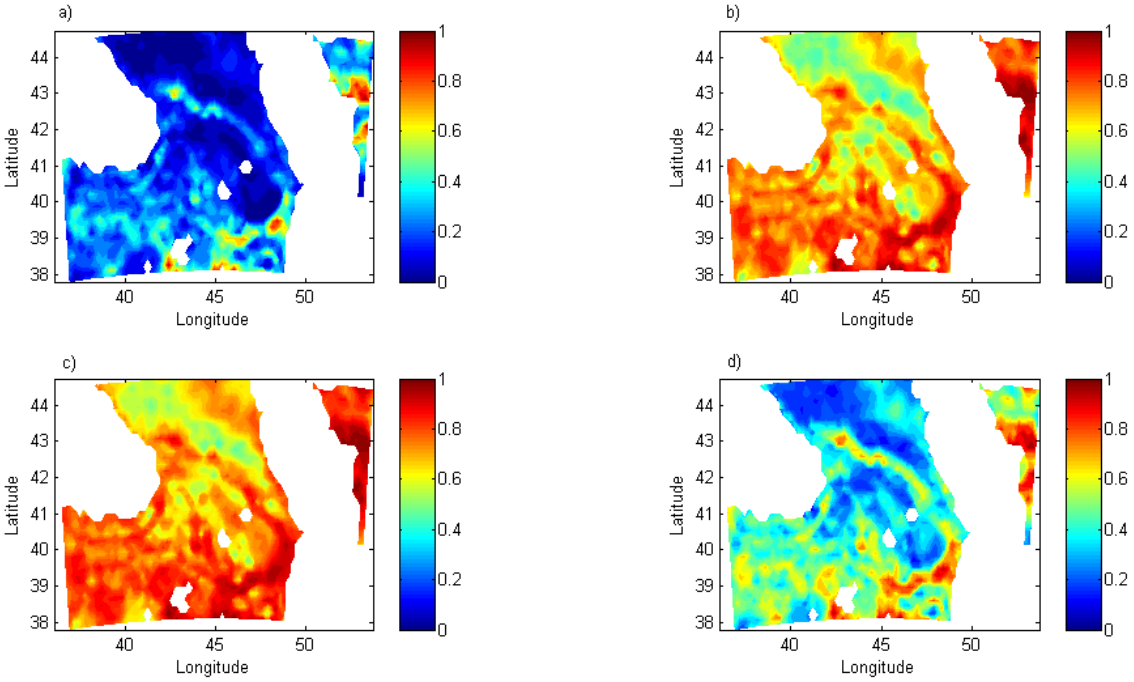

Figure 3.11: Contribution of light rain ($<2\text{mmhr}^{-1}$) to total a) RUSLE erosivity (F_G), b) RUSLE rainfall kinetic energy (E_G), c) total rainfall (P_G) and d) surface runoff (Q_G).

Tab. 3.2 gives the average grid values (average is indicated by "<>") and the first and third quartiles of the contributions of light rain to erosivity, kinetic energy, total rainfall and surface runoff. On average in each grid, 76% of rain is below $2\,\text{mmhr}^{-1}$, and delivers 72% and 67% of total rainfall kinetic energy according to the RUSLE and USLE, respectively. With a minimum energy of $8\,\text{Jm}^{-2}\text{mm}^{-1}$, the importance of light rain is always inflated in the RUSLE (Fig. 1.7). Not all this rain is erosive,

as surface runoff must also be present to transport detached sediment particles. The contribution of light rain to surface runoff (45%) is lower than for rainfall amount or kinetic energy. This leads to a 23% contribution of light rain to both RUSLE and USLE erosivities, reduced by comparison with the contribution to total rain amount and kinetic energy, but nonetheless substantial.

Across the domain, 13% of total erosivity (in both RUSLE and USLE) is from light rainfall (F_D), lower than the grid average of 23% ($< F_G >$). This reflects the fact that most erosivity in the domain occurs in areas where rainfall is heavy. In other parts of the domain, erosivity is lower and light rain plays a more important role. The most erosive area is in the centre of the domain in the north (Fig. 3.10) where rainfall is heavy (Fig. 3.4) and the proportion of erosivity owing to light rain is low (Fig. 3.11a). The domain wide measure (F_D, equation 3.4) is weighted towards the most erosive areas, but the spatial heterogeneity evident in Fig. 3.11 limits the usefulness of this measure. In contrast, the grid level measure (F_G, equation 3.2) weights each model grid equally, even though some are considerably more erosive than others. Employing a minimum erosivity threshold to avoid considering areas with insignificant erosion caused entirely by light rain permits a useful analysis using $< F_G >$.

		Fraction	q_1	q_3
RUSLE	$< F_G >$	0.23	0.10	0.31
	$< E_G >$	0.72	0.63	0.81
USLE	$< F_G >$	0.23	0.10	0.30
	$< E_G >$	0.67	0.57	0.76
	$< P_G >$	0.76	0.68	0.84
	$< Q_G >$	0.45	0.32	0.56

Table 3.2: Average contributions of low intensity rainfall (below $2\,\mathrm{mmhr}^{-1}$) to erosivity, total rain amount, rainfall kinetic energy and surface runoff in each grid. The first and third quartiles (q_1 and q_3) are given for the grid values. $< F_G >=< \frac{R_{low}}{R} >$ and $< X_G >=< \frac{X_{low}}{X} >$, where X is grid total kinetic energy (E), rainfall amount (P) or surface runoff (Q) and X_{low} is grid total E, P or Q from rain intensities below $2\,\mathrm{mmhr}^{-1}$ (sec. 3.2.2).

The sensitivity of $< F_G >$ and F_D to the threshold adopted for low intensity rainfall ($2\,\mathrm{mmhr}^{-1}$ in the (R)USLE) is explored in Fig. 3.12. This again shows that low intensity rain contributes more to total erosion in the RUSLE than the USLE, and that the average contribution of light rain in a model grid is greater than across the

domain. Including more light rain by lowering the threshold accounts for a greater fraction of total erosivity. The fraction of domain total erosivity from light rain (F_D) falls below 10% when the light rain threshold is reduced below about 1.8 mmhr^{-1}. For the grid average, the proportion of erosivity excluded by focussing on heavy rain alone only reduces to 10% with a threshold of about 1.4 mmhr^{-1}.

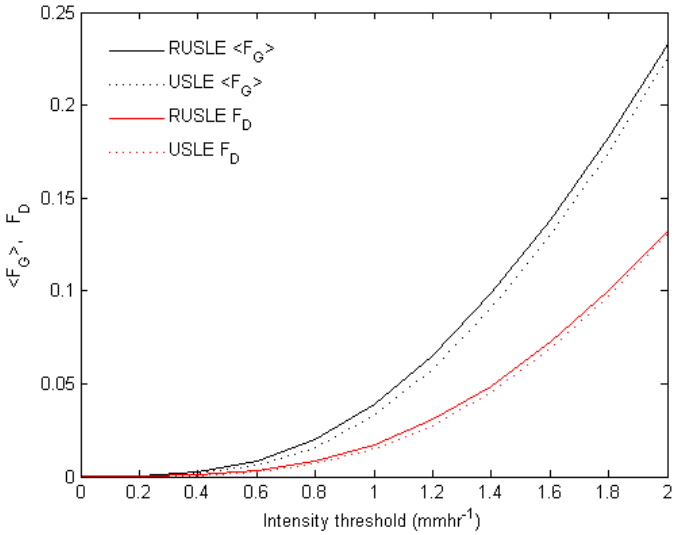

Figure 3.12: Average contribution of low intensity rain to erosivity in a grid, $< F_G >$ (black), and across the domain, F_D (red), as a function of the threshold used to define low intensity rain in the RUSLE (solid lines) and USLE (dotted lines).

Fig. 3.13 shows contours of the fraction of total grid RUSLE erosivity attributable to storm days, S_G, defined using the 99$^{\text{th}}$ percentile of 30-minute rain intensity (sec. 3.2). A reduction in the contribution of storm days to erosivity in the mountains mirrors the increase in the contribution of low intensity rainfall to erosivity (Fig. 3.11a). A correlation coefficient of -0.51 was found between S_G and terrain height. Erosion in the mountains is due more to low intensity non-storm precipitation than in low-lying regions.

Fig. 3.14 shows the average fraction of erosivity from storm days, $< S_G >$, as a function of the percentile of 30-minute rain intensity used to define a storm day. Very heavy rain days (99$^{\text{th}}$ percentile) are responsible for 69% and 70% of total grid erosivity in the RUSLE and USLE, respectively. This proportion increases as less intense storm days are included. For weaker storms, e.g. the 95$^{\text{th}}$ percentile, only 3% of erosivity is caused by non-storm rain. Percentiles of 30-minute rain intensity

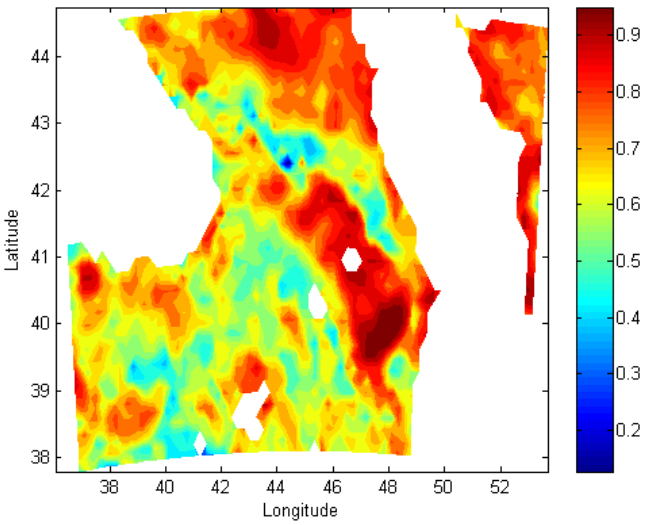

Figure 3.13: Fraction of total RUSLE erosivity owing to storm days, S_G. Storm days are defined as days where at least one 30-minute period exceeds the 99$^{\text{th}}$ percentile of 30-minute rainfall intensity.

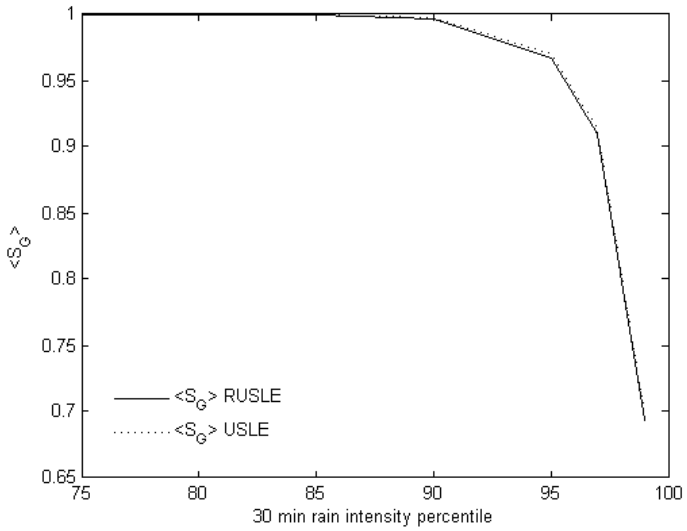

Figure 3.14: Average fractional contribution of heavy rain days to total erosivity in a grid, $< S_G >$, as a function of the percentile of 30-minute rainfall used to define a heavy rain day, for RUSLE (solid line) and USLE (dotted line). The fraction of domain total erosivity attributable to storm days, S_D, was similar and is not shown.

are given in Tab. 3.3, which also shows the values of $< S_G >$ plotted in Fig. 3.14. The (R)USLE low intensity threshold of $2\,\mathrm{mmhr}^{-1}$ lies between the 97^{th} and 99^{th} percentiles. Non-storm rain therefore contributes between 9 and 30% to erosivity in the (R)USLE. This is consistent with the finding that 23% of total erosivity in a grid is from rain below $2\,\mathrm{mmhr}^{-1}$.

Percentile	Intensity (mmhr^{-1})	$< S_G >$ RUSLE	$< S_G >$ USLE
75	0.16	1.00	1.00
80	0.24	1.00	1.00
85	0.37	1.00	1.00
90	0.60	1.00	1.00
95	1.06	0.97	0.97
97	1.42	0.91	0.91
99	2.27	0.69	0.70

Table 3.3: Grid-averaged 30-minute rain intensity percentiles (mmhr^{-1}), and average contribution of storm days to total grid erosivity in the RUSLE and USLE, with storms defined as days with at least one 30-minute period greater than the percentiles listed.

These results will depend upon the proportion of light rain in the local climate, and may therefore vary between regions. Fig. 3.15 shows the relationship between RUSLE F_G and the proportion of rain below $2\,\mathrm{mmhr}^{-1}$ in a grid, P_G. An exponential fit to these data is also shown: $F_G = a\exp^{(bP_G)}$. The coefficients of the fit for both RUSLE and USLE are given in Tab. 3.4. The average of these coefficients results in the following fitted equation:

$$F_G = 0.002\exp(6P_G) \tag{3.7}$$

	a $\times 10^{-3}$	a- $\times 10^{-3}$	a+ $\times 10^{-3}$	b	b-	b+	R^2	RMSE
RUSLE	2.06	1.75	2.37	5.97	5.80	6.14	0.76	0.08
USLE	1.93	1.63	2.23	6.00	5.83	6.18	0.75	0.08

Table 3.4: Coefficients in the fitted equation $F_G = a\exp(bP_G)$, with lower (-) and upper (+) confidence bounds, for erosivity calculated using RUSLE and USLE kinetic energies.

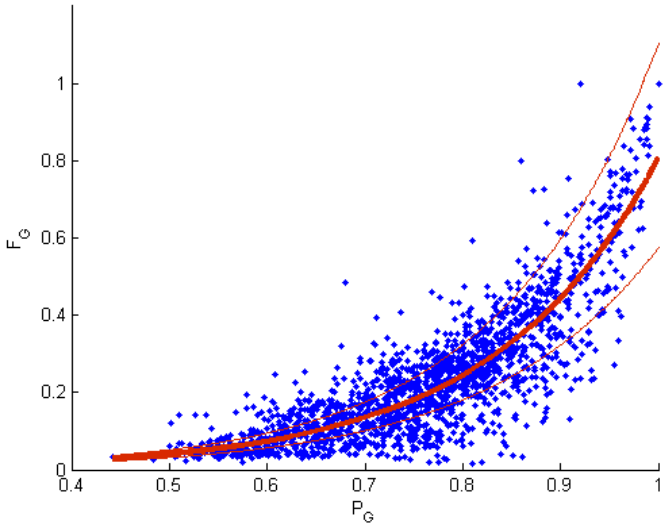

Figure 3.15: Scatter plot and exponential fit between the contribution of light rain ($< 2\,\mathrm{mmhr}^{-1}$) to RUSLE erosivity, F_G, and the fraction of light rain in a grid, P_G. An exponential fit to the data is also shown (bold red line) with upper and lower bounds for 95% confidence in the fit. The same plot for USLE F_G was similar and is not shown.

3.4 Discussion

3.4.1 Implications for erosion modelling

The results presented here show that light rain contributes significantly to rainfall erosivity (23%) in the Caucasus region, according to model results using WRF forced with CFSR data for 2009. Between 9 and 30% of erosivity may be excluded from the storm-based erosivity calculations in the (R)USLE model, even when light rain occurring within storms is accounted for. This finding is consistent with *Wischmeier* [1959] who found that the USLE accounted for 72-85% of yearly variations in soil loss in the United States, though this figure includes variability in soil processes as well as in erosivity. It is also broadly quantitatively consistent with studies that observed significant erosion during light rain [*Kirkbride and Reeves*, 1993; *Baartman et al.*, 2012; *Marques et al.*, 2008].

The implications of this for erosion modelling with the (R)USLE are not obvious. The soil erodibility term, K (equation 1.26), defined empirically as the ratio of total soil loss to erosivity over a long term period, implicitly corrects for errors in the calculation of the erosivity term. Therefore, when used to model long term soil loss,

the effects of light rain are accounted for by the erodibility factor. However, for shorter timescales and event erosion modelling this is not the case because of the high variability in F_G. The (R)USLE was not intended for event erosion prediction, but is nonetheless widely used for this purpose [*Kinnell*, 2010].

Emphasis is placed on obtaining good fits for energy-intensity parameterisations at high intensities, as these events are considered most erosive. The RUSLE and USLE energy-intensity relations are therefore least accurate for low intensity rainfall (Fig. 1.7). An accurate means of computing rainfall kinetic energy at low intensities would be required to obtain a clearer indication of the importance of light rain for erosivity. The method proposed in chapter 4 could be used for this. However, despite differences between the energies of light rain in the RUSLE and USLE, the dependence of $< F_G >$ on the minimum intensity threshold is very similar, indicating that this is not likely to change the main findings of this study (Fig. 3.12)

3.4.2 Exponential relationship between F_G and P_G

An exponential dependence of the contribution of light rain to erosivity on the proportion of light rain was found (equation 3.7, Fig. 3.15). In a heavy rain regime, an increase in the proportion of light rainfall will have little impact on kinetic energy and erosivity, which are dominated by the upper end of the rain distribution. In contrast, in a regime dominated by light rain (with little total erosion), small increases in the proportion of light rain have a larger impact on energy and erosivity. This is exacerbated by the non-linear dependence of kinetic energy on intensity; kinetic energy is particularly sensitive to light rain (Fig. 1.7).

This relation can be used to correct for a bias in the fraction of light rainfall in the modelled climate. The problems revealed by the validation in sec. 3.3.1 suggest that an alternative model setup might give more reliable results. Using an alternative reanalysis with a lower precipitation bias for the boundary forcings, for example, or experimenting with different cumulus or microphysics parameterisations in WRF might produce a more realistic model climate. However, a different model setup may not offer an improvement. *Wang et al.* [2010] showed that two other reanalyses (NCEP/NCAR and NCEP/DOE) had a positive precipitation bias in the Caucasus, while ECMWF ERA-40 produced too little precipitation. For every model configuration there will be some bias, and equation 3.7 allows this to be corrected without the need for costly and time consuming additional model simulations. The

correction can only be approximate, as there is significant scatter around the fitted relationship (Fig. 3.15). As only daily precipitation observations were available, the bias in the fraction of light 30-minute precipitation could not be estimated here. The average value of P_G was 76%, but Fig. 3.15 suggests that where at least 70% of rain is below $2\,\mathrm{mmhr}^{-1}$, this will contribute at least 10% to total erosivity.

Equation 3.7 could also be applied to estimate the importance of light rain for erosivity in other regions with different climates. For event erosion prediction, where the (R)USLE erodibility factor cannot account for the variability in F_G, it could be used to correct for the error incurred by excluding light rain. No attempt has been made to account for differences in soil type and slope, which are important determinants of surface runoff. This may affect the applicability of equation 3.7 to other areas. This equation is only appropiate for local scales, given the spatial heterogeneity of F_G and P_G (Fig. 3.11).

3.4.3 Limitations

The RUSLE and USLE guidelines are not clear about how to employ the minimum threshold of 0.5 inches over 6 hours. In this study, this was downscaled to an equivalent 30-minute threshold of 1 mm (or a rate of $2\,\mathrm{mmhr}^{-1}$) to allow an analysis at sub-storm frequencies. To test whether the main conclusions are affected by this, data was aggregated into 6 hour periods, and the importance of rainfall below 0.5 inches (12.7 mm) was computed. Periods with less than 12.7 mm constituted 88% of total rainfall and 57% of total erosivity in both the RUSLE and USLE, on average in each grid, compared with 76% and 23% using 30-minute data. This lies within the confidence bounds of the exponential relationship between F_G and P_G (Fig. 3.15). At a time resolution of 6 hours, more light rainfall may fall within storms, as a 6 hour period can consist of both light and heavy 30-minute intervals. It might therefore be expected that the contribution to erosivity from non-storm days might be reduced using the aggregated 6 hour data.

These results are based on one year of model data, but a longer simulation period would give greater statistical confidence in the exponential fit between F_G and P_G. WRF precipitation was validated against observations, but erosivity also depends on surface runoff. This would also need to be validated for a full assessment, but lack of runoff data at sufficient temporal and spatial resolutions prevented this.

3.5 Conclusions

The contribution of low intensity rain to rainfall erosivity during 2009 in the Caucasus was investigated using a WRF model simulation at 20 km resolution, with reanalysis boundary conditions from CFSR. Erosivity, defined as the product of rainfall kinetic energy and surface runoff, was calculated according to the kinetic energy-intensity relationships used in two widely used soil erosion models, the RUSLE and the USLE, from 30-minute model precipitation and runoff data.

Rainfall intensities below 2 mmhr^{-1} were found to contribute 23% to total erosivity on average in a model grid, for both the RUSLE and USLE. Accounting for light rain that falls within storms, between 9 and 30% of erosivity may be excluded from the storm-based erosivity calculations in the (R)USLE models. (R)USLE guidelines should be more specific about the recommended treatment of low intensity rainfall in the build up and tail end of storms. Excluding light rain does not lead to errors in (R)USLE predicted soil loss over long periods, but could cause an underestimation of soil loss from individual events.

An exponential dependence of the contribution of light rain to erosivity on the proportion of light rain in the local climate was found. This is applicable on local scales, and may be used to estimate the importance of light rain in other regions with different rainfall climatologies, or to correct for a bias in the model rainfall distribution when observations are available to quantify this. It can also serve to correct for the error incurred by ignoring light rainfall in event erosion prediction.

The importance of light rain for erosion can only truly be answered using observations. However, these findings are consistent with observations from different regions, which suggest that low intensity rain can cause substantial erosion [*Kirkbride and Reeves*, 1993; *Baartman et al.*, 2012; *Marques et al.*, 2008].

4 Dynamic simulation of rainfall kinetic energy flux

4.1 Introduction

Rainfall kinetic energy is an important variable for soil erosion prediction and is commonly used in empirical and physical erosion models. Difficulties in measuring rainfall kinetic energy, however, have led to the development of equations parameterising kinetic energy from intensity in a wide range of locations worldwide, based upon measurements of raindrop size spectra. This approach has several drawbacks. First, there is evidence of significant variability in kinetic energy for a given intensity of rain, owing to variations in drop size spectra and/or deviations of raindrops from terminal velocity [*Rosewell*, 1986; *Kinnell*, 1981; *Fox*, 2004; *Parsons and Gadian*, 2000; *Steiner and Smith*, 2000]. Second, since energy-intensity equations are developed based on data at a given location, their applicability to other regions is questionable. Third, emphasis is placed on providing a good fit for these parameterisations at high rain intensities, as these generally constitute the most erosive events [*Van Dijk et al.*, 2002]. This can result in quite unrealistic predictions of energy at low intensities, such as positive values at zero intensity in the RUSLE [*Renard et al.*, 1997] or negative values at low intensities in the USLE [*Wischmeier and Smith*, 1958] (sec. 1.3.2). However, there is evidence to suggest that low intensity rain can in fact contribute significantly to erosion [*Kirkbride and Reeves*, 1993; *Marques et al.*, 2008; *Baartman et al.*, 2012] so the use of many energy-intensity equations may not be appropriate in these situations.

This chapter presents a new approach to soil erosion research, using a cloud resolving model to dynamically simulate the kinetic energy of rain from basic physics. The results demonstrate that the model is capable of producing energies within the range of observations from several studies reported in the literature. These methods may

easily be applied in a full regional climate model. Aside from avoiding the shortfalls of assuming a fixed relationship with intensity, using a regional climate model to simulate rainfall kinetic energy offers the opportunity to perform a range of studies investigating the role of the climate in erosion and of factors that may influence this.

4.2 Methods

Kinetic energy can be calculated for rainfall given assumptions about the size and speed of raindrops. The kinetic energy, k, of a falling raindrop with diameter D is given by

$$k(D) = \frac{1}{2}M(D)V(D)^2 \tag{4.1}$$

where $M(D)$ is the mass of the raindrop and $V(D)$ is its fall speed. For a raindrop size distribution, $N(D)$, the total kinetic energy flux (the rate of kinetic energy transfer from the drops to the ground) is the sum of the flux from all raindrops in the distribution, given by

$$e(D) = \frac{1}{2}\int_0^\infty N(D)M(D)V(D)^3 dD \tag{4.2}$$

As described in sec. 1.2, $N(D)$ is commonly approximated by either an exponential or gamma distribution, both of which may be expressed in the general form given by equation 2.9. Adopting the common assumption that raindrops are spherical, their mass follows equation 1.23 with $c = \pi\rho_w/6$, where ρ_w is the density of water (taken to be $1000\,\mathrm{kgm}^{-3}$). Further assuming that drops fall at their terminal velocity according to equation 2.14, the solution to equation 4.2 is:

$$e(D) = \sqrt{\frac{\rho_0}{\rho}}\frac{ca^3N_T}{2}\frac{\Gamma(\mu+3b+4)}{\Gamma(\mu+1)}\frac{\lambda^{\mu+1}}{(\lambda+3f)^{\mu+3b+4}} \tag{4.3}$$

N_T is the total number concentration of raindrops and $\sqrt{\frac{\rho_0}{\rho}} = 1$ at the surface (see sec. 1.2 for a description of the terms in this equation).

The four WRF microphysics parameterisation schemes described in sec. 1.2 (Thompson, Morrison, Milbrandt-Yau (MY) and WDM6) all assume a drop size distribution

of the form given in equation 2.9 but use different values for the shape parameter, μ, which may be fixed (Morrison and WDM6) or user defined (Thompson and MY). When μ=0 the DSD follows an exponential form, while μ=1 gives a first order gamma distribution.

Rainfall kinetic energy flux at the surface was modelled according to equation 4.3 using a simple idealised cloud resolving version of WRF version 3.4. This includes the complete microphysics parameterisations of the full model but contains no radiation or land surface scheme (no surface heat and moisture fluxes or frictional effects) and neglects the effects of the Earth's rotation (no Coriolis force). Simulations of a supercell storm were performed using all four microphysics schemes. For Thompson and MY, simulations with both exponential and gamma distributions were performed. The six simulations will be referred to hereafter as Thompson-0, Thompson-1, MY-0, MY-1 (with μ =0 or 1 as indicated), Morrison (fixed μ=0), and WDM6 (fixed μ=1).

The idealised supercell storm simulated was the default WRF case study. The storm was initialised with no topography in a domain of area 84 km x 84 km with a horizontal resolution of 2 km and 41 vertical levels between the surface and the model top height at 20 km. Initial soundings for potential temperature and water vapour mixing ratio were taken from *Weisman and Klemp* [1982], with the tropopause positioned at 12 km. Vertical wind profiles from *Weisman and Rotunno* [2000] were used, but shear was extended to 7.25 km instead of 6 km, with quarter-circle shear (in both x- and y-directions) up to 2.25 km, and shear only in the x-direction above this. The storm was initiated by a potential temperature perturbation of 3 K centred in the middle of the domain at 1.5 km above the surface. The perturbation had a radius of 10 km in the horizontal and 1.5 km in the vertical direction and tapered to zero at the storm edge [*Morrison and Milbrandt*, 2010]. All boundaries were open, and model variables were extracted every 10 minutes.

The relationship between modelled kinetic energy flux and intensity, i, was approximated by a power law following the same methodology as *Steiner and Smith* [2000] (hereinafter SS00):

$$e = A_B i^B \tag{4.4}$$

The coefficients A and B were chosen by iterative variation of B to minimise the root mean squared error, $RMSE$, across all m data points, given by SS00:

$$RMSE = 100\% \sqrt{\frac{1}{m-2} \sum_{j=1}^{m} \left[\frac{\left(i_j - (e_j / A_B)^{1/B} \right)}{i_j} \right]^2} \tag{4.5}$$

B was varied from 0.1 to 2.0, covering the full range of values tested in SS00 and A was calculated from equation 4.4 according to

$$A_b = \left[\frac{\sum_{j=1}^{m} e_j^{1/B}}{\sum_{j=1}^{m} i_j} \right]^B \tag{4.6}$$

4.3 Results and Discussion

4.3.1 Data comparison

Fig. 4.1 shows the modelled kinetic energy flux-rainfall intensity relationship for each of the six microphysics schemes studied. Data was averaged within $1\,\mathrm{mmhr}^{-1}$ intensity bins, and was found to be insensitive to bin size. The model results are compared with a sample of energy-intensity parameterisations ($e(i)$) from the literature (39 kinetic energy-intensity equations from a total of 22 observational studies chosen by *Salles et al.* [2002]). The model is capable of simulating rainfall kinetic energies within the range of observations: modelled kinetic energies for all schemes lie mainly within the bounds of the literature values for a given intensity. The only exceptions to this are the Morrison and MY-0 schemes, which produced higher kinetic energies at low and high intensities, respectively, but which nonetheless performed well overall. Correlation coefficients between bin-averaged modelled and literature energy values exceeded 0.97 for all schemes. Within a given scheme (Thompson, MY), using a gamma distribution (μ=1) instead of an exponential (μ=0) slightly lowered the kinetic energy flux in agreement with *Fox* [2004]. This is attributable to a narrowing of the drop spectra, resulting in fewer large drops.

Parameterising energy from intensity assumes that any variability around this fit is negligible. However, energy fluxes deduced from disdrometer data by SS00 (Fig. 4.2, taken from SS00) demonstrate that there is considerable variability in energy for a given intensity, a claim also supported by other observational studies [*Rosewell*, 1986; *Kinnell*, 1981; *Van Dijk et al.*, 2002], theory and literature reviews [*Fox*, 2004; *Parsons and Gadian*, 2000]. Modelled energy fluxes compare favourably with those

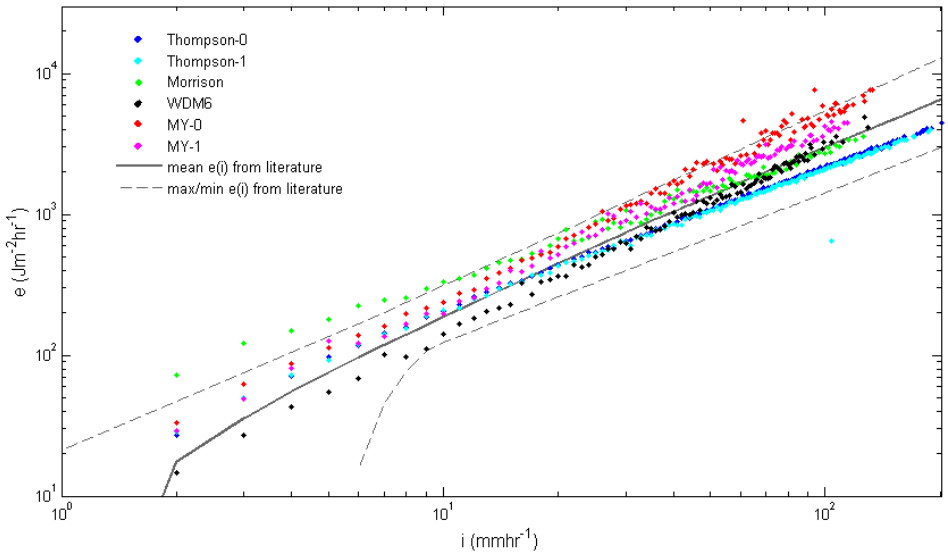

Figure 4.1: Bin-averaged modelled kinetic energy flux for each microphysics scheme (dots), and mean (solid line), and maximum/ minimum (dashed lines) kinetic energy values from energy-intensity relations in *Salles et al.* [2002]. Dark blue: Thompson-0, light blue: Thompson-1, green: Morrison, black: WDM6, red: MY-0, and pink: MY-1.

observations (Fig. 4.3), showing a large variance in energy for lighter rainfall which becomes more constrained at high intensities. Modelled energy fluxes are greater than observed at low intensities, particularly for the Morrison scheme. At high intensities, energy flux is greater than the observations in the MY-0 and MY-1 schemes, and less in the Thompson-1 and Thompson-0 schemes. These features are consistent with Fig. 4.1, where the schemes display similar behaviour relative to the mean literature energy-intensity curve. An interesting feature is the apparent bounding of observations between two limits above and below the model data. This is also present in the observations of SS00 (Fig. 4.2), and the authors suggest these limits are dependent on drop fall speeds and on upper/lower limits to raindrop size.

Comparing RMSE statistics for the energy-intensity power law fit given by equation 4.4, average model variability is greater than observed by SS00 (mean RMSE of 54% compared with 36%) but differs among schemes (Tab. 4.1). Morrison, WDM6 and MY-1 exhibited larger variances, while Thompson-0, Thompson-1, and MY-0 were closer to the observed value of 36%. This variability stems only from variations in drop spectra. Assumptions about drop terminal velocity, and any deviations from this, are additional sources of error which are discussed in further detail below.

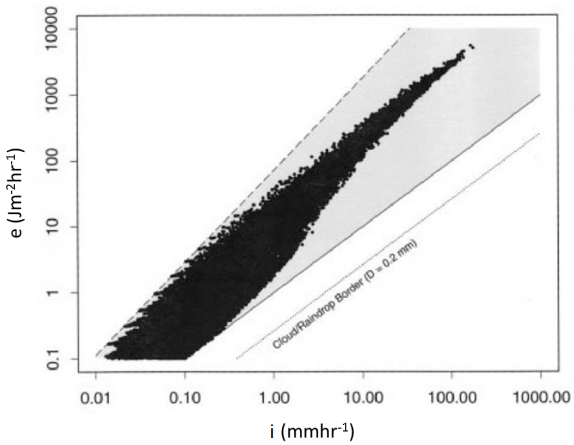

Figure 4.2: Radar observations of rainfall kinetic energy flux ($\mathrm{Jm^{-2}hr^{-1}}$) and rain intensity ($\mathrm{mmhr^{-1}}$), reproduced from Figure 3 of *Steiner and Smith* [2000].

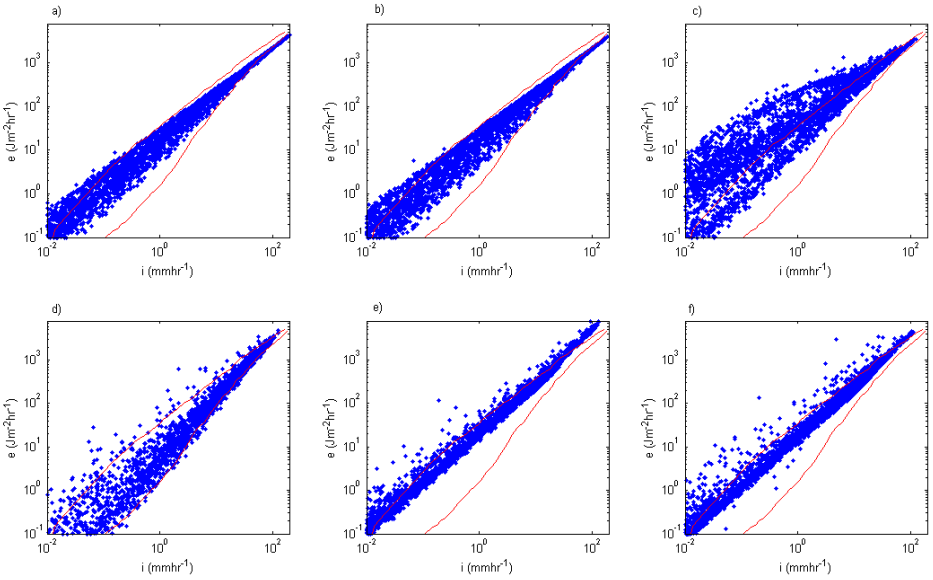

Figure 4.3: Outline of SS00 kinetic energy flux observations (red lines, taken from SS00 Figure 3, reproduced in Fig. 4.2) and modelled kinetic energy flux against rain intensity (blue dots) for a) Thompson-0, b) Thompson-1, c) Morrison, d) WDM6, e) MY-0 and f) MY-1 simulations.

Scheme	RMSE (%)	A	B
Thompson-0	25	21.1	1.0
Thompson-1	27	21.3	1.0
Morrison	83	154.3	0.5
WDM6	62	16.0	1.1
MY-0	50	29.4	1.1
MY-1	74	23.5	1.1

Table 4.1: Fit parameter values A and B, and RMSE (equation 4.5) for the fits given by equation 4.4 for each microphysics scheme.

4.3.2 Analysis of microphysics schemes

Closer examination reveals differing behaviours among the six microphysics options. As expected, rain water mass increases with intensity (Fig. 4.4c). However, Fig. 4.4 a) and b) reveal two categories of behaviour: schemes that distribute this rain mass among roughly the same number of drops of increasing size, or among an increasing number of raindrops of the same size. As intensity increases in WDM6, MY-0, and MY-1, raindrops become larger but not more numerous. By contrast, Morrison, Thompson-0 and Thompson-1 simply produce more raindrops of the same size. At higher intensities, additional raindrops are formed by melting frozen hydrometeors and forced breakup of raindrops.

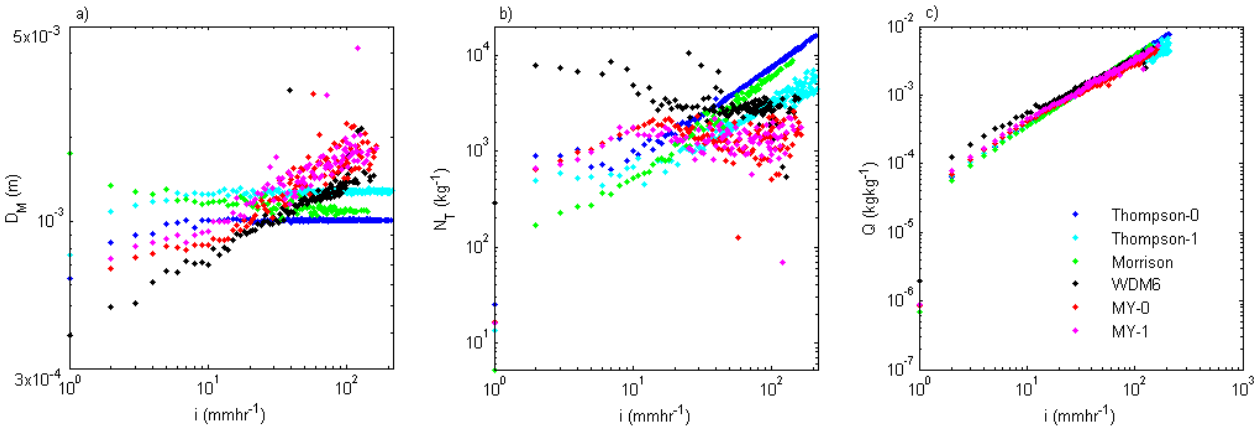

Figure 4.4: Average (a) raindrop size (mean-mass diameter, D_M), (b) raindrop number concentration, N_T, and (c) rainwater mass mixing ratio, Q, as a function of intensity for each model run. Averages were taken across the whole domain. Dark blue: Thompson-0, light blue: Thompson-1, green: Morrison, black: WDM6, red: MY-0, and pink: MY-1.

This contradicts observational evidence that drop size increases with intensity (e.g.,

Willis [1984]; *Abel and Boutle* [2012]). In these schemes, an overactive drop breakup parameterisation limits drop size (G. Thompson 2013, personal communication). In Thompson (WRF version 3.4), self collection and breakup follows *Verlinde and Cotton* [1993] and *Seifert and Beheng* [2001]:

$$\left|\frac{\partial N_T}{\partial t}\right|_{SC} = 4\xi_r N_T Q \tag{4.7}$$

$$\xi_r = \begin{cases} 1 & 50 < \mathrm{mvd_r} < 1.8\mathrm{mm} \\ 2 - \exp\left[2300 \times (\mathrm{mvd_r} - 1750 \times 10^{-6})\right] & \mathrm{mvd_r} > 1.8\mathrm{mm} \end{cases} \tag{4.8}$$

The rate of change in raindrop number concentration from self collection ($\left|\frac{\partial N_T}{\partial t}\right|_{SC}$) depends on the existing number and mass of raindrops (N_T and Q), and on the collection efficiency (ξ_r), which varies with drop size (median volume diameter, $\mathrm{mvd_r}$) as shown in Fig. 4.5. For drops larger than about 2 mm ξ_r is negative, corresponding to drop breakup and an increase in number concentration, since $\left|\frac{\partial N_T}{\partial t}\right|_{SC}$ appears as a negative term in the raindrop number tendency equation. Drop breakup in the Thompson scheme has since been relaxed partly as a result of this work, by lowering the pre-factor in the self collection equation from 4 to 0.5, in order to allow drop size to increase further with intensity (G. Thompson, 2013).

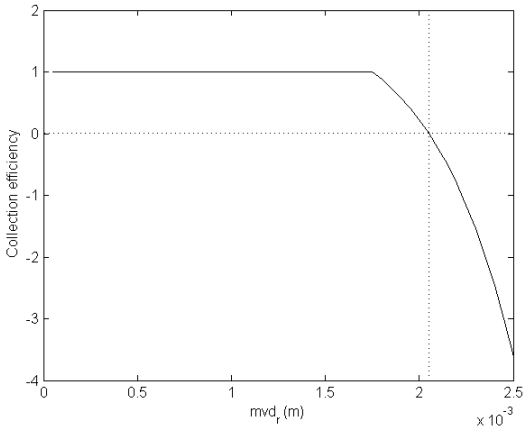

Figure 4.5: Dependence of raindrop collection efficiency, ξ_r, on drop median volume diameter, $\mathrm{mv}d_r$, in the Thompson scheme. A negative collection efficiency causes raindrop breakup and an increase in the number of drops.

4.3.3 Importance of raindrop velocity

For any variable X, the flux at the surface is equal to the product of X and its rate of arrival at the surface (the fall speed of raindrops). Rainwater mass flux (surface precipitation rate) therefore depends linearly on fall speed (equation 2.11). Kinetic energy, however, itself varies with the square of velocity, so its flux has a cubic dependence on speed (equation 4.2). Consequently, an accurate representation of the fall speed of larger drops becomes crucially important when kinetic energy flux is considered.

Several relations between terminal velocity and drop size, $V(D)$, have been proposed in the literature (sec. 1.2.4). Those assumed in the microphysics schemes tested here are compared with observations from *Gunn and Kinzer* [1949], whose results agree well with measurements in other studies, in Fig. 4.6. Evidently, some $V(D)$ equations have emphasized a good fit for smaller drop sizes at the expense of larger drops. Only the Thompson scheme avoids this problem. In general, $V(D)$ relationships which include an exponential term (e.g. *Atlas et al.* [1973]; *Uplinger* [1981], used in the Thompson scheme) can account for the saturation of the velocity curve as the drag increases on larger, more oblate, drops. Power law expressions (e.g. *Atlas and Ulbrich* [1977]; *Liu and Orville* [1969], used in both Morrison and WDM6) have no upper limit for velocity and result in large overestimations of fall speed for heavier drops. *Atlas et al.* [1973] and *Van Dijk et al.* [2002] made this same observation.

The importance of larger drops is illustrated by the schematic in Fig. 4.7. This shows the mean drop size distribution at the surface and the resulting mass and kinetic energy flux distributions with size for the Morrison scheme (results were similar for all schemes). The peaks of the curves occur at progressively greater sizes: larger drops contribute disproportionately to the total mass and kinetic energy flux relative to their size. Raindrops larger than 3 mm constitute only 0.4% of the total number of drops but contribute 32% to the mass and 52% to the kinetic energy flux on average across all schemes. These numbers include the bias resulting from the use of straight power law $V(D)$ relations in the MY, Morrison, and WDM6 schemes. Despite this, large drops still contribute significantly to total mass (27%) and kinetic energy flux (40%) on average in both the Thompson runs, which use a more appropriate $V(D)$ fit. It is also worth noting the significance of larger drops for mass flux and therefore for surface precipitation, suggesting that these drops may be more important for the development of microphysics schemes than has previously been supposed.

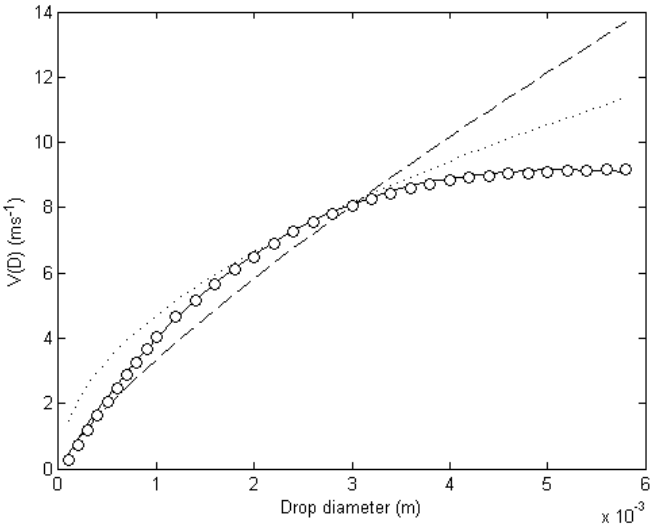

Figure 4.6: Comparison between terminal velocity expressions, $V(D)$, used in the Thompson (solid line), MY (dotted line), Morrison and WDM6 (dashed line for both) schemes, and measurements from *Gunn and Kinzer* [1949] (circles).

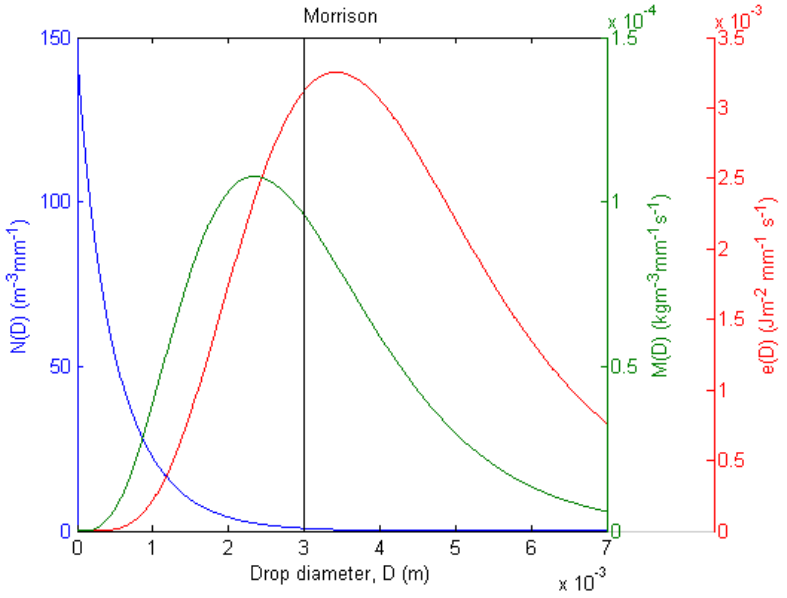

Figure 4.7: Schematic showing mean drop number density, $N(D)$, mass flux, $M(D)$, and kinetic energy flux, $E(D)$ as functions of drop size for the WDM6 scheme. Averages were taken across the whole domain. The $V(D)$ curves in Fig. 4.6 diverge from about 3 mm, represented by the black vertical line .

This raises a question regarding the data comparison presented in Fig. 4.1. Calculations of rainfall kinetic energy are rarely based upon direct, simultaneous observations of drop size distributions and drop fall velocities. Instead, drop size distributions are measured at the ground, and a fall velocity relationship is assumed in order to compute the kinetic energy. Drop size distribution measurements taken using impact disdrometers (e.g. the commonly used Joss-Waldvogel disdrometer [*Joss and Waldvogel*, 1967]) also assume that fall speeds follow observations by *Gunn and Kinzer* [1949]. Therefore, the 'observed' kinetic energy-intensity curves from *Salles et al.* [2002] (Fig. 4.1) implicitly include any errors resulting from the $V(D)$ relation assumed in each case.

To test the effect of this hidden error, the energy-intensity parameterisations taken from *Salles et al.* [2002] were classified into two categories according to the $V(D)$ expression used for the measurements in each case: those with power law forms, and those without. The results of this are shown in Fig. 4.8. Fall speed assumptions can only account for part of the difference between parameterisations; differences in drop size distribution between the various measurement sites and in the methods used to fit the curve will also play a part. The spread in kinetic energy-intensity curves based on power law velocity relations is slightly greater than for those which use other $V(D)$ relations. The most significant difference in the mean parameterisation of each group is at low rain intensities (less than $3\,\mathrm{mmhr}^{-1}$), where those which assume a power law relation have higher energies for a given intensity. Given that the power law velocity only deviates significantly from observations for large drops (Fig. 4.6), and drop size increases with intensity, it is unlikely that the $V(D)$ expressions are responsible for this deviation. For most intensities, the difference is minimal and may be neglected.

To test to what extent the fall speed expressions were responsible for differences in simulated kinetic energy flux between the schemes, $V(D)$ equations used in the Morrison, WDM6 and MY schemes were implemented into the Thompson scheme (Fig. 4.9). Results from Thompson-0 using the same fall speed relation as Morrison and WDM6 (which use the same $V(D)$ as each other) are closer to, but not the same as, the original Morrison results. The adapted Thompson-0 scheme produces energies closer to the original WDM6 simulation at intensities greater than about $40\,\mathrm{mmhr}^{-1}$, and further from the WDM6 results below this (Fig. 4.9a). Using the MY $V(D)$ equation in the Thompson scheme accounts for a large part of the difference between Thompson-0 and MY-0 runs below about $10\,\mathrm{mmhr}^{-1}$, but not

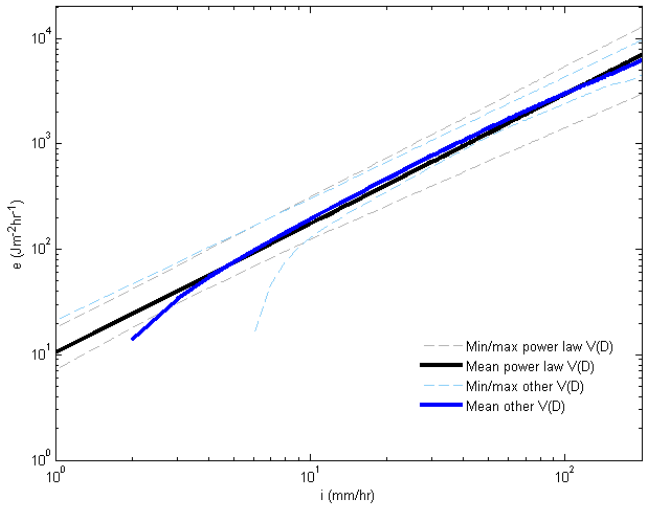

Figure 4.8: Rainfall kinetic energy flux-intensity parameterisations from *Salles et al.* [2002], divided into two categories: those which assume a power law $V(D)$ expression (black solid line and grey dashed lines) and those which do not (blue solid line and light blue dashed lines). In each case the solid line shows the average energy flux-intensity relationship and the dashed lines give the minimum/maximum energy flux for a given intensity.

at higher intensities (Fig. 4.9b). Different $V(D)$ assumptions therefore account for some, but not all, of the differences in kinetic energy flux simulated by the schemes.

4.3.4 Limitations

The conclusion that large drops contribute substantially to kinetic energy flux rests upon the DSD providing a good fit for larger drop sizes. Exponential DSDs tend to overestimate the number of small and large raindrops [*Willis*, 1984; *Torres et al.*, 1994], and so may artificially inflate the importance of the high end of the spectrum. However, the model simulations performed here used both gamma and exponential DSDs, and the evidence that large drops contribute significantly to kinetic energy and mass flux is robust across all schemes.

The success of this method will depend on the ability of regional climate models to produce realistic precipitation rates and raindrop size distributions. Differences between microphysics schemes (e.g. the number of moments, treatment of drop breakup and ice phase microphysics) may influence these factors. Model deficiencies and development will therefore have important consequences for rainfall energy flux

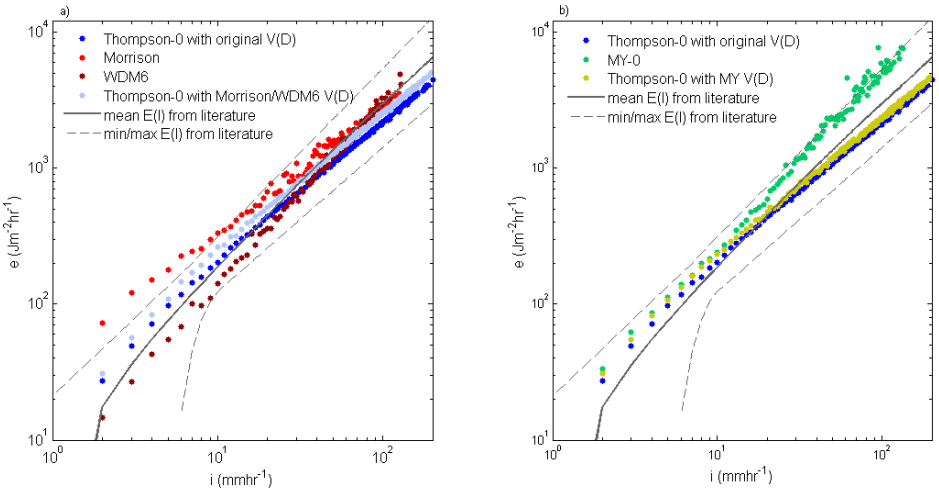

Figure 4.9: Modelled kinetic energy flux-intensity relationships obtained as a result of the $V(D)$ experiment using the Thompson scheme. a) shows results for the unaltered Thompson-0 (dark blue), Morrison (red) and WDM6 (dark red) schemes, and results for Thompson-0 using the Morrison/WDM6 $V(D)$ expression (light blue). The light blue data points are closer to both the Morrison and WDM6 data at higher intensities. b) gives results for the unaltered Thompson-0 (dark blue) and MY-0 (green) schemes, and results for Thompson-0 using the MY $V(D)$ expression (yellow). The yellow data lie between the original Thompson and MY-0 results.

simulations. However, this analysis shows that for a given precipitation intensity, modelled kinetic energy fluxes are within the range of observations.

Some error will also be introduced by the sphericity approximation for raindrops, which holds less well for large drops as oblateness increases with size. It is assumed that drops fall at their terminal velocity, but some studies suggest that deviations from terminal speed may be significant [*Van Dijk et al.*, 2002; *Montero-Martinez et al.*, 2009]. No attempt has been made to account for raindrop kinetic energy dissipated through heating on impact with the ground, which is not available for soil detachment. If the fraction of total kinetic energy lost in this way varies with raindrop size, this would affect the slope of the 'available' kinetic energy-intensity curve. These errors may be partly responsible for the differences found between the model results and observed data, but as the model data is for an idealised storm this comparison is already limited and more specific conclusions are difficult. A full model simulation of a real storm for which kinetic energy flux observations are available for comparison would be needed in order to reduce the uncertainties further.

Horizontal wind can cause raindrops to arrive at the surface at an angle, and no consideration of the effects of this on their kinetic energy flux is attempted here. The model dynamics implicitly affect the rate at which particles fall by advecting them in the direction of the wind velocity, but when drops impact the surface they are still assumed to do so according to their assumed $V(D)$ relation. *Pedersen and Hasholt* [1995] showed that the true kinetic energy of raindrops on impact with the ground is a function of the vertical, $w(D)$, and horizontal, $u(D)$, components of drop velocity: $k(D) = \frac{1}{2}M(D)\left[w(D) + u(D)\right]^2$. They proposed a kinetic energy-intensity parameterisation which includes the effect of horizontal wind, of the form $\alpha(v)\ln(I) + \beta(v)$, where α and β are increasing functions of the horizontal wind speed, v, and showed that this increases the drop energy upon impact. However, the consequences of this for soil detachment were not straightforward, as they depended on the ground slope aspect to the wind. EI30 erosivity indices increased using the new parameterisation, but this did not improve the correlation between erosivity and soil loss.

4.4 Conclusions

The work presented in this chapter demonstrates, for the first time, that it is possible to dynamically simulate the kinetic energy flux of rainfall with a cloud resolving model, using a range of microphysics options. Results are mainly within the range of observations reported in the literature. The model broadly captures the observed variability reported in other studies, which results from variations in drop size distribution for a given intensity. The standard method of parameterising kinetic energy from intensity ignores this variability. In addition, emphasis has been placed on obtaining good fits at high intensities for these parameterisations, which can result in unrealistic results for light rain. This is avoided by the proposed method.

These findings suggest that it is important to use a $V(D)$ relation which fits the full range of drop sizes well, especially for kinetic energy flux, but also for surface rainfall. Several commonly used power law relations overestimate larger drop speeds.

Each scheme revealed strengths and weaknesses in different areas. In all simulations, the energy flux-intensity relationship was reasonable, but the Morrison and MY-0 options produced higher energies at low and high intensities, respectively. WDM6 and Morrison exhibited too much variability in energy compared with the observations of SS00. Thompson-0, Thompson-1 and Morrison do not capture the observed increase in raindrop size for higher intensities, compensating for this with a rise in drop number concentration. In the Thompson scheme this is because of an overactive drop breakup parameterisation, which has since been adjusted for the next WRF release. Only the Thompson scheme uses a velocity-drop size relation that accounts for the saturation of speed as drop size increases.

The method proposed in this study may easily be extended for use in a full regional climate model. This could be used to provide high temporal and spatial resolution data to force erosion models. However, direct observations would be needed for verification in real data case studies. There is usually little or no microphysics treatment in cumulus parameterisation schemes, so the kinetic energy flux of rain from the cumulus scheme cannot be computed. Because of this, convection resolving scales are required so that all modelled precipitation is produced by the microphysics scheme. This has recently been achieved in a 10 year simulation [*Kendon et al.*, 2012]. As computing power improves, climate and climate change simulations of rainfall kinetic energy flux will become possible. This will allow projections of rainfall energy that may be useful for erosion prediction and management.

5 The impact of aerosols on rainfall erosivity

5.1 Introduction

No connection has hitherto been drawn between aerosols and soil erosion. The purpose of this chapter is to demonstrate the effect of increased aerosol loading on rainfall erosivity in two idealised case studies. It is generally accepted that storms are responsible for the dominant share of erosion [*Wischmeier and Smith*, 1978; *Boardman*, 2006]. However, evidence suggests that light rainfall can also cause substantial erosion over long time scales [*Kirkbride and Reeves*, 1993; *Baartman et al.*, 2012; *Marques et al.*, 2008]. Both cases are explored in this study.

Understanding the effects of aerosols on precipitation processes remains challenging, depending on a complex balance of microphysical and dynamic effects. These may be simplified by classification into two broad categories which we study here. Smaller cloud droplets in a polluted atmosphere inhibit the collision and coalescence processes that lead to raindrop formation, and may suppress surface rainfall. In warm rain clouds this outcome usually prevails. Conversely, in a mixed phase system, these smaller droplets, which are prevented from forming raindrops owing to their reduced size, survive longer in the cloud, may be lifted to freezing level and serve to invigorate cold-rain formation processes ('aerosol invigoration effect'). The associated latent heat release can invigorate convection, resulting in a delayed enhancement of surface rainfall under certain environmental conditions (see sec. 1.2.5 for a more detailed discussion).

The case studies in this chapter were chosen to illustrate the two categories of behaviour described above. A two-dimensional moist flow over a bell-shaped hill with gentle orographic precipitation provides the warm-rain example, where microphysical effects cause a decrease in precipitation with increasing aerosol concentrations. A

stationary supercell case study characterises the response of a mixed-phase cloud, in which the aerosol invigoration effect dominates, resulting in a positive precipitation sensitivity overall.

5.2 Methods

A cloud resolving version of WRF version 3.1 was used to simulate the two idealised case studies. This model is similar to that described in chapter 4 except that sub-grid cloud processes are parameterised using an updated version of the standard microphysics scheme by *Morrison et al.* [2009] (Morrison). The scheme has been adapted to include a prognostic treatment of cloud droplet number concentration and is described in detail in sec. 2.4.4.

The results presented in chapter 4 suggest that the Thompson scheme would be preferable because it uses a raindrop terminal velocity relation which agrees best with observations. Kinetic energy flux simulated in the Thompson scheme also agrees more closely with the observed range of kinetic energy-intensity parameterisations (Fig. 4.1) and the variability is more similar to observations (Fig. 4.3). However, all the schemes tested in chapter 4 were relatively successful at simulating rainfall kinetic energy flux. The Morrison scheme was chosen because of its ability to prognose cloud droplet number concentration. This was considered a major advantage for an aerosol study. WDM6, which prognoses both CCN and cloud droplet number concentration, was avoided because it does not account for the inability of the model to resolve the supersaturation field when nucleating cloud droplets (sec. 2.4.4). In addition, excessive size sorting is better controlled in Morrison than in WDM6. Milbrandt-Yau has a switch to activate cloud droplet number prediction, but background CCN number concentration cannot be freely varied as in the updated Morrison scheme.

The empirical parameters k and c from the assumed power law CCN distribution: $N_{CCN} = cs^k$ (equation 1.7) are user defined in this version of the Morrison scheme. k was fixed at 0.308 while c was varied to change the background aerosol loading from 300 to 1200 cm^{-3}. These values are consistent with other studies [*Khain et al.*, 2005; *Fan et al.*, 2012] and with observations [*Pruppacher and Klett*, 1997].

Erosivity was computed according to the QE index proposed by *Kinnell et al.* [1994] (equation 1.28). Surface runoff is a fraction of intensity and to enable a simple

calculation of erosivity (equation 1.28) in an idealised model with no land surface scheme we assume that this fraction, k, is constant:

$$R = \sum_t e_t i_t k (\triangle t)^2 \tag{5.1}$$

In equation 5.1, e_t is the rainfall kinetic energy flux ($\mathrm{Jm^{-2}hr^{-1}}$) and i_t is the intensity ($\mathrm{mmhr^{-1}}$) at time t of rain falling over a period $\triangle t$ of 10 minutes.

Kinetic energy flux is modelled within the bulk microphysics scheme based on the method described in chapter 4. Incorporating a consideration of drop size is important because large raindrops contribute disproportionately to kinetic energy flux compared with their number (chapter 4), so changes in drop size will affect the erosivity term.

For comparison, the USLE and RUSLE erosivity terms, R_U and R_R, are also computed, using the EI30 formulation (equation 1.27), with energy flux calculated using equation 1.31 and both USLE (equation 1.29) and RUSLE (equation 1.30) kinetic energy-intensity parameterisations:

$$R_{R,U} = I_{30} \sum_t e_t (\triangle t) \tag{5.2}$$

5.3 Mixed-phase cloud case study: stationary supercell storm

Case study setup

The stationary supercell storm was initiated with a temperature perturbation of 3 K in the centre of the domain, 1.5 km above the ground. The perturbation had a 10 km horizontal and 1.5 km vertical radius and approached zero at the domain boundaries. Soundings from *Weisman and Klemp* [1982] were used for the initial profiles of potential temperature and water vapour mixing ratio. Water vapour was increased by 7% throughout the column from this sounding. The domain was 42 km x 42 km with a horizontal resolution of 1 km and 61 vertical levels between the ground and model top at 20 km. Total run time was 4 hours with a time step of 6 s. Background CCN concentrations (c in equation 1.7) were increased from 300

to 1200 cm^{-3}. All boundaries were open, and model variables were extracted every 10 minutes.

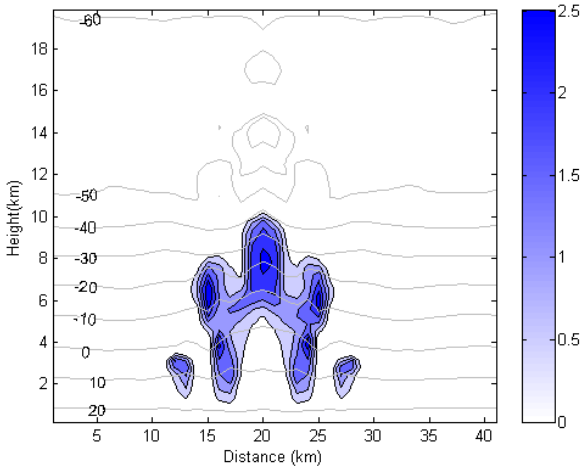

Figure 5.1: Cross section showing cloud water mass mixing ratio (g/kg) after 30 minutes in the base CCN simulation (300 cm^{-3}) for the stationary supercell case study. Isotherms are shown by the grey contours (°C).

Results

The temperature perturbation triggered a convective storm, which delivered an average of 25.7 mm rain per rainy grid at a rate of 8.20 $mmhr^{-1}$ for the 300 $CCNcm^{-3}$ scenario. The cloud extended above the freezing level (Fig. 5.1). Total accumulated rainfall increased between 300 and 700 CCN cm^{-3} (Fig. 5.2). In the following, results are presented for the CCN range which exhibits an aerosol invigoration effect on surface precipitation; 'clean' and 'polluted' conditions refer to these lower and upper limits (300 and 700 CCN cm^{-3}, respectively). For this range, total rainfall increased by 25% on average in each rainy grid, and mean rain intensity over rainy time steps increased by 23% across the whole domain. The middle of the intensity distribution increased most, with a slight decrease in the upper quantiles of rain intensity (Fig. 5.3). A saturation effect above 700 CCN cm^{-3} could be explained by limited moisture availability, and/or by the dominance of condensation loss processes, such as increased detrainment of smaller (lighter) cloud ice particles which dries the upper cloud levels and enhances evaporation and sublimation in more polluted environments [*Rosenfeld and Woodley*, 2000]. However, the diagnostics needed to justify this argument (e.g. latent heating) were not available from the model output.

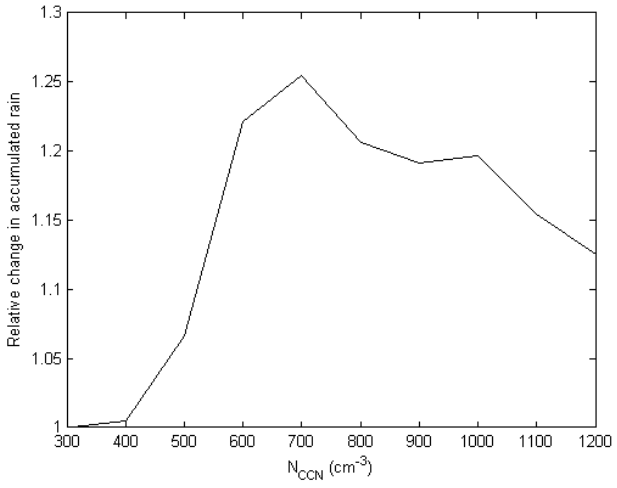

Figure 5.2: Relative change in accumulated rainfall with CCN loading for the static supercell case study.

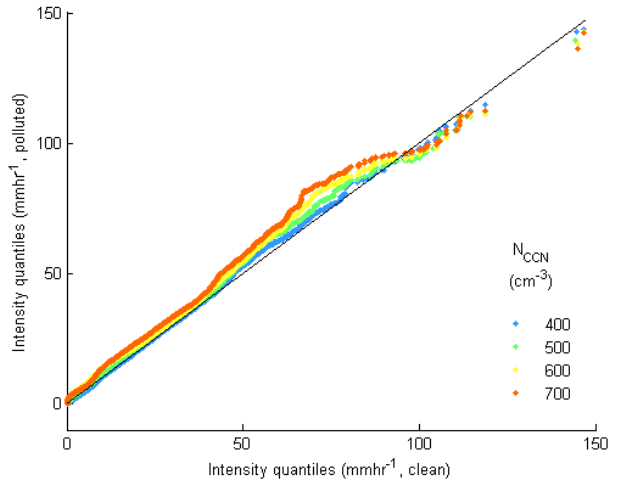

Figure 5.3: Comparison between quantiles of the rain intensity distributions in the base and increased aerosol simulations for the supercell case study. Deviations above (below) the black solid line ($x = y$) represent increases (decreases) in the quantiles of the intensity distribution in each of the elevated CCN loadings compared with the clean case.

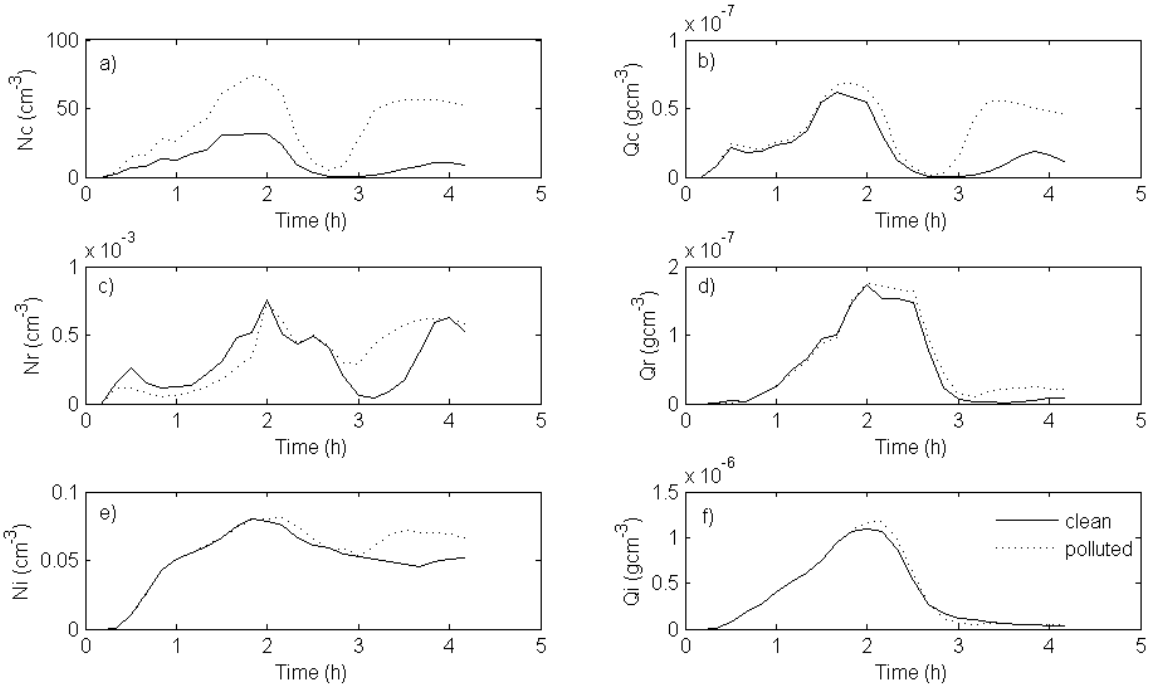

Figure 5.4: Time series of mean number concentration (cm^{-3}) of (a) cloud droplets, (c) raindrops and (e) ice particles (cloud ice + snow + graupel) and of mean mass (gcm^{-3}) of (b) cloud water, (d) rainwater and (f) ice. Averages were taken across the whole domain for all time steps. Results are shown for the clean (solid line, 300 CCN cm^{-3}) and polluted (dotted line, 700 CCN cm^{-3}) conditions.

The mean cloud droplet concentration, N_c, ranged from about 200 to 740 cm^{-3} in cloudy regions (positive cloud water mixing ratio, Q_c) for the 900 cm^{-3} increase in CCN concentration. Fig. 5.4 shows the microphysical changes occurring within the cloud. N_c is substantially higher (+233%) in the polluted scenario, while cloud water mixing ratio, Q_c, increases less (+73%). The number concentration of ice particles (cloud ice + snow + graupel), N_i, increases by 12%, while ice mass mixing ratio, Q_i increases by 2%. The effect of this invigoration on rain is seen in the second half of the simulation, with increases in raindrop number concentration and mass mixing ratio of rain, N_r and Q_r, of +12% and +15%, respectively. The onset of surface precipitation is delayed by 10 minutes and persists for longer in the polluted case, with higher precipitation rates from about 2 hours into the simulation and a higher peak precipitation rate (Fig. 5.5). The net result of these changes is a 7% increase in total water content, consisting of a substantial increase in liquid (+31%) and a modest rise in ice water content (+2%; Fig. 5.6). Updraft velocity increases by 2%

(averaged over values of vertical wind speed greater than 2 ms^{-1}), particularly in the upper cloud levels (Fig. 5.7).

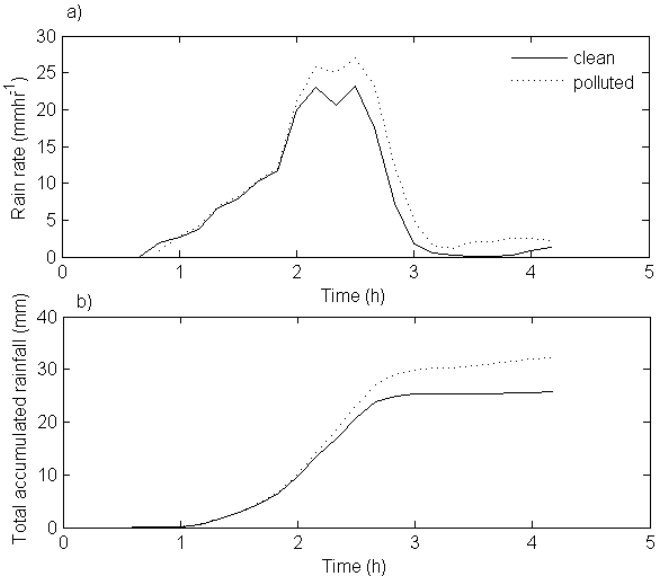

Figure 5.5: a) Domain-mean rain rate ($mmhr^{-1}$) for rainy time steps only and b) domain total accumulated rainfall (mm) for the clean (solid line) and polluted (dotted line) cases.

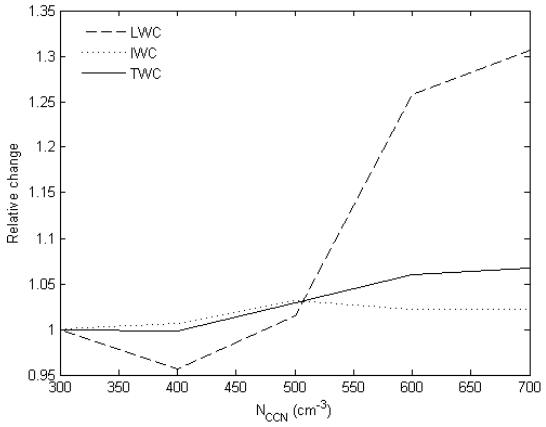

Figure 5.6: Relative change in mean liquid (LWC), ice (IWC) and total water content (TWC) with CCN concentration (cm^{-3}) for the supercell case study. Averages were taken across space and time, over positive values only. For 300 CCN cm^{-3} average LWC was 1.78 gm^{-3}, IWC was 9.44 gm^{-3} and TWC was 11.2 gm^{-3}.

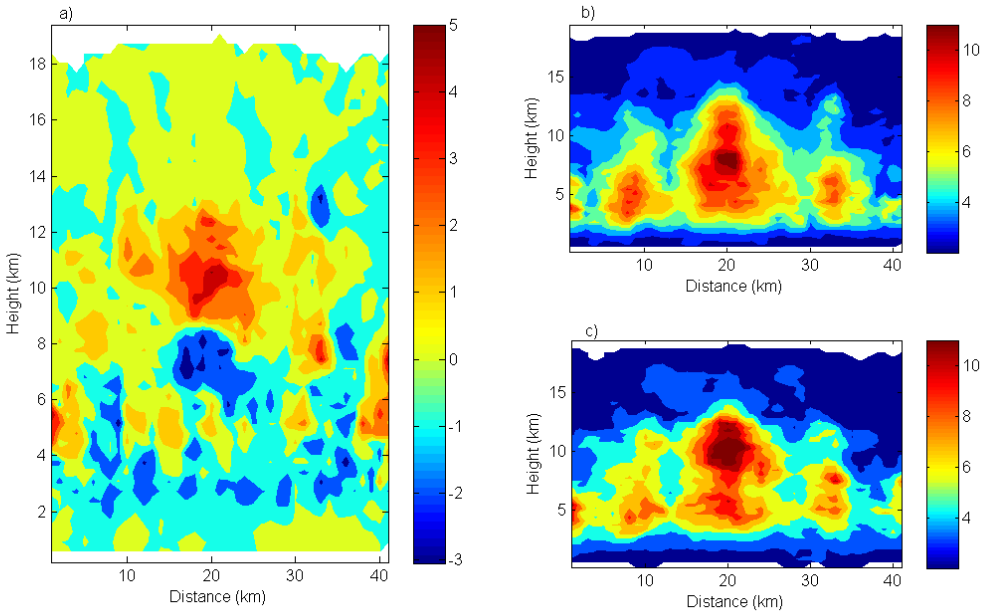

Figure 5.7: Vertical cross sections of time-mean updraft velocity (ms^{-1}), taken through the centre of the domain in the longitudinal direction: a) change in updraft velocity between clean and polluted simulations, b) updraft speed in the clean and c) polluted simulations. Updraft velocity is defined by values of vertical wind speed greater than 2 ms^{-1}, according to *Fan et al.* [2012].

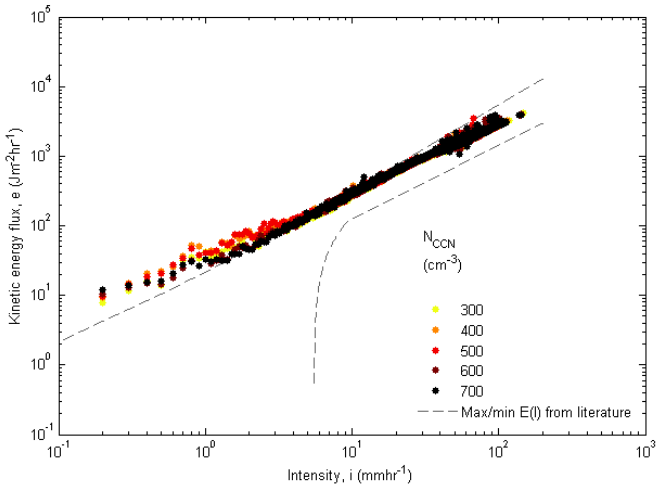

Figure 5.8: Modelled kinetic energy flux-intensity relationship for the supercell case study. Kinetic energy flux, e, was modelled using equation 4.3. Values plotted are mean energy fluxes across the domain for each intensity bin, and are not sensitive to bin size. The upper/lower range of observed kinetic energy-intensity relationships reported in the literature are also shown (grey dashed lines, *Salles et al.* [2002]).

Rainfall kinetic energy flux, e, modelled within the microphysics scheme according to equation 4.3, is shown as a function of intensity for the static supercell case in Fig. 5.8. As for the moving supercell storm in chapter 4, the modelled relationship is approximately linear and falls mainly within the range of observed relationships reported in the literature [*Salles et al.*, 2002], except at low rainfall intensities.

Fig. 5.9 presents the relative change in accumulated rainfall (I), kinetic energy (E), and domain total erosivities R and R_R with increased aerosol loading. For 300 to 700 CCN cm^{-3} a clear invigoration signal is seen, and total rainfall and kinetic energy rise by +25% and +29%, respectively. Domain total erosivity (R) increases by +36%, greater than the change in either total rainfall or kinetic energy. For comparison, the domain total RUSLE erosivity (R_R) is calculated, and is similarly amplified relative to the change in total rainfall (+37%). The USLE erosivity (R_U) also shows an amplification (+37%, not shown). For further verification, erosivity according to the EI30 formulation (equation 5.2) was computed using the energy flux modelled within the microphysics scheme. This again showed an amplification beyond the change in total rainfall (+41%). This gives confidence that the signal is robust across different commonly used measures of erosivity and kinetic energy calculations.

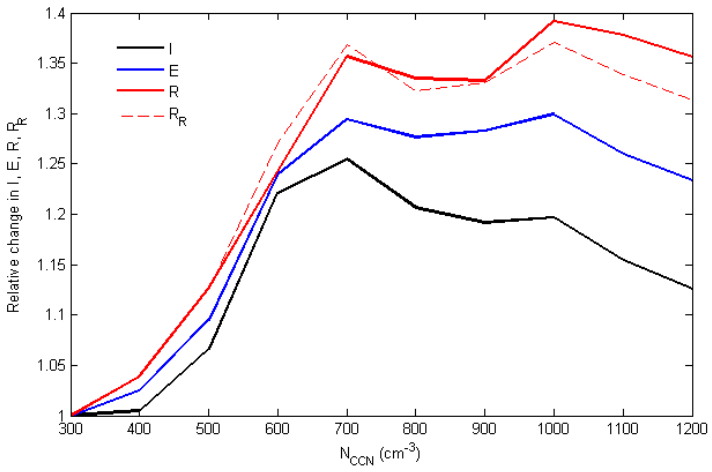

Figure 5.9: Relative change from the base case aerosol loading of domain-mean accumulated rainfall (I) and modelled kinetic energy (E), and domain total erosivity (R) and RUSLE erosivity (R_R) for the supercell case study. For the base supercell simulation (N_{CCN}=300 cm^{-3}), I=25.7 mm, E=765 Jm^{-2}, $R = 6.35 \times 10^9$ Jm^{-1} and $R_R = 3.65 \times 10^{10}$ Jm^{-1}hr^{-1}. Averages (for I and E) were taken over grids with positive values only.

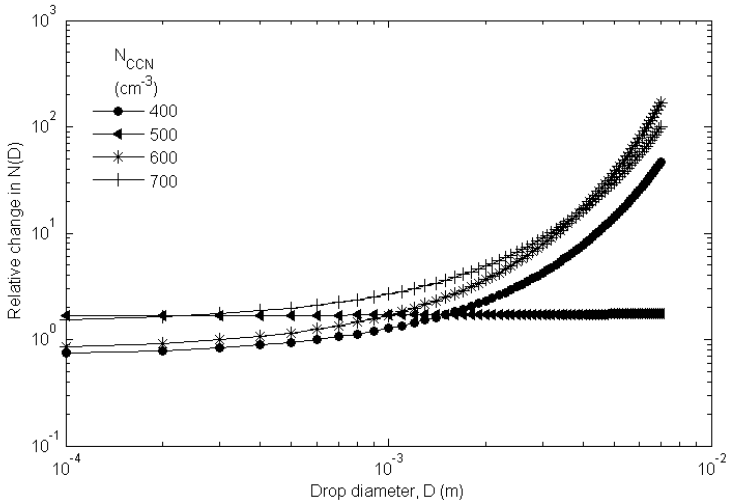

Figure 5.10: Ratio of mean raindrop size distribution at the surface for each aerosol loading to the base CCN level in the stationary supercell case. A value of 10^0 on the y-axis means no change from the base CCN simulation. $N(D)$ was calculated using the mean raindrop number concentration, N_r, and slope parameter, λ_r, for each simulation. The clean scenario (300 CCN cm^{-3}) had an average of 1537 drops m^{-3} distributed with a slope parameter of 2878 m^{-1}. Averages were taken over time and space, for rainy time steps only.

Raindrops are larger in the polluted scenario; mean drop diameter increases by 27% between 300 and 700 $\mathrm{CCNcm^{-3}}$. Fig. 5.10 illustrates the relative change in DSD for each aerosol loading compared with the base CCN level ($300\,\mathrm{cm^{-3}}$). As aerosol loading increases, there is a disproportionate increase in the number of large raindrops, resulting in an overall rise in the mean drop size. However, this change is not monotonic, with a greater rise in the number of large drops for 600 $\mathrm{CCNcm^{-3}}$ than for 700 $\mathrm{CCNcm^{-3}}$, relative to the base CCN case. In the 500 $\mathrm{CCNcm^{-3}}$ case, there are more raindrops of all sizes, with no disproportionate change in the number of larger drops. Overall, the DSD widens with increasing intensity, leading to an increase in average drop size. However, some variability in the DSD for a given intensity of rain is also expected (see chapter 4).

5.4 Warm cloud case study: orographic precipitation

Case study setup

For the hill case, tropical profiles of potential temperature and water vapour were used [*Anderson et al.*, 1986] and a constant westerly wind velocity of $10\,\mathrm{ms^{-1}}$ was applied. Simulations using tropical profiles were chosen as these delivered more rain and higher erosivity values, and therefore provided a more suitable erosion case study than the mid-latitude alternatives. The two-dimensional hill followed a simple bell shape, 2 km high with a half width of 30 km. The domain had 201 grids of 2 km horizontal resolution in the west-east direction, and 41 vertical levels between the ground and model top at 30 km. A 20 s model time step was used, and the model was run for 10 hours. x-boundaries were open and y-boundaries were periodic to force the 2D simulation to be uniform in the y-direction. Model variables were extracted every 10 minutes. 'Clean' and 'polluted' conditions in this section refer to the lowest and highest CCN concentrations for this case study (300 and $1200\,\mathrm{cm^{-3}}$, respectively).

Results

Moist air, forced to rise over the hill by the constant wind forcing, condensed to form a cloud (Fig. 5.11). Unlike in the supercell case, the cloud remained below freezing

level at all times, and delivered an average of 1.2 mm rain in each rainy grid at a rate of 0.18 mmhr^{-1} for the base CCN concentration. Increased CCN loading reduced the total rainfall, with a 72% average reduction in total rain per rainy grid, and a 70% reduction in mean rain intensity between the clean and polluted simulations. The intensity distributions are compared in Fig. 5.12, which indicates a disproportionate decrease in the most extreme rainfall.

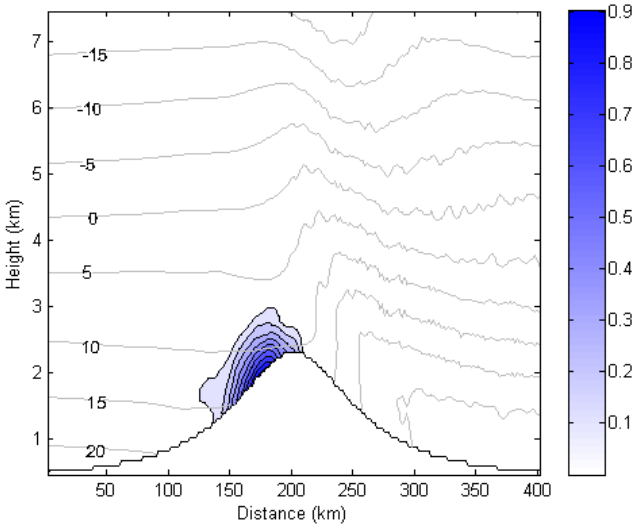

Figure 5.11: Cross section showing cloud water mass mixing ratio (gkg^{-1}) after 10 hours in the base CCN simulation (300 cm^{-3}) for the hill case study. Isotherms are also shown (grey contours, °C).

Background CCN concentrations from 300 to 1200 cm^{-3} delivered mean cloud droplet concentrations of approximately 130 to 450 cm^{-3} in cloudy regions ($Q_c > 0$). Cloud droplet number and mass respond similarly to increased aerosol loading as in the supercell case (Fig. 5.13). Cloud droplet concentration, N_c, increases substantially with aerosol (+257%), while cloud water mass, Q_c, also increases but by a lesser amount (+27%). The number concentration of raindrops, N_r, and the mass of rain, Q_r, decrease by 78% and 81%, respectively.

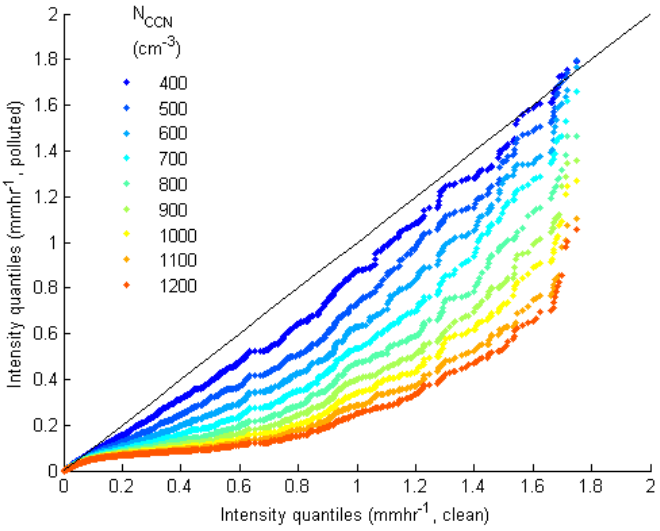

Figure 5.12: As for Fig. 5.3, for the hill case study.

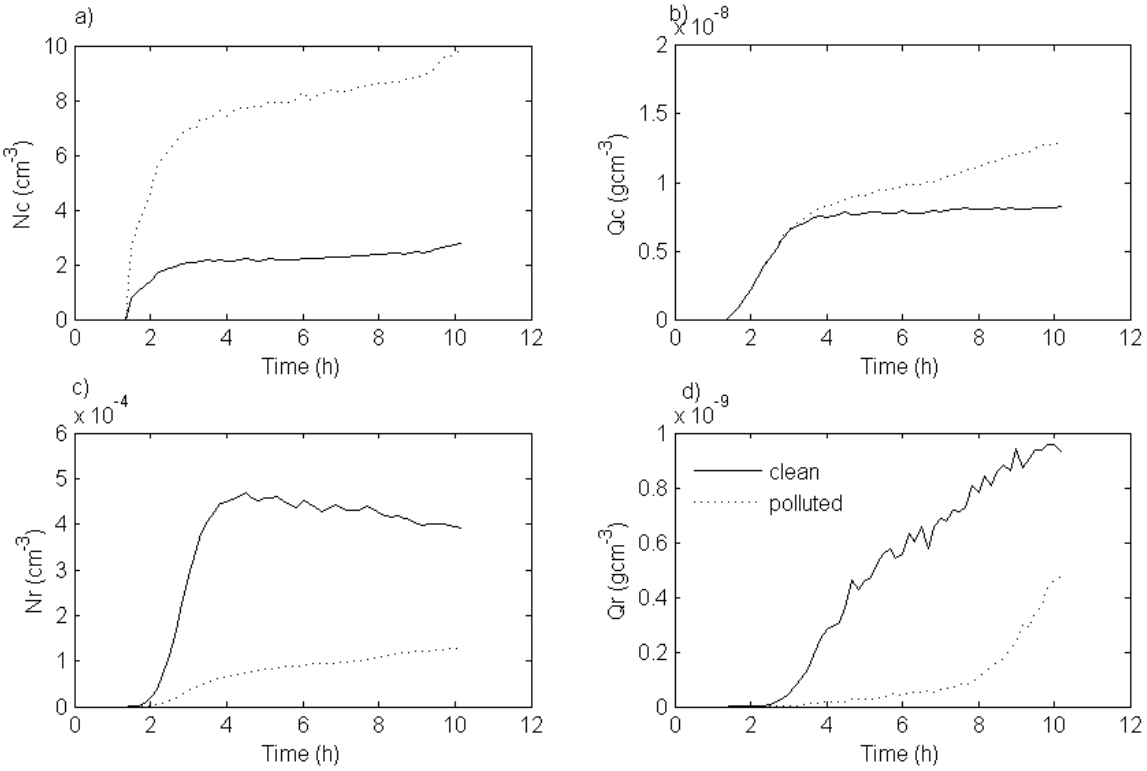

Figure 5.13: Time series of mean number concentration (cm^{-3}) of a) cloud droplets and c) raindrops, and mean mass (gcm^{-3}) of b) cloud and d) rainwater . Results are shown for the clean (solid line) and polluted (dotted line) conditions. Averages were taken across the whole domain over all time steps.

The rainfall kinetic energy flux modelled according to equation 4.3 is shown in Fig. 5.14, with results for the supercell included for comparison. Results are within the range of observed kinetic energy-intensity relationships reported in the literature [*Salles et al.*, 2002]. Kinetic energy flux for a given intensity of rain is higher in the supercell case. In the hill case, energy flux for a given intensity increases with aerosol loading. These points are discussed in further detail in the following section.

Fig. 5.15 shows the relative change in accumulated rainfall, kinetic energy and domain total erosivity. For an increase of 900 CCN cm^{-3}, total precipitation is suppressed by 71% and energy by 80%. Domain total erosivity (R) falls by 90%, while RUSLE (R_R) and USLE (R_U, not shown) erosivities decrease by 89% and 93%, respectively. Erosivity calculated using the EI30 formulation (equation 5.2), computed using the energy flux modelled within the microphysics scheme (equation 4.3), decreased by 90%. In both the hill and supercell case studies therefore, the change in erosivity exceeds the change in total rainfall, using a range of erosivity formulations and energy calculations.

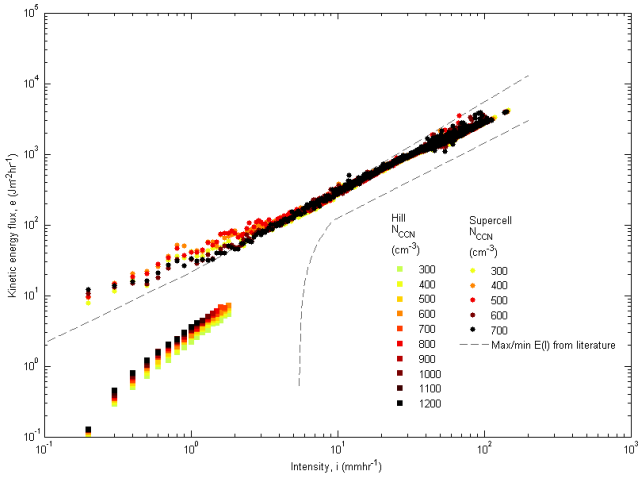

Figure 5.14: Modelled kinetic energy flux-intensity relationship, for the hill (squares) and supercell (circles) cases. Values plotted are mean energy fluxes across the domain for each intensity bin, and are not sensitive to bin size. The upper/lower range of observed kinetic energy-intensity relationships reported in the literature are also shown (grey dashed lines, [*Salles et al.*, 2002]).

In contrast to the supercell, average raindrop size decreases in the hill case: mean drop diameter is reduced by 24%. The overall change in DSD is illustrated by Fig. 5.16a, which shows the mean DSD relative to the base CCN loading (300 cm^{-3}).

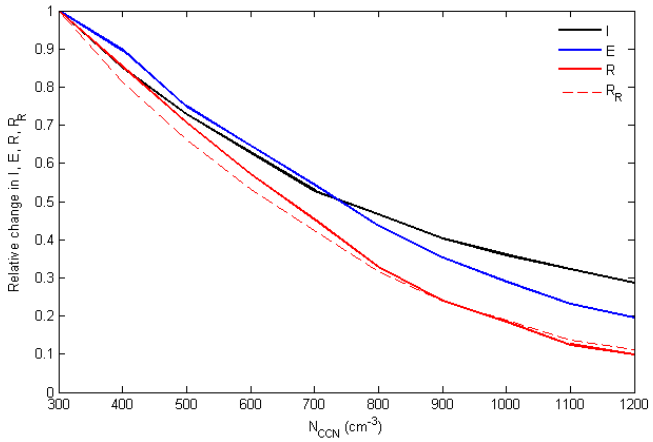

Figure 5.15: Relative change from the base case aerosol loading of domain-mean accumulated rainfall (I) and modelled kinetic energy (E), and domain total erosivity (R) and RUSLE erosivity (R_R) for the hill case study. For the base hill simulation (N_{CCN}=300cm^{-3}), I= 1.15 mm, E=2.21 Jm^{-2}, R=8.83 x 10^4 Jm^{-1} and R_R=2.88 x 10^6 Jmhr^{-1}. Averages (for I and E) were taken over grids with positive values only.

There are fewer raindrops of all sizes (downward shift in relative DSD), but a disproportionate decrease in the number of large drops, leading to an overall reduction in raindrop size. Fig. 5.16b shows the mean DSDs in the 0.2 mmhr^{-1} intensity bin for each CCN loading relative to the base CCN case, and is representative of other intensity bins. As CCN increases, rain of a given intensity consists of fewer small drops and more large drops, shown by a cross-over in the relative size distributions at about 0.4 mm in Fig. 5.16b. Rainfall of a given intensity therefore consists of larger drops under higher CCN concentrations.

5.5 Discussion

5.5.1 Case studies

In both case studies, the relative increase in the number of cloud droplets exceeds the increase in cloud water mass, indicating that droplets are smaller under more polluted conditions (Fig. 5.4, Fig. 5.13). This is expected according to *Twomey* [1977] (sec. 1.2.5). In the hill case, this reduces the number of raindrops, N_r (-78%), and the mass of rain, Q_r (-81%), as autoconversion from cloud to rainwater is

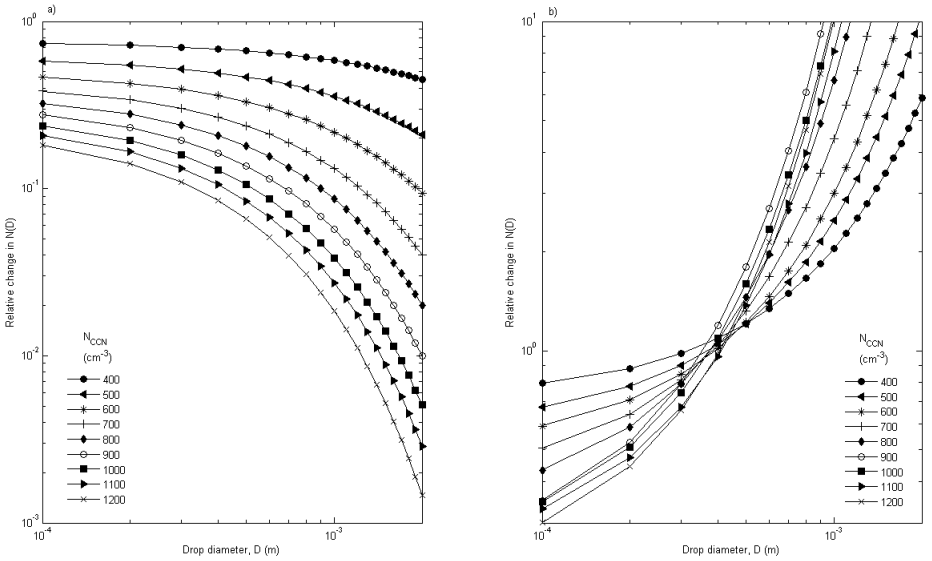

Figure 5.16: Ratio of mean raindrop size distribution at the surface for each aerosol loading to the base CCN level in the hill case. The size distribution, $N(D) = N_r\lambda_r e^{(-\lambda_r D)}$ where $N(D)$ is the number of raindrops with diameter D, N_r is the total number concentration of raindrops and λ_r is the slope parameter. For a) $N(D)$ was calculated using mean N_r and λ_r values. For the base aerosol loading average N_r was 19300 m^{-3}, distributed with a slope parameter of 23.7 $\times$ $10^3\,\mathrm{m}^{-1}$. For b) Mean N_r and λ_r values from only the 0.2 mmhr^{-1} intensity bin were used to calculate $N(D)$. For the base case N_r=40100 m^{-3} and λ_r=15.5 $\times$ $10^3\,\mathrm{m}^{-1}$. Other intensity bins were similar (not shown). Averages were taken over time and space, for rainy time steps only.

inversely related to cloud droplet number concentration in the model, reflecting the decrease in collision efficiency with cloud droplet size. In contrast, the penetration of the cloud above the freezing level in the supercell means that these droplets, which survive longer in the cloud, can freeze if lifted above the freezing level. This is demonstrated by an increase in mass and number of cloud ice particles in the supercell with increased aerosol loading (Fig. 5.4). Extra latent heat released by freezing drives an enhancement of convection in the cloud which strengthens updraft velocities (Fig. 5.7), leading to a delayed increase in surface rainfall (Fig. 5.5). These results are broadly in qualitative agreement with those presented by *Fan et al.* [2012]. The aerosol invigoration effect is usually associated with greater cloud top heights, which result from enhanced convection under more polluted conditions. A temperature inversion at about 12 km above the ground may explain why this is not

seen in the supercell case.

To estimate the total soil erosion for the base CCN level in each case study, total erosivity is multiplied by the RUSLE slope factor, S, to account for the increase in erosion with terrain steepness [*Yang et al.*, 2003; *Wischmeier and Smith*, 1978; *Renard et al.*, 1997]:

$$\begin{aligned} S &= 10.8\, sin\beta + 0.03 \quad tan\beta < 0.09 \\ S &= 10.8\, sin\beta - 0.50 \quad tan\beta \geq 0.09 \end{aligned} \tag{5.3}$$

where β is the slope angle. The soil loss is about 2 tons/acre for the supercell (8400 tons in total for the domain) and 0.2 tons/acre for the hill case (30 tons in total), based on Figure 4 from *Kinnell et al.* [1994] and assuming a runoff coefficient of 1 (k from equation 5.1). These soil loss estimates are first order approximations, so the error incurred by this assumption is neglected.

5.5.2 Response of erosivity to aerosols

According to both formulations (equations 5.1 and 5.2), erosivity is proportional to the product of two positively correlated variables: kinetic energy flux and rain intensity (Fig. 5.8). The change in erosivity with aerosol concentrations can therefore mostly be expected to be amplified beyond the change in total rainfall, $I = \sum_t i(\triangle t)$.

However, referring to the same definition, erosivity changes are also dominated more by the upper end of the rainfall intensity/energy distribution than are changes in total rainfall. The top 10% of rain intensity values constitute 69% of domain total erosivity in the supercell and 89% in the hill case. As a result, when extreme rain intensity changes more or less than the average, this will differentially impact erosivity compared with precipitation, and the amplification may either be enhanced further or dampened. In extreme cases, changes in erosivity could even oppose changes in mean rain intensity, when these are decoupled from changes to the upper end of the precipitation distribution. These results indicate that there is a complex erosivity response to increasing aerosol that differs from the mean precipitation signal.

It is also worth noting that the change in the product of the sum does not equate to change in the sum of the product: $\sum_t e_t i_t k(\triangle t)^2 \neq \sum_t e_t \sum_t i_t k(\triangle t)^2$. Total rainfall and energy increased by 25% and 29% in the supercell case. The increase in

erosivity computed directly from these total changes would be 61%, compared with 36% obtained by summing the product of energy and intensity. For the hill case the reductions in rainfall and energy were 71% and 81% respectively, giving a 94% decrease in erosivity computed directly from these total changes, compared with 90% from the model calculations. This gives further justification for this approach: both runoff and energy data are needed throughout the rainy period, as the same results cannot be achieved from accumulated values during a storm. This information is most easily acquired using a modelling approach.

5.5.3 Raindrop size

Changes in raindrop size can either amplify or mitigate the sensitivity of erosivity to aerosols. Large raindrops have been shown to contribute disproportionately to rainfall kinetic energy flux compared with their mass and number (chapter 4), and therefore constitute a greater fraction of total erosivity than surface precipitation. Consequently, drop size changes can differentially affect the sensitivities of erosivity and precipitation to aerosols.

Drop size distribution measurements show that raindrop size is positively correlated with intensity [*Laws and Parsons*, 1943] but in the model microphysics scheme this is only achieved for intensities below about $20\,\mathrm{mmhr}^{-1}$ (Fig. 5.17) (refer to sec. 4.3.2 for an explanation of this). Nonetheless, raindrop size in the supercell does increase (Fig. 5.10), driven by an increase in the intensity of lighter rainfall, for which the model is able to simulate this positive correlation. This suggests that the amplification of erosivity (R) in the supercell case may be underestimated by this scheme, as the energy-intensity relationship would be steeper with a more realistic treatment of drop size. This is consistent with a larger increase in R_R than R in the supercell case (Fig. 5.9). In the hill case, rain intensity is always below $20\,\mathrm{mmhr}^{-1}$, so the limitations of drop size simulation in the model microphysics do not apply.

Two key differences between the modelled kinetic energy flux in the supercell and hill cases are notable (Fig. 5.14). First, supercell raindrops are larger and thus have higher kinetic energies for similar intensities than in the gentler orographic rain case. Rain in the supercell case is largely the result of melting graupel, which naturally produces larger drops than those formed by collision and coalescence processes in the warm part of the cloud. In addition, stronger updrafts in the supercell also increase raindrop size. Raindrops fall when their weight overcomes the force of updrafts

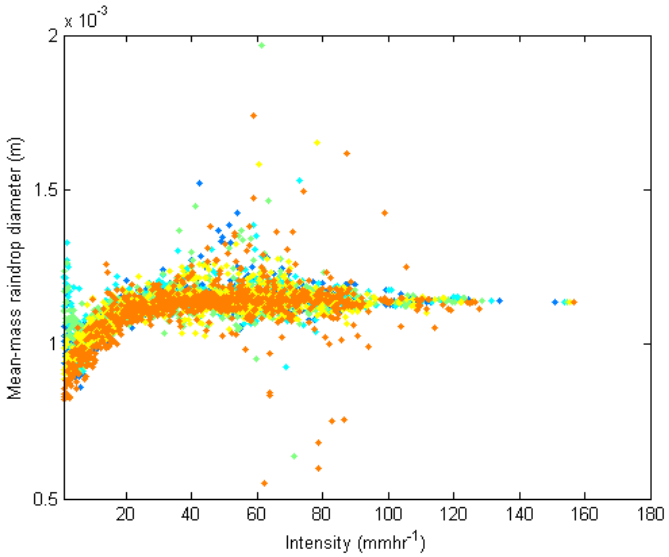

Figure 5.17: Mean-mass raindrop diameter (m) as a function of rainfall intensity (mmhr^{-1}). Averages were taken over the whole domain and the mean bin values are insensitive to the size of the intensity bins.

suspending them in the air, and thus grow to a larger size before precipitating when updrafts are strong. In the Morrison scheme vertical wind speed does not appear directly in the calculation of drop velocity, but this is indirectly accounted for by advection (sec. 2.4.4).

Second, in the hill case rainfall kinetic energy flux increases with CCN for a given intensity of rain, while the kinetic energy-intensity relationship for the supercell is relatively well constrained and insensitive to aerosol loading (Fig. 5.14). Overall, drop size decreases with increasing aerosol concentrations in the hill case, leading to a reduction in mean precipitation intensity (Fig. 5.16a). This corresponds to a shift along the kinetic energy-intensity curve in Fig. 5.14. Surprisingly, despite this reduction in rainfall drops are actually larger for a given rain intensity (Fig. 5.16b). Overall, less rain falls in the polluted scenario, but erosivity for a given intensity of rain is greater. This is illustrated by an upward shift in the kinetic energy-intensity curve for the hill case (Fig. 5.14). This mitigates the decrease in erosivity and the amplification of the erosivity change compared with the change in total rainfall. The overall outcome is a reduction in total rainfall brought about by smaller cloud droplets, but a subtle invigoration effect also occurs. Instantaneous saturation adjustment in the model is independent of particle size, but the diffusional growth stage of droplets in the polluted cloud is prolonged by the decrease in collision

efficiency of the smaller droplets, increasing the total mass of condensate (20% rise in liquid water content) [*Khain et al.*, 2005]. This releases extra latent heat, driving an intensification of air flow in the cloud. Stronger vertical velocities can support heavier raindrops, which grow to a larger size for a given intensity.

The supercell case does not exhibit a similar drop size effect for a given intensity, despite a clear invigoration effect (the kinetic energy-intensity curve in Fig. 5.8 is well constrained). This can partly be explained by the failure of the model microphysics scheme to replicate the observed increase in raindrop size with intensity, except for light rainfall. Updrafts drive moisture convergence at the cloud base, and are therefore closely related to rain intensity; stronger updrafts force more moisture to rise through the cloud and cause more rainfall. Therefore, if the size of the modelled raindrops is constant with intensity above a given threshold, stronger updrafts will not have the expected drop size effect.

5.6 Conclusions

The response of rainfall erosivity to atmospheric aerosols was modelled in two idealised simulations with a cloud-resolving version of the WRF model. In a mixed-phase stationary supercell storm, increased aerosol loading enhanced surface rainfall and erosivity. A warm rain case study with light orographic precipitation demonstrated the opposite response, with a reduction in both precipitation and erosivity. Results demonstrate that in both cases the change in erosivity with increasing aerosol concentrations is in the same direction as, but amplified beyond, the change in accumulated rainfall.

This amplification stems from the fact that erosivity is proportional to the product of two positively correlated variables, rainfall intensity and energy. Because of this, changes in extreme rainfall intensity dominate the erosivity signal, and where the behaviour of extreme rainfall differs from the mean, the amplification may be enhanced further or dampened. The effect of aerosols on raindrop size has a disproportionate impact on erosivity compared with surface precipitation, and can either enhance or mitigate the overall amplification signal.

The amplification of the change in erosivity compared with total rainfall is consistent with results from *Nearing et al.* [2005], who perturbed rainfall data and forced several erosion models (including the RUSLE and process based models) to estimate the

impacts on erosion. These authors found that the sensitivity of erosion to increases in rain intensity and amount while maintaining a constant rainfall duration, and to increases in rainfall duration and amount at constant intensity, were at least one for all the erosion models tested. *Pruski and Nearing* [2002a] found that a 1% increase in total rainfall, allowing intensity and amount to vary together, could lead to a 1.7% increase in erosion, holding all soil factors constant.

These results suggest that anthropogenic aerosol emissions affect rainfall erosivity in a manner which is not obvious from the precipitation response. The complexities of many competing cloud processes can result in different outcomes, and other cases may involve subtle combinations of the examples discussed here. In particular, the experiments presented here pertain to this model setup and microphysics scheme. The cloud and precipitation responses to increasing aerosol concentrations in each case study may differ among schemes. Indeed, the sign of the precipitation sensitivity to aerosols using other schemes could even be different for the same case study. The extent of the amplification will be affected by differences in modelled raindrop sizes and shifts in the rainfall distribution, but the positive correlation between kinetic energy flux and intensity suggests that there should still be an amplification of the erosivity change when compared with the precipitation response.

There are several intriguing implications of these results. It is generally accepted that heavy rain, which is more likely to be produced by mixed-phase clouds, is responsible for the dominant share of erosion [*Zender*, 2005; *Boardman*, 2006]. The most erosive clouds may therefore have a positive erosivity sensitivity to aerosols and the drive for reducing urban aerosol emissions could benefit regional agricultural productivity. Agricultural practices like biomass burning could have a negative impact on productivity by increasing erosion. However, the response of mixed-phase clouds to changing aerosol concentrations can vary in response to environmental conditions. In particular, low humidity and high wind shear are understood to discourage the aerosol invigoration effect (sec. 1.2.5), and in these cases reductions in background aerosol concentrations could result in more erosion. Aerosol induced circulation changes would also have a major influence on precipitation, but have not been considered here.

These findings also raise sensitive questions about accountability for the consequences of polluting activities. Cities account for the bulk of aerosols emitted, which in turn impact rural practices, and agricultural productivity in regions close

to cities is likely to be differentially affected compared with more remote regions. Further work might involve an investigation of aerosol-erosion feedbacks; in regions where precipitation correlates positively with dust loading for example [*Zender*, 2005], there is the possibility of a positive dust-aerosol-erosion feedback.

Summary and conclusions

This thesis has investigated the potential of regional climate models to be used for soil erosion studies. Current soil erosion models include considerable detail concerning processes occurring within the soil, but employ a simplified treatment of rainfall. There is therefore potential for a new perspective on erosion prediction and modelling with an atmospheric science focus. Regional climate models include the physics of rain formation processes and can be used to simulate rainfall erosivity, an indicator of the capacity of rain to erode soil.

Rainfall erosivity was modelled using the Weather Research and Forecasting (WRF) model forced with CFSR reanalysis data for 2009 in the Caucasus region. Low intensity rain below $2\,\mathrm{mmhr}^{-1}$ was found to contribute an average of 23% to total erosivity, questioning the common assumption that only heavy rain can be erosive. An exponential dependence of the fraction of erosivity from light rain on the proportion of light rain in the local climate was found. Light rainfall occurring between storms was found to contribute significantly to rainfall erosivity. Between 9 and 30% of erosivity may be excluded from the storm-based calculations in the (Revised) Universal Soil Loss Equation. Excluding light rain does not lead to errors in predicted soil loss over long periods, but could cause an underestimation of erosion from individual events.

The kinetic energy flux of rainfall is an important determinant of soil detachment and erosion, and is currently parameterised from rainfall intensity. Chapter 4 presented the first dynamic simulation of rainfall kinetic energy flux, using a cloud resolving version of the WRF model. It was shown that several commonly used microphysics parameterisation schemes are capable of modelling the energy flux within the range of observations reported in the literature. This broadly captures the observed variability in kinetic energy flux for a given intensity, where current methods fail. This method can easily be extended for use in a full regional climate model run at convection resolving scales. In addition, large raindrops were shown to contribute

disproportionately to rainfall kinetic energy flux, and also to the surface precipitation rate, compared with their number. This suggests that more emphasis should be placed on correctly parameterising the fall speeds of larger raindrops, as several commonly used methods overestimate large drop velocities.

In chapter 5 the effect of atmospheric aerosols on soil erosion was explored for the first time. A mixed-phase stationary supercell storm exhibited invigoration of ice processes and an enhancement of precipitation with increased aerosol loading. A warm orographic raincloud demonstrated a reduction in precipitation. It was found that in both these cases the change in erosivity was in the same direction as, but amplified beyond, the change in surface precipitation. Aerosol-induced changes in raindrop size have a disproportionate impact on erosivity compared with surface precipitation, and can either enhance or mitigate this amplification.

With a rising world population and the uncertainties of a changing climate, sustainable food production is a primary concern. Soil erosion poses a serious threat to agricultural productivity. The work presented here demonstrates the importance of atmospheric processes for soil erosion, and argues that a consideration of these effects is necessary. Coupling an atmospheric model with a more complex land surface model capable of simulating erosion would be required to realise the full potential of regional climate models for erosion applications. This would permit an investigation of atmosphere-erosion feedback processes, which are not accounted for in current erosion models.

Appendix

Appendix A: Model setup for chapter 3 simulations

For real data simulations, the WRF Preprocessing System (WPS) was used to generate model input files from CFSR reanalysis data. A text file, namelist.wps, is needed to specify the model domain and options for WPS. A second text file, namelist.input, is used to specify run-time model setup options.

namelist.wps file:

```
&share
wrf_core              = 'ARW',
max_dom               = 1
start_date            = '2009-01-01_01:00:00'
end_date              = '2010-01-01_01:00:00'
interval_seconds      = 21600,
io_form_geogrid       = 2,
/
&geogrid
parent_id             = 1, 1,
parent_grid_ratio     = 1, 5,
i_parent_start        = 1, 38,
j_parent_start        = 1, 46,
e_we                  = 83, 471,
e_sn                  = 50, 291,
geog_data_res         = '5m', '30s',
dx                    = 20000,
dy                    = 20000,
```

```
map_proj            = 'lambert',
ref_lat             = 41.5,
ref_lon             = 45,
truelat1            = 41.5,
truelat2            = 41.5,
stand_lon           = 45,
geog_data_path      = './geog/'
/
```

namelist.input file:

```
&time_control
run_days                    =   0,
run_hours                   =   0,
run_minutes                 =   0,
run_seconds                 =   0,
start_year                  =   2009,
start_month                 =   01,
start_day                   =   01,
start_hour                  =   01,
start_minute                =   00,
start_second                =   00,
end_year                    =   2010,
end_month                   =   01,
end_day                     =   01,
end_hour                    =   01,
end_minute                  =   00,
end_second                  =   00,
interval_seconds            =   21600
input_from_file             =   .true.,
history_interval            =   30,
frames_per_outfile          =   336,
restart                     =   .false.,
restart_interval            =   10080,
io_form_history             =   2,
```

```
io_form_auxinput4           =  2,
auxinput4_inname            =  wrflowinp_d<domain>
auxinput4_interval          =  360,
io_form_auxinput4           =  2,
io_form_restart             =  2,
io_form_input               =  2,
io_form_boundary            =  2,
ignore_iofields_warning     =  .true.,
debug_level                 =  0
/

&domains
time_step                   =  20,
time_step_fract_num         =  0,
time_step_fract_den         =  1,
max_dom                     =  1,
e_we                        =  83,
e_sn                        =  50,
e_vert                      =  60,
p_top_requested             =  5000,
num_metgrid_levels          =  38,
num_metgrid_soil_levels     =  4,
dx                          =  20000,
dy                          =  20000,
grid_id                     =  1,
parent_id                   =  1,
i_parent_start              =  1,
j_parent_start              =  1,
parent_grid_ratio           =  1,
parent_time_step_ratio      =  1,
feedback                    =  0,
smooth_option               =  0
/

&physics
```

```
mp_physics                  =  8,
ra_lw_physics               =  1,
ra_sw_physics               =  1,
radt                        =  10,
sf_sfclay_physics           =  2,
sf_surface_physics          =  2,
bl_pbl_physics              =  2,
bldt                        =  0,
cu_physics                  =  1,
cudt                        =  5,
sst_update                  =  1,
sst_skin                    =  1,
isfflx                      =  1,
ifsnow                      =  0,
icloud                      =  1,
surface_input_source        =  1,
num_soil_layers             =  4,
sf_urban_physics            =  0,
maxiens                     =  1,
maxens                      =  3,
maxens2                     =  3,
maxens3                     =  16,
ensdim                      =  144,
/

&fdda
/

&dynamics
w_damping                   =  1,
diff_opt                    =  2,
km_opt                      =  4,
diff_6th_opt                =  2,
diff_6th_factor             =  0.12,
base_temp                   =  290
```

```
damp_opt                = 3,
zdamp                   = 5000.,
dampcoef                = 0.2,
khdif                   = 0,
kvdif                   = 0,
non_hydrostatic         = .true.,
moist_adv_opt           = 1,
scalar_adv_opt          = 1,
/

&bdy_control
spec_bdy_width          = 5,
spec_zone               = 1,
relax_zone              = 4,
specified               = .true.,
nested                  = .false.,
/

&grib2
/

&namelist_quilt
nio_tasks_per_group     = 0,
nio_groups              = 1,
/
```

Appendix B: Model setup for chapter 4 simulations

For idealised simulations the initial conditions are provided by a text file, input_sounding. In this file the first row gives the surface pressure (hPa), potential temperature (K) and water vapour mixing ratio (gkg^{-1}). For the remaining rows the five columns are, from left to right, height (m above sea level), potential temperature (K), water vapour mixing ratio (gkg^{-1}) and x- and y-components of the wind vector (ms^{-1}). A namelist.input file is still required to specify run time model setup options.

The default WRF supercell case study (em_quarter_ss) was used for the simula-

tions presented in chapter 4. In the namelist.input file, mp_physics was changed in order to implement the different microphysics parameterisation options discussed in the text: Thompson (8), Milbrandt-Yau (9), Morrison (10), WDM6 (16). Within the Thompson and Milbrandt-Yau schemes, experiments were performed using both exponential and gamma raindrop size distributions. For this, the parameters mu_r (Thompson) and alpha_r (Milbrandt-Yau) were set to 0 for an exponential and 1 for a gamma DSD within the code for each scheme. For the drop velocity experiments discussed in sec. 4.3.3, the parameters av_r, bv_r and fv_r in the Thompson parameterisation code represent the parameters a, b and f in the V(D) expression given by equation 2.14. These were changed to the values given by Tab. 2.3 in order to implement the velocity expressions from Morrison, Milbrandt-Yau and WDM6 within the Thompson scheme.

input_sounding file:

1000	300	14		
250	300.45	14	-7.88	-3.58
750	301.25	14	-6.94	-0.89
1250	302.47	13.5	-5.17	1.33
1750	303.93	11.1	-2.76	2.84
2250	305.31	9.06	0.01	3.47
2750	306.81	7.36	2.87	3.49
3250	308.46	5.95	5.73	3.49
3750	310.03	4.78	8.58	3.49
4250	311.74	3.82	11.44	3.49
4750	313.48	3.01	14.3	3.49
5250	315.24	2.36	17.15	3.49
5750	317.18	1.8	20.01	3.49
6250	319.02	1.41	22.87	3.49
6750	320.88	1.07	25.73	3.49
7250	322.8	0.8	27.15	3.49
7750	324.87	0.6	27.15	3.49
8250	326.86	0.43	27.15	3.49
8750	328.89	0.32	27.15	3.49
9250	330.39	0.24	27.15	3.49

9750	332.8	0.17	27.15	3.49
10250	335.23	0.1	27.15	3.49
10750	337.31	0.08	27.15	3.49
11250	339.55	0.05	27.15	3.49
11750	342.82	0.03	27.15	3.49
12250	349.88	0.04	27.15	3.49
12750	357.34	0.04	27.15	3.49
13250	364.91	0.04	27.15	3.49
13750	373.22	0.04	27.15	3.49
14250	381.67	0.04	27.15	3.49
14750	390.29	0.04	27.15	3.49
15250	398.91	0.04	27.15	3.49
15750	407.53	0.04	27.15	3.49
16250	416.15	0.04	27.15	3.49
16750	424.77	0.04	27.15	3.49
17250	433.39	0.04	27.15	3.49
17750	442.01	0.04	27.15	3.49
18250	450.63	0.04	27.15	3.49
18750	459.25	0.04	27.15	3.49
19250	467.87	0.04	27.15	3.49
19750	476.49	0.04	27.15	3.49
20250	485.11	0.04	27.15	3.49
20750	493.73	0.04	27.15	3.49
21250	502.35	0.04	27.15	3.49
21750	510.97	0.04	27.15	3.49
22250	519.59	0.04	27.15	3.49
22750	528.21	0.04	27.15	3.49

namelist.input file:

```
&time_control
run_days                            =   0,
run_hours                           =   0,
run_minutes                         =   120,
run_seconds                         =   0,
```

```
start_year                          =   0001,
start_month                         =   01,
start_day                           =   01,
start_hour                          =   00,
start_minute                        =   00,
start_second                        =   00,
end_year                            =   0001,
end_month                           =   01,
end_day                             =   01,
end_hour                            =   00,
end_minute                          =   120,
end_second                          =   00,
history_interval                    =   10,
frames_per_outfile                  =   1000,
restart                             =   .false.,
restart_interval                    =   120,
io_form_history                     =   2
io_form_restart                     =   2
io_form_input                       =   2
io_form_boundary                    =   2
debug_level                         =   0
/

&domains
time_step                           =   12,
time_step_fract_num                 =   0,
time_step_fract_den                 =   1,
max_dom                             =   1,
s_we                                =   1,
e_we                                =   42,
s_sn                                =   1,
e_sn                                =   42,
s_vert                              =   1,
e_vert                              =   41,
dx                                  =   2000,
```

```
dy                          =  2000,
ztop                        =  20000,
grid_id                     =  1,
parent_id                   =  0,
i_parent_start              =  0,
j_parent_start              =  0,
parent_grid_ratio           =  1,
parent_time_step_ratio      =  1,
feedback                    =  1,
smooth_option               =  0
/

&physics
mp_physics                  =  8,
ra_lw_physics               =  0,
ra_sw_physics               =  0,
radt                        =  30,
sf_sfclay_physics           =  0,
sf_surface_physics          =  0,
bl_pbl_physics              =  0,
bldt                        =  0,
cu_physics                  =  0,
cudt                        =  5,
num_soil_layers             =  5,
/

&fdda
/

&dynamics
rk_ord                      =  3,
diff_opt                    =  2,
km_opt                      =  2,
damp_opt                    =  2,
zdamp                       =  5000.,
```

```
 dampcoef                    =   0.003,
 khdif                       =   500,
 kvdif                       =   500,
 smdiv                       =   0.1,
 emdiv                       =   0.01,
 epssm                       =   0.1,
 time_step_sound             =   6,
 h_mom_adv_order             =   5,
 v_mom_adv_order             =   3,
 h_sca_adv_order             =   5,
 v_sca_adv_order             =   3,
 moist_adv_opt               =   1,
 scalar_adv_opt              =   1,
 chem_adv_opt                =   1,
 tke_adv_opt                 =   1,
 non_hydrostatic             =   .true.,
 mix_full_fields             =   .true.,
 /

 &bdy_control
 periodic_x                  =   .false.,
 symmetric_xs                =   .false.,
 symmetric_xe                =   .false.,
 open_xs                     =   .true.,
 open_xe                     =   .true.,
 periodic_y                  =   .false.,
 symmetric_ys                =   .false.,
 symmetric_ye                =   .false.,
 open_ys                     =   .true.,
 open_ye                     =   .true.,
 nested                      =   .false.,
 /

 &grib2
 /
```

```
&namelist_quilt
nio_tasks_per_group      =  0,
nio_groups               =  1,
/
```

Appendix C: Model setup for chapter 5 simulations

Stationary supercell case study

The default WRF supercell case study (em_quarter_ss) was adapted to reduce the imposed wind speed to zero in the x- and y-directions and to increase the water vapour mixing ratio by 7% from the default input_sounding file. The following table gives the values of key parameters set in the Morrison microphysics parameterisation code for the updated version with prognostic cloud droplet number concentration. This code was provided by Hugh Morrison. All other parameters were given their default values.

Parameter	Value/range	Description
K1	0.308	exponent in CCN distribution (k in equation 1.7)
C1	300 to 1200	Background CCN concentration (c in equation 1.7)
ISUB	1	Use grid scale vertical velocity for droplet activation

input_sounding file:

```
1000    300     14
250     300.45  14.98   0   0
750     301.25  14.98   0   0
1250    302.47  14.445  0   0
1750    303.93  11.877  0   0
2250    305.31  9.6942  0   0
2750    306.81  7.8752  0   0
3250    308.46  6.3665  0   0
3750    310.03  5.1146  0   0
4250    311.74  4.0874  0   0
4750    313.48  3.2207  0   0
```

5250	315.24	2.5252	0	0
5750	317.18	1.926	0	0
6250	319.02	1.5087	0	0
6750	320.88	1.1449	0	0
7250	322.8	0.856	0	0
7750	324.87	0.642	0	0
8250	326.86	0.4601	0	0
8750	328.89	0.3424	0	0
9250	330.39	0.2568	0	0
9750	332.8	0.1819	0	0
10250	335.23	0.107	0	0
10750	337.31	0.0856	0	0
11250	339.55	0.0535	0	0
11750	342.82	0.0321	0	0
12250	349.88	0.0428	0	0
12750	357.34	0.0428	0	0
13250	364.91	0.0428	0	0
13750	373.22	0.0428	0	0
14250	381.67	0.0428	0	0
14750	390.29	0.0428	0	0
15250	398.91	0.0428	0	0
15750	407.53	0.0428	0	0
16250	416.15	0.0428	0	0
16750	424.77	0.0428	0	0
17250	433.39	0.0428	0	0
17750	442.01	0.0428	0	0
18250	450.63	0.0428	0	0
18750	459.25	0.0428	0	0
19250	467.87	0.0428	0	0
19750	476.49	0.0428	0	0
20250	485.11	0.0428	0	0
20750	493.73	0.0428	0	0
21250	502.35	0.0428	0	0
21750	510.97	0.0428	0	0
22250	519.59	0.0428	0	0

22750 528.21 0.0428 0 0

namelist.input file:

```
&time_control
run_days                            =   0,
run_hours                           =   0,
run_minutes                         =   240,
run_seconds                         =   0,
start_year                          =   0001,
start_month                         =   01,
start_day                           =   01,
start_hour                          =   00,
start_minute                        =   00,
start_second                        =   00,
end_year                            =   0001,
end_month                           =   01,
end_day                             =   01,
end_hour                            =   00,
end_minute                          =   120,
end_second                          =   00,
history_interval                    =   10,
frames_per_outfile                  =   1000,
restart                             =   .false.,
restart_interval                    =   120,
io_form_history                     =   2
io_form_restart                     =   2
io_form_input                       =   2
io_form_boundary                    =   2
debug_level                         =   0
/

&domains
time_step                           =   6,
time_step_fract_num                 =   0,
```

```
time_step_fract_den     =  1,
max_dom                 =  1,
s_we                    =  1,
e_we                    =  42,
s_sn                    =  1,
e_sn                    =  42,
s_vert                  =  1,
e_vert                  =  61,
dx                      =  1000,
dy                      =  1000,
ztop                    =  20000,
grid_id                 =  1,
parent_id               =  0,
i_parent_start          =  0,
j_parent_start          =  0,
parent_grid_ratio       =  1,
parent_time_step_ratio  =  1,
feedback                =  1,
smooth_option           =  0
/

&physics
mp_physics              =  10,
ra_lw_physics           =  0,
ra_sw_physics           =  0,
radt                    =  30,
sf_sfclay_physics       =  0,
sf_surface_physics      =  0,
bl_pbl_physics          =  0,
bldt                    =  0,
cu_physics              =  0,
cudt                    =  5,
isfflx                  =  1,
ifsnow                  =  0,
icloud                  =  1,
```

```
num_soil_layers     =  5,
mp_zero_out         =  0,
/

&fdda
/

&dynamics
rk_ord              =  3,
diff_opt            =  2,
km_opt              =  2,
damp_opt            =  2,
zdamp               =  5000.,
dampcoef            =  0.003,
khdif               =  500,
kvdif               =  500,
smdiv               =  0.1,
emdiv               =  0.01,
epssm               =  0.1,
time_step_sound     =  6,
h_mom_adv_order     =  5,
v_mom_adv_order     =  3,
h_sca_adv_order     =  5,
v_sca_adv_order     =  3,
moist_adv_opt       =  1,
scalar_adv_opt      =  1,
chem_adv_opt        =  1,
tke_adv_opt         =  1,
non_hydrostatic     =  .true.,
mix_full_fields     =  .true.,
/

&bdy_control
periodic_x          =  .false
symmetric_xs        =  .false
```

```
symmetric_xe            =   .false
open_xs                 =   .true.
open_xe                 =   .true.
periodic_y              =   .false
symmetric_ys            =   .false
symmetric_ye            =   .false
open_ys                 =   .true.
open_ye                 =   .true.
nested                  =   .false
/

&grib2
/

&namelist_quilt
nio_tasks_per_group     =   0,
nio_groups              =   1,
/
```

Hill case study

The default WRF case study for flow over an orographic hill (em_hill2d_x) was adapted for a moist tropical environment using the input_sounding file given below. The dimensions of the hill were set in the case initialisation file (module_initialize_hill2d_x.F): hill height was 2km (hm=2000) and half width was 30km (xa=30). The microphysics setup was the same as for the stationary supercell case.

input_sounding file:

```
1013    299.7   16.11
0       299.7   16.11   10   0
50      299.89  15.91   10   0
100     300.07  15.71   10   0
150     300.26  15.51   10   0
200     300.44  15.31   10   0
```

250	300.63	15.11	10	0
300	300.81	14.91	10	0
350	301	14.71	10	0
400	301.18	14.51	10	0
450	301.37	14.31	10	0
500	301.56	14.11	10	0
550	301.74	13.91	10	0
600	301.93	13.71	10	0
650	302.11	13.51	10	0
700	302.3	13.31	10	0
750	302.48	13.11	10	0
800	302.67	12.91	10	0
850	302.85	12.71	10	0
900	303.04	12.51	10	0
950	303.22	12.31	10	0
1000	303.41	12.11	10	0
1050	303.6	11.98	10	0
1100	303.79	11.85	10	0
1150	303.98	11.72	10	0
1200	304.17	11.59	10	0
1250	304.36	11.47	10	0
1300	304.55	11.34	10	0
1350	304.75	11.21	10	0
1400	304.94	11.08	10	0
1450	305.13	10.95	10	0
1500	305.32	10.82	10	0
1550	305.51	10.69	10	0
1600	305.7	10.56	10	0
1650	305.89	10.43	10	0
1700	306.08	10.3	10	0
1750	306.27	10.18	10	0
1800	306.46	10.05	10	0
1850	306.65	9.92	10	0
1900	306.84	9.79	10	0
1950	307.04	9.66	10	0

2000	307.23	9.53	10	0
2050	307.53	9.32	10	0
2100	307.84	9.11	10	0
2150	308.15	8.9	10	0
2200	308.46	8.69	10	0
2250	308.77	8.48	10	0
2300	309.08	8.27	10	0
2350	309.38	8.07	10	0
2400	309.69	7.86	10	0
2450	310	7.65	10	0
2500	310.31	7.44	10	0
2550	310.62	7.23	10	0
2600	310.93	7.02	10	0
2650	311.23	6.81	10	0
2700	311.54	6.6	10	0
2750	311.85	6.39	10	0
2800	312.16	6.18	10	0
2850	312.47	5.97	10	0
2900	312.78	5.76	10	0
2950	313.08	5.55	10	0
3000	313.39	5.34	10	0
3050	313.56	5.21	10	0
3100	313.74	5.09	10	0
3150	313.91	4.96	10	0
3200	314.08	4.83	10	0
3250	314.25	4.7	10	0
3300	314.42	4.57	10	0
3350	314.6	4.44	10	0
3400	314.77	4.31	10	0
3450	314.94	4.18	10	0
3500	315.11	4.05	10	0
3550	315.28	3.92	10	0
3600	315.45	3.79	10	0
3650	315.63	3.66	10	0
3700	315.8	3.53	10	0

3750	315.97	3.41	10	0
3800	316.14	3.28	10	0
3850	316.31	3.15	10	0
3900	316.48	3.02	10	0
3950	316.66	2.89	10	0
4000	316.83	2.76	10	0
4050	317	2.73	10	0
4100	317.18	2.69	10	0
4150	317.36	2.66	10	0
4200	317.53	2.62	10	0
4250	317.71	2.59	10	0
4300	317.88	2.56	10	0
4350	318.06	2.52	10	0
4400	318.23	2.49	10	0
4450	318.41	2.45	10	0
4500	318.59	2.42	10	0
4550	318.76	2.39	10	0
4600	318.94	2.35	10	0
4650	319.11	2.32	10	0
4700	319.29	2.28	10	0
4750	319.47	2.25	10	0
4800	319.64	2.22	10	0
4850	319.82	2.18	10	0
4900	319.99	2.15	10	0
4950	320.17	2.11	10	0
5000	320.34	2.08	10	0
5050	320.53	2.04	10	0
5100	320.71	2	10	0
5150	320.89	1.96	10	0
5200	321.08	1.92	10	0
5250	321.26	1.89	10	0
5300	321.44	1.85	10	0
5350	321.63	1.81	10	0
5400	321.81	1.77	10	0
5450	321.99	1.73	10	0

5500	322.18	1.69	10	0
5550	322.36	1.65	10	0
5600	322.54	1.61	10	0
5650	322.73	1.58	10	0
5700	322.91	1.54	10	0
5750	323.09	1.5	10	0
5800	323.28	1.46	10	0
5850	323.46	1.42	10	0
5900	323.64	1.38	10	0
5950	323.83	1.34	10	0
6000	324.01	1.31	10	0
6050	324.2	1.28	10	0
6100	324.39	1.25	10	0
6150	324.59	1.23	10	0
6200	324.78	1.2	10	0
6250	324.97	1.18	10	0
6300	325.16	1.15	10	0
6350	325.36	1.13	10	0
6400	325.55	1.1	10	0
6450	325.74	1.08	10	0
6500	325.93	1.05	10	0
6550	326.13	1.03	10	0
6600	326.32	1	10	0
6650	326.51	0.98	10	0
6700	326.7	0.95	10	0
6750	326.89	0.93	10	0
6800	327.09	0.9	10	0
6850	327.28	0.88	10	0
6900	327.47	0.85	10	0
6950	327.66	0.83	10	0
7000	327.86	0.8	10	0
7050	328.05	0.78	10	0
7100	328.24	0.77	10	0
7150	328.44	0.75	10	0
7200	328.63	0.74	10	0

7250	328.82	0.72	10	0
7300	329.02	0.7	10	0
7350	329.21	0.69	10	0
7400	329.4	0.67	10	0
7450	329.6	0.65	10	0
7500	329.79	0.64	10	0
7550	329.98	0.62	10	0
7600	330.18	0.61	10	0
7650	330.37	0.59	10	0
7700	330.57	0.57	10	0
7750	330.76	0.56	10	0
7800	330.95	0.54	10	0
7850	331.15	0.52	10	0
7900	331.34	0.51	10	0
7950	331.53	0.49	10	0
8000	331.73	0.47	10	0
8050	331.94	0.46	10	0
8100	332.14	0.45	10	0
8150	332.35	0.44	10	0
8200	332.56	0.43	10	0
8250	332.77	0.42	10	0
8300	332.98	0.41	10	0
8350	333.19	0.4	10	0
8400	333.4	0.39	10	0
8450	333.61	0.38	10	0
8500	333.82	0.36	10	0
8550	334.03	0.35	10	0
8600	334.24	0.34	10	0
8650	334.45	0.33	10	0
8700	334.66	0.32	10	0
8750	334.86	0.31	10	0
8800	335.07	0.3	10	0
8850	335.28	0.29	10	0
8900	335.49	0.28	10	0
8950	335.7	0.27	10	0

9000	335.91	0.25	10	0
9050	336.12	0.25	10	0
9100	336.34	0.24	10	0
9150	336.55	0.23	10	0
9200	336.76	0.23	10	0
9250	336.97	0.22	10	0
9300	337.18	0.21	10	0
9350	337.4	0.21	10	0
9400	337.61	0.2	10	0
9450	337.82	0.19	10	0
9500	338.03	0.19	10	0
9550	338.24	0.18	10	0
9600	338.46	0.17	10	0
9650	338.67	0.17	10	0
9700	338.88	0.16	10	0
9750	339.09	0.15	10	0
9800	339.31	0.15	10	0
9850	339.52	0.14	10	0
9900	339.73	0.13	10	0
9950	339.94	0.13	10	0
10000	340.15	0.12	10	0
10050	340.36	0.12	10	0
10100	340.58	0.11	10	0
10150	340.79	0.11	10	0
10200	341	0.1	10	0
10250	341.21	0.1	10	0
10300	341.42	0.1	10	0
10350	341.63	0.09	10	0
10400	341.84	0.09	10	0
10450	342.05	0.09	10	0
10500	342.27	0.08	10	0
10550	342.48	0.08	10	0
10600	342.69	0.07	10	0
10650	342.9	0.07	10	0
10700	343.11	0.07	10	0

10750	343.32	0.06	10	0
10800	343.53	0.06	10	0
10850	343.74	0.06	10	0
10900	343.95	0.05	10	0
10950	344.17	0.05	10	0
11000	344.38	0.05	10	0
11050	344.61	0.04	10	0
11100	344.85	0.04	10	0
11150	345.09	0.04	10	0
11200	345.32	0.04	10	0
11250	345.56	0.04	10	0
11300	345.8	0.04	10	0
11350	346.03	0.04	10	0
11400	346.27	0.03	10	0
11450	346.51	0.03	10	0
11500	346.75	0.03	10	0
11550	346.98	0.03	10	0
11600	347.22	0.03	10	0
11650	347.46	0.03	10	0
11700	347.69	0.03	10	0
11750	347.93	0.02	10	0
11800	348.17	0.02	10	0
11850	348.4	0.02	10	0
11900	348.64	0.02	10	0
11950	348.88	0.02	10	0
12000	349.11	0.02	10	0
12050	349.38	0.02	10	0
12100	349.64	0.02	10	0
12150	349.9	0.02	10	0
12200	350.17	0.02	10	0
12250	350.43	0.02	10	0
12300	350.69	0.01	10	0
12350	350.96	0.01	10	0
12400	351.22	0.01	10	0
12450	351.48	0.01	10	0

12500	351.75	0.01	10	0
12550	352.01	0.01	10	0
12600	352.27	0.01	10	0
12650	352.54	0.01	10	0
12700	352.8	0.01	10	0
12750	353.06	0.01	10	0
12800	353.33	0.01	10	0
12850	353.59	0.01	10	0
12900	353.85	0.01	10	0
12950	354.12	0.01	10	0
13000	354.38	0.01	10	0
13050	354.61	0.01	10	0
13100	354.83	0.01	10	0
13150	355.06	0.01	10	0
13200	355.29	0.01	10	0
13250	355.51	0.01	10	0
13300	355.74	0.01	10	0
13350	355.96	0.01	10	0
13400	356.19	0.01	10	0
13450	356.42	0.01	10	0
13500	356.64	0.01	10	0
13550	356.87	0	10	0
13600	357.09	0	10	0
13650	357.32	0	10	0
13700	357.55	0	10	0
13750	357.77	0	10	0
13800	358	0	10	0
13850	358.23	0	10	0
13900	358.45	0	10	0
13950	358.68	0	10	0
14000	358.9	0	10	0
14050	359.19	0	10	0
14100	359.48	0	10	0
14150	359.76	0	10	0
14200	360.05	0	10	0

14250	360.34	0	10	0
14300	360.62	0	10	0
14350	360.91	0	10	0
14400	361.2	0	10	0
14450	361.48	0	10	0
14500	361.77	0	10	0
14550	362.06	0	10	0
14600	362.34	0	10	0
14650	362.63	0	10	0
14700	362.92	0	10	0
14750	363.2	0	10	0
14800	363.49	0	10	0
14850	363.78	0	10	0
14900	364.06	0	10	0
14950	364.35	0	10	0
15000	364.63	0	10	0
15050	364.93	0	10	0
15100	365.23	0	10	0
15150	365.52	0	10	0
15200	365.82	0	10	0
15250	366.11	0	10	0
15300	366.41	0	10	0
15350	366.7	0	10	0
15400	367	0	10	0
15450	367.29	0	10	0
15500	367.59	0	10	0
15550	367.88	0	10	0
15600	368.18	0	10	0
15650	368.47	0	10	0
15700	368.77	0	10	0
15750	369.06	0	10	0
15800	369.36	0	10	0
15850	369.65	0	10	0
15900	369.95	0	10	0
15950	370.24	0	10	0

16000	370.54	0	10	0
16050	371.24	0	10	0
16100	371.94	0	10	0
16150	372.64	0	10	0
16200	373.35	0	10	0
16250	374.05	0	10	0
16300	374.75	0	10	0
16350	375.45	0	10	0
16400	376.15	0	10	0
16450	376.85	0	10	0
16500	377.56	0	10	0
16550	378.26	0	10	0
16600	378.96	0	10	0
16650	379.66	0	10	0
16700	380.36	0	10	0
16750	381.07	0	10	0
16800	381.77	0	10	0
16850	382.47	0	10	0
16900	383.17	0	10	0
16950	383.87	0	10	0
17000	384.57	0	10	0
17050	385.96	0	10	0
17100	387.34	0	10	0
17150	388.72	0	10	0
17200	390.11	0	10	0
17250	391.49	0	10	0
17300	392.87	0	10	0
17350	394.25	0	10	0
17400	395.64	0	10	0
17450	397.02	0	10	0
17500	398.4	0	10	0
17550	399.79	0	10	0
17600	401.17	0	10	0
17650	402.55	0	10	0
17700	403.93	0	10	0

17750	405.32	0	10	0
17800	406.7	0	10	0
17850	408.08	0	10	0
17900	409.46	0	10	0
17950	410.85	0	10	0
18000	412.23	0	10	0
18050	413.68	0	10	0
18100	415.12	0	10	0
18150	416.57	0	10	0
18200	418.02	0	10	0
18250	419.47	0	10	0
18300	420.91	0	10	0
18350	422.36	0	10	0
18400	423.81	0	10	0
18450	425.25	0	10	0
18500	426.7	0	10	0
18550	428.15	0	10	0
18600	429.59	0	10	0
18650	431.04	0	10	0
18700	432.49	0	10	0
18750	433.94	0	10	0
18800	435.38	0	10	0
18850	436.83	0	10	0
18900	438.28	0	10	0
18950	439.72	0	10	0
19000	441.17	0	10	0
19050	442.69	0	10	0
19100	444.21	0	10	0
19150	445.72	0	10	0
19200	447.24	0	10	0
19250	448.76	0	10	0
19300	450.28	0	10	0
19350	451.79	0	10	0
19400	453.31	0	10	0
19450	454.83	0	10	0

19500	456.35	0	10	0
19550	457.86	0	10	0
19600	459.38	0	10	0
19650	460.9	0	10	0
19700	462.42	0	10	0
19750	463.93	0	10	0
19800	465.45	0	10	0
19850	466.97	0	10	0
19900	468.49	0	10	0
19950	470	0	10	0
20000	471.52	0	10	0

namelist.input file:

```
&time_control
run_days                            =   0,
run_hours                           =   10,
run_minutes                         =   0,
run_seconds                         =   0,
start_year                          =   0001,
start_month                         =   01,
start_day                           =   01,
start_hour                          =   00,
start_minute                        =   00,
start_second                        =   00,
end_year                            =   0001,
end_month                           =   01,
end_day                             =   01,
end_hour                            =   10,
end_minute                          =   00,
end_second                          =   00,
history_interval                    =   10,
frames_per_outfile                  =   1000,
restart                             =   .false.,
restart_interval                    =   1200,
```

```
io_form_history          =  2
io_form_restart          =  2
io_form_input            =  2
io_form_boundary         =  2
debug_level              =  0
/

&domains
time_step                =  20,
time_step_fract_num      =  0,
time_step_fract_den      =  1,
max_dom                  =  1,
s_we                     =  1,
e_we                     =  202,
s_sn                     =  1,
e_sn                     =  3,
s_vert                   =  1,
e_vert                   =  41,
dx                       =  2000,
dy                       =  2000,
ztop                     =  30000.,
/

&physics
mp_physics               =  10,
ra_lw_physics            =  0,
ra_sw_physics            =  0,
radt                     =  0,
sf_sfclay_physics        =  0,
sf_surface_physics       =  0,
bl_pbl_physics           =  0,
bldt                     =  0,
cu_physics               =  0,
cudt                     =  0,
num_soil_layers          =  5,
```

```
/

&fdda
/

&dynamics
rk_ord                  =   3,
diff_opt                =   2,
km_opt                  =   1,
damp_opt                =   3,
zdamp                   =   20000.,
dampcoef                =   .1,
khdif                   =   00,
kvdif                   =   0,
smdiv                   =   0.1,
emdiv                   =   0.01,
epssm                   =   0.1,
time_step_sound         =   6,
h_mom_adv_order         =   5,
v_mom_adv_order         =   3,
h_sca_adv_order         =   5,
v_sca_adv_order         =   3,
non_hydrostatic         =   .true.,
/

&bdy_control
periodic_x              =   .false.,
symmetric_xs            =   .false.,
symmetric_xe            =   .false.,
open_xs                 =   .true.,
open_xe                 =   .true.,
periodic_y              =   .true.,
symmetric_ys            =   .false.,
symmetric_ye            =   .false.,
open_ys                 =   .false.,
```

```
open_ye                 =   .false.,
/

&grib2
/

&namelist_quilt
nio_tasks_per_group     =   0,
nio_groups              =   1,
/
```

Bibliography

Abel, S. J., and I. A. Boutle, An improved representation of the raindrop size distribution for single-moment microphysics schemes, *Quarterly Journal of the Royal Meteorological Society*, *138*(669), 2151–2162, 2012.

Albrecht, B. A., Aerosols, cloud microphysics, and fractional cloudiness, *Science*, *245*(4923), 1227–1230, 1989.

Allen, M. R., and W. J. Ingram, Constraints on future changes in climate and the hydrologic cycle., *Nature*, *419*(6903), 224–32, 2002.

Allen, P. A., *Earth surface processes*, Blackwell Science Ltd., 1997.

Anderson, G., S. Clough, F. Kneizys, J. Chetwynd, and E. Shettle, AFGL Atmospheric consituent profiles (0-120 km), *Environmental Research Papers*, *954*, 1986.

Andrews, D. G., *An introduction to atmospheric physics*, Cambridge University Press, 2010.

Armenian Travel Bureau, Climate in Armenia, *http://www.atb.am/en/armenia/nature/climate/*, 2013.

Atlas, D., and C. W. Ulbrich, Path-and area-integrated rainfall measurement by microwave attenuation in the 1-3 cm band, *Journal of Applied Meteorology*, *16*(12), 1322–1331, 1977.

Atlas, D., R. C. Srivastava, and R. S. Sekhon, Doppler radar characteristics of precipitation at vertical incidence, *Reviews of Geophysics*, *11*(1), 1–35, 1973.

Baartman, J. E. M., V. G. Jetten, C. J. Ritsema, and J. Vente, Exploring effects of rainfall intensity and duration on soil erosion at the catchment scale using openLISEM: Prado catchment, SE Spain, *Hydrological Processes*, *26*(7), 1034–1049, 2012.

Bagarello, V., V. Ferro, and G. Giordano, Testing alternative erosivity indices to predict event soil loss from bare plots in Southern Italy, *Hydrological Processes*, *24*(6), 789–797, 2010.

Barros, A. P., O. P. Prat, and F. Y. Testik, Size distribution of raindrops, *Nature Physics*, *6*(4), 232–232, 2010.

Beard, K., and H. R. Pruppacher, A determination of the terminal velocity and drag of small water drops by means of a wind tunnel, *Journal of the Atmospheric Sciences*, *26*, 1066–1072, 1969.

Beard, K. V., Terminal velocity and shape of cloud and precipitation drops aloft, *Journal of the Atmospheric Sciences*, *33*(5), 851–864, 1976.

Berg, P., J. O. Haerter, P. Thejll, C. Piani, S. Hagemann, and J. H. Christensen, Seasonal characteristics of the relationship between daily precipitation intensity and surface temperature, *Journal of Geophysical Research*, *114*, 2009.

Best, A. C., The size distribution of raindrops, *Quarterly Journal of the Royal Meteorological Society*, *76*(327), 16–36, 1950.

Boardman, J., Soil erosion science: reflections on the limitations of current approaches, *Catena*, *68*(2-3), 73–86, 2006.

Boas, M. L., *Mathematical methods in the physical sciences*, second ed., John Wiley and Sons, Inc., 1983.

Boer, G. J., Climate change and the regulation of the surface moisture and energy budgets, *Climate Dynamics*, *8*(5), 225–239, 1993.

Bozkurt, D., and O. L. Sen, Climate change impacts in the Euphrates—Tigris Basin based on different model and scenario simulations, *Journal of Hydrology*, *480*, 149–161, 2013.

Bozkurt, D., U. Turuncoglu, O. L. Sen, B. Onol, and H. N. Dalfes, Downscaled simulations of the ECHAM5, CCSM3 and HadCM3 global models for the eastern Mediterranean—Black Sea region: evaluation of the reference period, *Climate Dynamics*, *39*(1-2), 207–225, 2011.

BP, Baku-Tbilisi-Ceyhan Pipeline, *http://www.bp.com/sectiongenericarticle.do?categoryId=9006669&contentId=7015093*, 2013.

Brown, L. C., and G. R. Foster, Storm erosivity using idealized intensity distributions, *Transactions of the ASABE*, *30*(2), 0379 –0386, 1987.

Chen, F., and J. Dudhia, Coupling an advanced land surface-hydrology model with the Penn State-NCAR MM5 modeling system. Part I: model implementation and sensitivity, *Monthly Weather Review*, *129*(4), 569–585, 2001.

Cohard, J.-M., and J.-P. Pinty, A comprehensive two-moment warm microphysical bulk scheme. I: Description and tests, *Quarterly Journal of the Royal Meteorological Society*, *126*(566), 1815–1842, 2000.

Crosson, P., Soil erosion estimates and costs, *Science*, *269*, 461–462, 1995.

Cullen, H. M., and P. B. Demenocal, North Atlantic influence on Tigris–Euphrates streamflow, *International Journal of Climatology*, *20*(8), 853–863, 2000.

Cushman-Roisin, B., Introduction to geophysical fluid dynamics, 1994.

Demirci, A., and A. Karaburun, Estimation of soil erosion using RUSLE in a GIS framework: a case study in the Buyukcekmece Lake watershed, northwest Turkey, *Environmental Earth Sciences*, *66*(3), 903–913, 2011.

Dudhia, J., Numerical study of convection observed during the winter monsoon experiment using a mesoscale two-dimensional model, *Journal of the Atmospheric Sciences*, *46*(20), 3077–3107, 1989.

European Commission, Turkey - agriculture and enlargement, *Tech. rep.*, European Commission, 2013.

Evans, J. P., 21st century climate change in the Middle East, *Climatic Change*, *92*(3-4), 417–432, 2008.

Evans, J. P., R. B. Smith, and R. J. Oglesby, Middle East climate simulation and dominant precipitation processes, *International Journal of Climatology*, *24*(13), 1671–1694, 2004.

Fan, J., T. Yuan, J. M. Comstock, S. Ghan, A. Khain, L. R. Leung, Z. Li, V. J. Martins, and M. Ovchinnikov, Dominant role by vertical wind shear in regulating aerosol effects on deep convective clouds, *Journal of Geophysical Research*, *114*, 2009.

Fan, J., L. R. Leung, Z. Li, H. Morrison, H. Chen, Y. Zhou, Y. Qian, and Y. Wang, Aerosol impacts on clouds and precipitation in eastern China: results from bin and bulk microphysics, *Journal of Geophysical Research*, *117*, 1–21, 2012.

Favis-Mortlock, D. T., and A. J. Guerra, The implications of general circulation model estimates of rainfall for future erosion: a case study from Brazil, *Catena*, *37*(3-4), 329–354, 1999.

Feingold, G., and Z. Levin, The lognormal fit to raindrop spectra from frontal

convective clouds in Israel, *Journal of Climate and Applied Meteorology*, *25*(10), 1346–1363, 1986.

Ferrier, B. S., A double-moment multiple-phase four-class bulk ice scheme. Part I: Description, *Journal of the Atmospheric Sciences*, *51*(2), 249–280, 1994.

Flanagan, D. C., J. C. Ascough II, M. A. Nearing, and J. M. Laflen, The water erosion prediction project (WEPP) model, in *Landscape Erosion and Evolution Modeling*, pp. 145–199, Springer, 2001.

Fox, N. I., Technical note: The representation of rainfall drop-size distribution and kinetic energy, *Hydrology and Earth System Sciences*, *8*(5), 1001–1007, 2004.

Georgian Academy of Sciences, Climate study for the Georgian part of the AGT pipeline corridor, *Tech. rep.*, Institute of Hydrometeorology, 2002.

Giorgi, F., and P. Lionello, Climate change projections for the Mediterranean region, *Global and Planetary Change*, *63*(2-3), 90–104, 2008.

Google, Google Earth version 7, 2013.

Gunn, K. L. S., and J. S. Marshall, The distribution with size of aggregate snowflakes, *Journal of Meteorology*, *15*(5), 452–461, 1958.

Gunn, R., and G. D. Kinzer, The terminal velocity of fall for water droplets in stagnant air, *Journal of Meteorology*, *6*(4), 243–248, 1949.

Haerter, J. O., P. Berg, and S. Hagemann, Heavy rain intensity distributions on varying time scales and at different temperatures, *Journal of Geophysical Research*, *115*, 2010.

Hansen, J. W., and A. V. M. Ines, Stochastic disaggregation of monthly rainfall data for crop simulation studies, *Agricultural and Forest Meteorology*, *131*, 233–246, 2005.

Hartmann, D. L., *Global physical climatology*, vol. 56, Academic press, 1994.

Haylock, M. R., N. Hofstra, A. M. G. Klein Tank, E. J. Klok, P. D. Jones, and M. New, A European daily high-resolution gridded data set of surface temperature and precipitation for 1950–2006, *Journal of Geophysical Research: Atmospheres (1984–2012)*, *113*, 2008.

Held, I. M., and B. J. Soden, Robust responses of the hydrological cycle to global warming, *Journal of Climate*, *19*(21), 5686–5699, 2006.

Heydar Aliyev Foundation, Major aspects of climate, *http://www.azerbaijan.az/_Geography/_Climate/_climate_e.html*, 2013.

Huntingford, C., R. G. Jones, C. Prudhomme, R. Lamb, J. H. C. Gash, and D. A. Jones, Regional climate-model predictions of extreme rainfall for a changing climate, *Quarterly Journal of the Royal Meteorological Society*, *129*(590), 1607–1621, 2003.

Igel, A. L., S. C. van den Heever, C. M. Naud, S. M. Saleeby, and D. J. Posselt, Sensitivity of Warm-Frontal Processes to Cloud-Nucleating Aerosol Concentrations, *Journal of the Atmospheric Sciences*, *70*(6), 1768–1783, 2013.

Illingworth, A. J., and C. J. Stevens, An optical disdrometer for the measurement of raindrop size spectra in windy conditions, *Journal of Atmospheric and Oceanic Technology*, *4*(3), 411–421, 1987.

IPCC, *Climate Change 2007: The Physical Science Basis. Contribution of Working Group I to the Fourth Assessment Report of the Intergovernmental Panel on Climate Change*, Cambridge University Press, Cambridge, United Kingdom and New York, NY, USA., 2007.

IPCC, Summary for policymakers, in *Climate Change 2013: The Physical Science Basis. Contribution of Working Group I to the Fifth Assessment Report of the Intergovernmental Panel on Climate Change*, edited by T. F. Stocker, D. Qin, G.-K. Plattner, M. Tignor, S. K. Allen, J. Boschung, A. Nauels, Y. Xia, V. Bex, and P. M. Midgley, Cambridge University Press, Cambridge, United Kingdom and New York, NY, USA., 2013.

Janjic, Z. I., The step-mountain eta coordinate model: Further developments of the convection, viscous sublayer, and turbulence closure schemes, *Monthly Weather Review*, *122*(5), 927–945, 1994.

Jiang, H., H. Xue, A. Teller, G. Feingold, and Z. Levin, Aerosol effects on the lifetime of shallow cumulus, *Geophysical Research Letters*, *33*(14), L14,806, 2006.

Joss, J., and A. Waldvogel, Ein spektrograph fur niederschlagstropfen mit automatischer auswertung, *Pure and Applied Geophysics*, *68*(1), 240–246, 1967.

Joss, J., and A. Waldvogel, Comments on 'Some Observations on the Joss-Waldvogel Rainfall Disdrometer', *Journal of Applied Meteorology*, *16*, 112, 1977.

Kain, J. S., The Kain-Fritsch convective parameterization: an update, *Journal of Applied Meteorology*, *43*(1), 170–181, 2004.

Kendon, E. J., N. M. Roberts, C. A. Senior, and M. J. Roberts, Realism of rainfall in a very high-resolution regional climate model, *Journal of Climate*, *25*(17), 5791–5806, 2012.

Kereselidze, D. N., L. G. Matchavariani, B. B. Kalandadze, and V. Z. Trapaidze, Allowable soil erosion rates in Georgia, *Eurasian Soil Science*, *46*(4), 438–446, 2013.

Kessler, E., On the distribution and continuity of water substance in atmospheric circulations, *Meteorological Monographs*, *32*(10), 1969.

Khain, A., and B. Lynn, Simulation of a supercell storm in clean and dirty atmosphere using weather research and forecast model with spectral bin microphysics, *Journal of Geophysical Research*, *114*, 2009.

Khain, A., M. Ovtchinnikov, M. Pinsky, A. Pokrovsky, and H. Krugliak, Notes on the state-of-the-art numerical modeling of cloud microphysics, *Atmospheric Research*, *55*(3-4), 159–224, 2000.

Khain, A., D. Rosenfeld, and A. Pokrovsky, Aerosol impact on the dynamics and microphysics of deep convective clouds, *Quarterly Journal of the Royal Meteorological Society*, *131*(611), 2639–2663, 2005.

Khain, A. P., Notes on state-of-the-art investigations of aerosol effects on precipitation: a critical review, *Environmental Research Letters*, *4*, 2009.

Khain, A. P., N. BenMoshe, and A. Pokrovsky, Factors determining the impact of aerosols on surface precipitation from clouds: an attempt at classification, *Journal of the Atmospheric Sciences*, *65*(6), 1721–1748, 2008.

Kinnell, P., Event soil loss, runoff and the Universal Soil Loss Equation family of models: A review, *Journal of Hydrology*, *385*, 384–397, 2010.

Kinnell, P., K. McGregor, and C. Rosewell, The IXEA index as an alternative to the EI30 erosivity index, *Transactions of the American Society of Agricultural Engineers*, *37*(5), 1449–1456, 1994.

Kinnell, P. I. A., Some observations on the Joss-Waldvogel rainfall disdrometer., *Journal of Applied Meteorology*, *15*, 499–502, 1976.

Kinnell, P. I. A., Rainfall intensity-kinetic energy relationships for soil loss prediction, *Soil Science Society of America Journal*, *45*(1), 153–155, 1981.

Kirkbride, M. P., and A. D. Reeves, Soil erosion caused by low-intensity rainfall in Angus, Scotland, *Applied Geography*, *13*(4), 299–311, 1993.

Kostinski, A. B., and R. a. Shaw, Droplet dynamics: Raindrops large and small, *Nature Physics*, *5*(9), 624–625, 2009.

Laprise, R., The Euler Equations of motion with hydrostatic pressure as as independent variable, *Monthly Weather Review*, *120*, 197–207, 1992.

Laws, J. O., Measurements of the fall-velocity of water-drops and raindrops, *Transactions, American Geophysical Union*, *22*, 709–721, 1941.

Laws, J. O., and D. A. Parsons, The relation of raindrop-size to intensity, *Transactions, American Geophysical Union*, *24*, 452–460, 1943.

Lebsock, M. D., G. L. Stephens, and C. Kummerow, Multisensor satellite observations of aerosol effects on warm clouds, *Journal of Geophysical Research*, *113*, 2008.

Lee, S.-S., and G. Feingold, Aerosol effects on the cloud-field properties of tropical convective clouds, *Atmospheric Chemistry and Physics*, *13*(14), 6713–6726, 2013.

Lee, S. S., L. J. Donner, V. T. J. Phillips, and Y. Ming, The dependence of aerosol effects on clouds and precipitation on cloud-system organization, shear and stability, *Journal of Geophysical Research*, *113*, 2008.

Lelieveld, J., et al., Climate change and impacts in the Eastern Mediterranean and the Middle East, *Climatic Change*, *114*(3-4), 667–687, 2012.

Lenderink, G., and E. van Meijgaard, Increase in hourly precipitation extremes beyond expectations from temperature changes, *Nature Geoscience*, *1*(8), 511–514, 2008.

Lenderink, G., and E. van Meijgaard, Unexpected rise in extreme precipitation caused by a shift in rain type?, *Nature Geoscience*, *2*(6), 373–373, 2009.

Lenderink, G., and E. van Meijgaard, Linking increases in hourly precipitation extremes to atmospheric temperature and moisture changes, *Environmental Research Letters*, *5*(2), 025,208, 2010.

Leung, L. R., Y.-H. Kuo, and J. Tribbia, Research needs and directions of regional climate modeling using WRF and CCSM, *Bulletin of the American Meteorological Society*, *87*(12), 1747–1751, 2006.

Li, Z., F. Niu, J. Fan, Y. Liu, D. Rosenfeld, and Y. Ding, Long-term impacts of aerosols on the vertical development of clouds and precipitation, *Nature Geoscience*, *4*(12), 888–894, 2011.

Liepert, B. G., and M. Previdi, Do models and observations disagree on the rainfall response to global warming?, *Journal of Climate*, *22*(11), 3156–3166, 2009.

Lim, K.-S. S., and S.-Y. Hong, Development of an effective double-moment cloud microphysics scheme with prognostic cloud condensation nuclei (CCN) for weather and climate models, *Monthly Weather Review*, *138*(5), 1587–1612, 2010.

Liu, J. Y., and H. D. Orville, Numerical modeling of precipitation and cloud shadow effects on mountain-induced cumuli, *Journal of the Atmospheric Sciences*, *26*(6), 1283–1298, 1969.

Mahmudov, R., Water Resources of the Azerbaijan Republic, *Tech. rep.*, Scientific Research Institute of Hydrometeorology, Ministry of Ecology and Natural Resources of the Azerbaijan Republic, 2003.

Marques, M. J., R. Bienes, R. Pérez-Rodríguez, and L. Jiménez, Soil degradation in central Spain due to sheet water erosion by low-intensity rainfall events, *Earth Surface Processes and Landforms*, *33*(3), 414–423, 2008.

Marshall, J. S., and W. M. K. Palmer, The distribution of raindrops with size, *Journal of Meteorology*, *5*(4), 165–166, 1948.

Martinez-Casasnovas, J., M. Ramos, and M. Ribes-Dasi, Soil erosion caused by extreme rainfall events: mapping and quantification in agricultural plots from very detailed digital elevation models, *Geoderma*, *105*(1-2), 125–140, 2002.

Milbrandt, J. A., and R. McTaggart-Cowan, Sedimentation-induced errors in bulk microphysics schemes, *Journal of the Atmospheric Sciences*, *67*(12), 3931–3948, 2010.

Milbrandt, J. A., and M. K. Yau, A multimoment bulk microphysics parameterization. Part I: Analysis of the role of the spectral shape parameter, *Journal of the Atmospheric Sciences*, *62*(9), 3051–3064, 2005.

Ministry Of the Islamic Republic of Iran, Iran's climate, *http://www.en.iran.ir/about/climate*, 2013.

Mlawer, E. J., S. J. Taubman, P. D. Brown, M. J. Iacono, and S. A. Clough, Radiative transfer for inhomogeneous atmospheres: RRTM, a validated correlated-k model for the longwave, *Journal of Geophysical Research*, *102*, 1997.

Montero-Martinez, G., A. B. Kostinski, R. a. Shaw, and F. García-García, Do all raindrops fall at terminal speed?, *Geophysical Research Letters*, *36*(11), 2009.

Morgan, R., *Soil Erosion and Conservation*, second ed., Longman Group UK Limited, 1986.

Morrison, H., and J. Milbrandt, Comparison of two-moment bulk microphysics schemes in idealized supercell thunderstorm simulations, *Monthly Weather Review*, 2010.

Morrison, H., J. A. Curry, and V. I. Khvorostyanov, A new double-moment microphysics parameterization for application in cloud and climate models. Part I: description, *Journal of the Atmospheric Sciences*, *62*, 1665–1677, 2005.

Morrison, H., G. Thompson, and V. Tatarskii, Impact of cloud microphysics on the development of trailing stratiform precipitation in a simulated squall line: comparison of one- and two-moment schemes, *Monthly Weather Review*, *137*(3), 991–1007, 2009.

Nearing, M., et al., Modeling response of soil erosion and runoff to changes in precipitation and cover, *Catena*, *61*(2-3), 131–154, 2005.

Nearing, M. A., Potential changes in rainfall erosivity in the US with climate change during the 21st century, *Journal of Soil and Water Conservation*, *56*(3), 229–232, 2001.

Nicks, A. D., and G. A. Gander, CLIGEN: a weather generator for climate inputs to water resource and other models, in *Proc. Fifth Int. Conf. on Computers in Agriculture*, pp. 903–909, 1994.

Niu, F., and Z. Li, Systematic variations of cloud top temperature and precipitation rate with aerosols over the global tropics, *Atmospheric Chemistry and Physics*, *12*(18), 8491–8498, 2012.

Niu, S., X. Jia, J. Sang, X. Liu, C. Lu, and Y. Liu, Distributions of raindrop sizes and fall velocities in a semiarid plateau climate: convective versus stratiform rains, *Journal of Applied Meteorology and Climatology*, *49*(4), 632–645, 2010.

Nohara, D., A. Kitoh, M. Hosaka, and T. Oki, Impact of climate change on river discharge projected by multimodel ensemble, *Journal of Hydrometeorology*, *7*, 1076–1089, 2006.

Pall, P., M. R. Allen, and D. A. Stone, Testing the Clausius–Clapeyron constraint on changes in extreme precipitation under CO2 warming, *Climate Dynamics*, *28*(4), 351–363, 2007.

Parsons, A. J., and A. M. Gadian, Uncertainty in modelling the detachment of soil by rainfall, *Earth Surface Processes and Landforms*, *25*(7), 723–728, 2000.

Pedersen, H. S. r., and B. Hasholt, Influence of wind speed on rainsplash erosion, *Catena*, *24*(1), 39–54, 1995.

Pimentel, D., et al., Environmental and economic costs of soil erosion and conservation benefits, *Science*, *267*, 1117–1123, 1995.

Pruppacher, H. R., and J. D. Klett, *Microphysics of Clouds and Precipitation*, vol. 18, 954 pp., 1997.

Pruski, F. F., and M. Nearing, Climate-induced changes in erosion during the 21st century for eight U.S. locations, *Water Resources Research*, *38*(12), 34–1–34–11, 2002a.

Pruski, F. F., and M. Nearing, Runoff and soil-loss responses to changes in precipitation: A computer simulation study, *Journal of Soil and Water Conservation*, *57*(1), 7–16, 2002b.

Reisner, J., R. M. Rasmussen, and R. T. Bruintjes, Explicit forecasting of supercooled liquid water in winter storms using the MM5 mesoscale model, *Quarterly Journal of the Royal Meteorological Society*, *124*, 1071–1107, 1998.

Renard, K., and J. Freimund, Using monthly precipitation data to estimate the R-factor in the revised USLE, *Journal of Hydrology*, *157*, 287–306, 1994.

Renard, K., G. Foster, G. Weesies, D. McCool, and D. Yoder, Predicting soil erosion by water: a guide to conservation planning with the Revised Universal Soil Loss Equation (RUSLE), *Tech. rep.*, U.S. Department of Agriculture, 1997.

Rogers, R. R., Raindrop collision rates, *Journal of the Atmospheric Sciences*, *46*, 2469–2472, 1989.

Rogers, R. R., and M. K. Yau, *A short course in cloud physics*, third ed., Pergamon Press plc, Oxford, UK, 1989.

Rosenfeld, D., Aerosol-cloud interactions control of earth radiation and latent heat release budgets, *Space Science Reviews*, *125*(1-4), 149–157, 2006.

Rosenfeld, D., and C. W. Ulbrich, Cloud microphysical properties, processes, and rainfall estimation opportunities, *Radar and Atmospheric Science: A Collection of Essays in Honor of David Atlas, Meteor. Monogr*, (52), 237–258, 2003.

Rosenfeld, D., and W. Woodley, Deep convective clouds with sustained supercooled liquid water down to -37.5 degrees C, *Nature*, *405*(6785), 440–2, 2000.

Rosenfeld, D., U. Lohmann, G. B. Raga, C. D. O'Dowd, M. Kulmala, S. Fuzzi, A. Reissell, and M. O. Andreae, Flood or drought: how do aerosols affect precipitation?, *Science (New York, N.Y.)*, *321*(5894), 1309–13, 2008.

Rosewell, C. J., Rainfall kinetic energy in eastern Australia, *Journal of Climate and Applied Meteorology*, *25*(11), 1695–1701, 1986.

Saha, S., and Coauthors, The NCEP Climate Forecast System, *Journal of Climate*, *19*(15), 3483–3517, 2006.

Salathe Jr, E. P., L. R. Leung, Y. Qian, and Y. Zhang, Regional climate model projections for the State of Washington, *Climatic Change*, *102*(1-2), 51–75, 2010.

Salles, C., J. Poesen, and D. Sempere-Torres, Kinetic energy of rain and its functional relationship with intensity, *Journal of Hydrology*, *257*(1), 256–270, 2002.

Schneider, U., A. Becker, P. Finger, B. Meyer-Christoffer, Anja Rudolf, and M. Ziese, GPCC Full Data Reanalysis Version 6.0 at 0.5: Monthly land-surface precipitation from rain-gauges built on GTS-based and historic data., 2011.

Seifert, A., and K. D. Beheng, A double-moment parameterization for simulating autoconversion, accretion and selfcollection, *Atmospheric Research*, *59-60*, 265–281, 2001.

Sekhon, R. S., and R. C. Srivastava, Snow size spectra and radar reflectivity, *Journal of the Atmospheric Sciences*, *27*(2), 299–307, 1970.

Sensoy, S., Climate of Turkey, *Tech. rep.*, Turkish State Meteorological Service, 2013.

Shahgedanova, M., W. Hagg, D. Hassell, C. Stokes, and V. Popvnin, Climate change, glacier retreat, and water availability in the Caucasus region, *Threats to Global Water Security*, pp. 131–143, 2009.

Shelton, N., Azerbaijan : environmental conditions and outlook, *AMBIO: A Journal of the Human Environment*, *32*(4), 302–306, 2003.

Shipway, B. J., and a. a. Hill, Diagnosis of systematic differences between multiple parametrizations of warm rain microphysics using a kinematic framework, *Quarterly Journal of the Royal Meteorological Society*, *138*(669), 2196–2211, doi: 10.1002/qj.1913, 2012.

Skamarock, W. C., J. B. Klemp, D. O. Gill, D. M. Barker, M. G. Duda, X.-Y. Huang, W. Wang, and J. G. Powers, A Description of the Advanced Research WRF Version 3, *NCAR Technical Note NCAR/TN-475+STR*, (June), 2008.

Smith, P. L., Raindrop size distributions: Exponential or Gamma - does the difference matter?, *Journal of Applied Meteorology*, *42*(7), 1031–1034, 2003.

Solomon, S., et al., Technical Summary, in *Climate Change 2007: The Physical Science Basis. Contribution of Working Group I to the Fourth Assessment Report of the Intergovernmental Panel on Climate Change*, edited by S. Solomon, D. Qin, M. Manning, Z. Chen, M. Marquis, K. Averyt, M. Tignor, and H. Miller, Cambridge University Press, Cambridge, United Kingdom and New York, NY, USA., 2007.

Squires, P., The microstructure and colloidal stability of warm clouds, *Tellus*, *10*(2), 256–261, 1958.

Squires, P., and S. Twomey, The relation between cloud droplet spectra and the spectrum of cloud nuclei, in *Physics of Precipitation: Proceedings of the Cloud Physics Conference, Woods Hole, Massachusetts, June 3-5, 1959*, pp. 211–219, Wiley Online Library, 1960.

Srivastava, R. C., A study of the effect of precipitation on cumulus dynamics, *Journal of the Atmospheric Sciences*, *24*, 36–45, 1967.

Srivastava, R. C., The size distribution of raindrops generated by their breakup and coalescence, *Journal of the Atmospheric Sciences*, *28*(3), 410–415, 1971.

Steiner, M., and J. A. Smith, Reflectivity, rain rate, and kinetic energy flux relationships based on raindrop spectra, *Journal of Applied Meteorology*, *39*(11), 1923–1940, 2000.

Szakáll, M., S. K. Mitra, K. Diehl, and S. Borrmann, Shapes and oscillations of falling raindrops — a review, *Atmospheric Research*, *97*(4), 416–425, 2010.

Tao, W.-K., X. Li, A. Khain, T. Matsui, S. Lang, and J. Simpson, Role of atmospheric aerosol concentration on deep convective precipitation: Cloud-resolving model simulations, *Journal of Geophysical Research*, *112*(D24), D24S18, 2007.

Tao, W.-k., J.-p. Chen, Z. Li, C. Wang, and C. Zhang, Impact of Aerosols on Convective Clouds and Precipitation, *Reviews of Geophysics*, *50*, 1–162, 2012.

Testik, F. Y., and A. P. Barros, Toward elucidating the microstructure of warm rainfall: a survey, *Reviews of Geophysics*, *45*, 1–21, 2007.

Thompson, G., R. M. Rasmussen, and K. Manning, Explicit forecasts of winter precipitation using an improved bulk microphysics scheme. Part I: description and sensitivity analysis, *Monthly Weather Review*, *132*(2), 519–542, 2004.

Thompson, G., P. R. Field, R. M. Rasmussen, and W. D. Hall, Explicit forecasts of winter precipitation using an improved bulk microphysics scheme. Part II: implementation of a new snow parameterization, *Monthly Weather Review*, *136*(12), 5095–5115, 2008.

Torres, D. S., J. M. Porrà, and J.-D. Creutin, A general formulation for raindrop size distribution, *Journal of Applied Meteorology*, *33*(12), 1494–1502, 1994.

Trenberth, K. E., Conceptual framework for changes of extremes of the hydrological cycle with climate change, in *Weather and Climate Extremes*, pp. 327–339, Springer, 1999.

Trenberth, K. E., A. Dai, R. M. Rasmussen, and D. B. Parsons, The changing character of precipitation, *Bulletin of the American Meteorological Society*, *84*(9), 1205–1217, 2003.

Twomey, S., The nuclei of natural cloud formation. Part II: the supersaturation in natural clouds and the variation of cloud droplet concentration, *Geofisica Pura e Applicata*, *43*, 243–249, 1959.

Twomey, S., The influence of pollution on the shortwave albedo of clouds, *Journal of Atmospheric Sciences*, *34*, 1149–1152, 1977.

Twomey, S., and J. Warner, Comparison of measurements of cloud droplets and cloud nuclei, *Journal of the Atmospheric Sciences*, *24*, 702, 1967.

Ulbrich, C. W., and D. Atlas, Microphysics of raindrop size spectra: tropical continental and maritime storms, *Journal of Applied Meteorology and Climatology*, *46*(11), 1777–1791, 2007.

UNEP, Chapter 2: Land, in *Global Environment Outlook-3 - Past, present and future perspectives (GEO-3)*, Earthscan Publications, UK, 2002.

UNEP, Chapter 3: Land, in *Global Environment Outlook-4: Environment for development (GEO-4)*, Malta, 2007.

Uplinger, W. G., A new formula for raindrop terminal velocity, in *Conference on Radar Meteorology, 20 th, Boston, MA*, pp. 389–391, 1981.

USDA, About the Universal Soil Loss Equation, *http://www.ars.usda.gov/Research//docs.htm?docid=10626*, 2013.

Usón, A., and M. C. Ramos, An improved rainfall erosivity index obtained from experimental interrill soil losses in soils with a Mediterranean climate, *Catena*, *43*(4), 293–305, 2001.

Van Dijk, A., L. A. Bruijnzeel, and C. J. Rosewell, Rainfall intensity–kinetic energy relationships: a critical literature appraisal, *Journal of Hydrology*, *261*(1), 1–23, 2002.

Verlinde, J., and W. R. Cotton, Fitting microphysical observations of nonsteady convective clouds to a numerical model: an application of the adjoint technique of data assimilation to a kinematic model, *Mon*, *121*, 2776–2793, 1993.

Villermaux, E., and B. Bossa, Single-drop fragmentation determines size distribution of raindrops, *Nature Physics*, *5*(9), 697–702, 2009.

Villermaux, E., and B. Bossa, Size distribution of raindrops reply, *Nature Physics*, *6*(4), 232, 2010.

Villermaux, E., and F. Eloi, The distribution of raindrops speeds, *Geophysical Research Letters*, *38*(19), n/a–n/a, 2011.

Von Storch, H., Models of Global and Regional Climate, in *Encyclopedia of Hydrological Sciences*, chap. 32, pp. 477–490, John Wiley and Sons, Inc., 2006.

Waldvogel, A., The N0 jump of raindrop spectra, *Journal of the Atmospheric Sciences*, *31*, 1067–1078, 1974.

Wang, W., P. Xie, S.-H. Yoo, Y. Xue, A. Kumar, and X. Wu, An assessment of the surface climate in the NCEP climate forecast system reanalysis, *Climate Dynamics*, *37*(7-8), 1601–1620, 2010.

Weisman, M., and J. Klemp, The dependence of numerically simulated convective storms on vertical wind shear and buoyancy, *Monthly Weather Review*, *110*, 504–520, 1982.

Weisman, M. L., and R. Rotunno, The use of vertical wind shear versus helicity in interpreting supercell dynamics, *Journal of the Atmospheric Sciences*, *57*(9), 1452–1472, 2000.

Wentz, F. J., L. Ricciardulli, K. Hilburn, and C. Mears, How much more rain will global warming bring?, *Science*, *317*(5835), 233–235, 2007.

White, R., and R. Toumi, A tightly bound soil-water scheme within an atmosphere-land-surface model, *Journal of Hydrology*, *452-453*(0), 51–63, 2012.

Willis, P. T., Functional fits to some observed drop size distributions and parameterization of rain, *Journal of the Atmospheric Sciences*, *41*(9), 1648–1661, 1984.

Wischmeier, W. H., A rainfall erosion index for a Universal Soil-Loss Equation, *Soil Science Society of America Journal*, *23*(3), 246–249, 1959.

Wischmeier, W. H., and D. D. Smith, Rainfall energy and its relationship to soil loss, *Transactions, American Geophysical Union*, *39*(2), 285–291, 1958.

Wischmeier, W. H., and D. D. Smith, Predicting rainfall erosion losses: a guide to conservation planning, *Tech. rep.*, U.S. Department of Agriculture, 1978.

Wood, A. W., L. R. Leung, V. Sridhar, and D. P. Lettenmaier, Hydrologic implications of dynamical and statistical approaches to downscaling climate model outputs, *Climatic Change*, *62*(1-3), 189–216, 2004.

Woods, C. P., M. T. Stoelinga, and J. D. Locatelli, Size spectra of snow particles measured in wintertime precipitation in the Pacific Northwest, *Journal of the Atmospheric Sciences*, *65*(1), 189–205, 2008.

Yang, D., S. Kanae, T. Oki, T. Koike, and K. Musiake, Global potential soil erosion with reference to land use and climate changes, *Hydrological Processes*, *17*(14), 2913–2928, 2003.

Young, K. C., *Microphysical processes in clouds*, vol. 427, Oxford University Press New York, 1993.

Yu, B., Using CLIGEN to generate RUSLE climate inputs, *Transactions of the American Society of Agricultural Engineers*, *45*(4), 993–1001, 2002.

Zender, C. S., Regional contrasts in dust emission responses to climate, *Journal of Geophysical Research*, *110*, 1–7, 2005.

Zhang, X.-C., Spatial downscaling of global climate model output for site-specific assessment of crop production and soil erosion, *Agricultural and Forest Meteorology*, *135*(1-4), 215–229, 2005.

Zhang, X.-C., A comparison of explicit and implicit spatial downscaling of GCM output for soil erosion and crop production assessments, *Climatic Change*, *84*(3-4), 337–363, 2007.

Zhang, Y., V. Dulière, P. W. Mote, and E. P. Salathé, Evaluation of WRF and HadRM Mesoscale Climate Simulations over the U.S. Pacific Northwest, *Journal of Climate*, *22*(20), 5511–5526, 2009.

Zhang, Y.-G., M. A. Nearing, X.-C. Zhang, Y. Xie, and H. Wei, Projected rainfall erosivity changes under climate change from multimodel and multiscenario projections in Northeast China, *Journal of Hydrology*, *384*(1), 97–106, 2010.

Nomenclature

CCN	Cloud condensation nuclei
CN	Condensation nuclei
DSD	Raindrop size distribution
EI30	Erosivity defined according to equation 1.27
GCMs	General circulation models
GDP	Gross domestic product
PBL	Planetary boundary layer
PSD	Particle Size Distribution
QE	Erosivity defined according to equation 1.28
RCM	Regional climate model
RK3	Runge-Kutta time integration
RUSLE	Revised Universal Soil Loss Equation
USLE	Universal Soil Loss Equation
WPS	WRF Preprocessing System
WRF	Weather Research and Forecasting model